Hydrodynamic coupling of arrays in fluids

Author
Arun Kumar Manickavasagam

Supervisors
Stefanie Gutschmidt
Mathieu Sellier
Mark Jermy

A thesis presented for the degree of
Doctor of Philosophy

Department of Mechanical Engineering
University of Canterbury
New Zealand
14 August 2020

"Only those who risk going too far can possibly find out how far one can go." - T.S.Eliot.

Abstract

Broadband, multi-functional and parallel-processing devices are often built on coupled oscillators or arrays of resonators. Different length scales and applications determine the dominating coupling mechanism of the device. In this work we investigate the effects of fluid-coupling between members of a one-dimensional array in an unbounded and a bounded fluid domain. Our analysis is based on the Navier-Stokes equation for incompressible flow which is solved using a boundary integral technique resulting in the hydrodynamic coupling matrix through which added mass and hydrodynamic dissipation effects are inferred. We also study the influence of non-neighbouring members in view of trying to distinguish between local and global (array) effects. Results clearly suggest that the fluid-coupling is mutually dependent on both gaps between the beams and their respective heights from the surface. Also, non-neighbouring members play a significant role with an increase in size of the array and at gaps less than half the width of the cantilever.

Dedication

To my Father

Acknowledgements

I wish to express my deepest gratitude to my supervisor A/Prof. Stefanie Gutschmidt, for providing me this opportunity to embark on this research adventure and for believing in my abilities. She has been a great source of support, constantly encouraging me to learn new skills and pursue excellence in all that I do. I am extremely fortunate to have a supervisor like Stefanie, who not only has great technical insight but has also acted as a parental figure in pulling me out of the darkest times when my father passed away suddenly in 2017. I am equally grateful to my co-supervisors Prof. Mathieu Sellier for the discussions related to numerical analysis and fluid aspects of the project and Prof. Mark Jermy for providing us the high-speed camera and helping us with the experimental aspects of the project. I would also like to express my sincere thanks to Prof. Ryan Tung for the discussions we have had which helped me learn and understand the modeling for a single beam vibrating in an infinite fluid domain.

I also express my thanks to my reviewers Dr. Richard Clarke and Dr. Martin Homer for taking their time to read my thesis in detail and the constructive feedback they provided which helped improve the quality of my thesis to a great extent.

People in my office and dynamics research group have always been friendly and made research more enjoyable by providing a stimulating research environment. I would like to express my thanks to Sam Jackson, who worked alongside me on AFM arrays in air and the visiting research assistants (VRA's) Martin Raeder and Niclas Wagner for their help with the experiments. I thank my fellow research students for their good-natured attitude and help. In particular, Anthony for his friendship, Farzin for the technical discussions and Khalid for the conversations over many teas and coffees we have had, Jarrod for his good sense of humor, Angus for proof-reading parts of my thesis and Daniel Morris for his cheerfulness.

Also, my thanks to the new friends I made - James Hewett for the hikes and technical assistance, Michael for his encouraging words and organizing social dinner nights, George for his energy and enthusiasm, Niebert for her sense of humor and cricket conversations, Anurag, Shaurya, Sagor and Hammad for many conversations over cups of tea. My thanks also to Ali, Pouria, Sia and Mohammad for their support. My special thanks to Charlie and Carmello for their constant encouragement and positivity which provided me tremendous support during the last leg of my PhD.

I would like to thank the technicians at University of Canterbury - Julian Murphy and Julian Phillips for providing all required electronic components, David Reid for help with 3D printing, Gary Cotton, David Ruston and Gerry Kirk for assistance

with purchasing parts and mechanical design aspects of the test-rig. Also, thanks to Paul and Adam for being patient throughout and allowing me to use many computers in the Mech suite to run my simulations over the summer break.

I would also like to thank the many friends and connections I made through the local cricket and chess communities and beyond which proved to be a welcome distraction when not doing my PhD and helped me recharge. In particular, I would like to thank Alan Alty for the many e-mail conversations we have had during my dark days and providing the much needed moral support since my father's passing. Also, thanks to Shane Young for taking me and my brother Raam out for dinners and Paul and Jane O'Flaherty for making us feel at home away from home.

I extend my thanks to my longtime flatmate Ravi and other friends for their constant encouragement. Lastly, I would like to thank my mother and brother for staying strong in the face of adversity and their unconditional love without which I wouldn't have found the strength to carry on.

Contents

List of Figures

Chapter 1

Introduction

1.1 Background

Since the invention of the scanning tunneling microscope (STM) and the atomic force microscope (AFM), the field of scanning probe microscopy (SPM) has grown tremendously having its applications in chemistry, biology, nanotechnology, material science and electronics. Static structural details of a single molecule have been observed by techniques such as X-ray crystallography, nuclear magnetic resonance (NMR) spectroscopy, single molecule fluorescence microscopy and X-ray electron free laser but it is not possible to directly visualize the dynamic processes using these techniques [2]. Atomic Force Microscopy (AFM) originally invented to provide molecular and sub-atomic resolution images of solid surfaces has overcome this limitation to provide great insights into functioning of proteins within soft biological samples [3].

AFM has been successfully used to visualize membrane and cytoskeletal structures of live cells at nanometre scale [9]. Changes in cell stiffness by analysing the value of Young's modulus of human keratinocytes has also been studied. It is also being used for nanodissection or nanosurgery and is expected to facilitate the search for biomarkers related to disease diagnosis progress and treatment [61]. AFM is a superb technique to study micro and nano-scale biochemical and mechanical processes of live cells relating to diseases. Live cell imaging in physiologically relevant conditions has been the driving force behind AFM developments. AFM has revealed novel molecular resolution information about membrane structures, cell organelles and the cytoskeleton. It has also led to quantification of unbinding events between a cell probe and a second cell, or a ligand or a molecular probe and a host receptor [18].

A commercial AFM consists of a single microcantilever beam (typically a couple hundred of micrometres in length) with a fine tip at its free end to image the sample surface [19]. The atomic interactions between the atoms at the tip and the surface of the sample which is typically approximated mathematically by Lennard-Jones potential causes the deflection of the micro cantilever beam. The deflection of beam varies according to the height of the sample at every location on the sample and is measured by reflecting a laser beam off the surface of the cantilever which provides the profile of the sample surface.

The preferred mode of operation for imaging soft biological samples is the non-contact (nc) mode in which the forces are governed by a potential interaction only and the tip does not come in contact with the sample and hence does not damage fragile samples, e.g. mammalian cells [2]. However, nc mode has lower lateral resolution, limited by tip-sample interaction while the contact mode has high scan speeds and the tapping mode provides a higher lateral resolution (1 nm to 5 nm).

Current stimulated emission depletion (STED) microscopy (live-cell microscopy) uses two synchronized train of laser pulses with one part used for excitation while its counterpart for stimulated emission depletion [33]. It operates in resolution ranges of 180 ± 10 nm to 36 ± 10 nm, being able to visualize processes such as cytokinesis at the rate of $80-100$ frames per second [37]. However, AFM can image at much higher spatial resolutions (< 1 nm) and is less destructive, has high signal to noise ratio, high sensitivity and high throughput operation in fluids which helps in analysing disease states of single cells, thus making it a unique tool. But the rate at which it can image is $1-10$ frames per second. nc-AFM permits experiments in liquid phase without the need for coating, staining or freezing samples [38]. AFM is not just purely an imaging technology, but can also be used to probe mechanical properties. It is easy to use and can be coupled with other types of microscopies and spectroscopies to acquire simultaneous data sets [42]. It has a wide magnification range available, thus advancing the frontiers of cell biology, as no other available method can offer three-dimensional dynamic imaging for living cells and force spectroscopy at micro and molecular resolution [18].

Inspite of the advantages that current AFM technology offers for imaging samples, it currently lacks more precise visualizing of the dynamic molecular processes occurring in tiny cells of soft biological samples in real time at nano-scale. In order to understand their complex dynamic processes it is very important to be able to track the motion of live cells in liquid environments. Current commercial AFM technology is centred around the use of a single cantilever beam to scan the sample. However, this can take a long time and in the process important information about the molecular dynamics occurring at a particular point on the sample may be missed, especially for samples having larger surface area. The current high-speed AFM technology can image dynamic biological processes with nanometer precision at sub-100 ms timescales [29, 45]. Biological events can be very fast and hence it is necessary to achieve faster scan rates without compromising the image quality. Linear scan rates would take hours to cover distances (in cm) [36] and hence, a 100-fold increase in speed will be necessary in order to video image the mammalian cell with the kind of spatial resolution and force control that has been attained for single molecules. Also considering the fact that they are soft samples, sufficient care must be taken to ensure no damage or excessive deformation induced by the technology occurs to samples during the imaging process. One possible solution to overcome this problem is to use an array of cantilevers improving the scan rates resulting in a complete picture of the molecular dynamics over a sample surface [48]. AFM array technology is a prospective solution to visualize dynamic phenomena of live cells in real time at high scan rates of $10-200$ frames per second with high resolutions of < 1 nm in air. Unlike conventional AFM (direct sensing mechanism), these arrays measure tip-deflections using piezoresistive sensors mounted at the clamped end of

each cantilever (indirect method). They are fabricated from multi-layered silicon beams with each probe individually actuated by a bimetallic heater [49].

1.2 Literature Review

As discussed above high-speed AFM is now actively being used to obtain information on biological systems with the technology being commercially available (Bruker, RIBM, AXS and Asylum Research) with imaging speeds up to approximately one frame/s and scan sizes of several tens of microns [29]. For samples having larger surface area, AFM array technology offers a prospective solution to image with increasing scan speeds [49]. However, such technology has not been implemented in fluids yet in which biological samples are preserved. Hence, in the following sections we review the literature on the dynamics of a single and multiple cantilevers operating in a fluid environment which will help us understand the underlying physics (hydrodynamic coupling effects) governing the motion of multiple cantilevers in fluids.

1.2.1 Single cantilever in fluid

Knowledge on hydrodynamic loading of a single cantilever vibrating in fluids is well established in literature. Extensive research has been done on cantilever dynamics in an infinite fluid domain (no wall) [12, 53, 57, 59] and a bounded fluid (vibrating in close proximity to a wall) medium [6, 14–17, 21, 32, 43]. From these studies we know that the natural frequency of a cantilever vibrating in fluid is less by 20% compared to its natural frequency in air or vacuum. This reduction in natural frequency is due to the additional mass of the fluid being moved along with the beam which is known as *added mass or virtual mass effect* and the increase in *viscous damping* caused by the fluid. Researchers have investigated the cantilever dynamics over a range of length scales (from 10^{-9} m to 10^{0} m) for a wide variety of applications such as biosensors [22], atomic force microscopic cantilevers [7], piezoelectric fans [30] and flapping wings for propulsion [55]. Added mass or viscous damping effects stemming from fluid will dominate the dynamic behaviour of the cantilever depending on the type of target application and length scale.

In 1851, Stokes studied hydrodynamic loads acting on vibrating bodies and showed that it is dependent on non-dimensional frequency which is helpful in predicting added mass and viscous damping effects [56]. In 1969, Tuck provided a generalised analytical formula to predict hydrodynamic loads acting on a thin ribbon of arbitrary cross-section exhibiting small oscillatory motions in an incompressible, viscous fluid [57]. Tuck was particularly motivated to study the effect of *'bilge keel'* (each of a pair of plates fastened under the sides of the hull of a ship to provide lateral resistance to water, thus preventing rolling) on small rolling motion of ships. Thus, he presented numerical solutions for a special case considering a ribbon of negligible thickness. In 1998, Sader built upon Tuck's work and presented analytical formulas to study the frequency response of beams with rectangular cross-sections (incorporating transverse oscillations only) in an unbounded fluid domain [53]. It was shown that viscous effects become more significant when the dimensions of the beam are

reduced, whereas they can be ignored for macro-cantilevers ($\sim 10^0$ m). Later in 2000, the results were experimentally validated by Chon et al. [12]. In 2006, Sader et al. [59] presented full "hydrodynamic functions" for a three-dimensional flexible thin blade by deriving exact analytical solutions in contrast to previous works on two-dimensional rigid body models using the boundary integral method [21, 53]. As expected manifestations of the Stokes paradox in the two-dimensional rigid body problem disappeared in genuinely three-dimensional flows.

Other studies analyse the dynamic response of a cantilever close to a solid wall (bounded fluid medium) and conclude that viscous damping has a dominant effect on cantilever dynamics as it approaches the surface whereas changes in added mass have a weak influence [6, 21, 32, 43]. It was also found that the resonance peaks tend to lose their sharpness and flatten out when in close proximity to the surface. Sader et al. [21] found that pressure and vorticity jumps are coupled across the beam when in close proximity to the surface which is not the case in an infinite fluid medium. Also, when the distance between the surface and the beam is more than its width, surface effects become insignificant and the beam's dynamics would be similar to that of a beam in an infinite fluid medium. Kiracofe et al. [32] investigated the nonlinear dynamics of magnetically excited AFM cantilever on graphite and mica, immersed in various fluids. It was shown that the resonance peak can split into two distinct peaks due to nonlinear tip sample interactions and the nonlinear response is determined if one of these forces (tip-sample interaction or hydrodynamic force) is dominant over the other, or if both are dominant.

1.2.2 Multiple cantilever beams in fluids

Over the last decade, there has been a growing interest to study the collective dynamics of multiple cantilever beams immersed in fluids at both macro and micro-level to understand the hydrodynamic coupling effects manifesting in the form of added mass and viscous damping coefficients to predict the overall array dynamics. We classify the arrays into two categories based on length scales, a) macro arrays: $> 10^{-3}$ m and b) micro arrays: $< 10^{-6}$ m

Macro Arrays

Jeong et al. [27] presented an analytical method to study the hydroelastic vibration of two identical rectangular plates coupled via a bounded fluid as shown in Figure 1.1. They predicted the in-phase and out-of-phase modes and validated the results with a three-dimensional finite element analysis.

In 2009, Kimber et al. [31] experimentally quantified the hydrodynamic forces on two centimetre long cantilevers. For the out-of-phase vibration manner shown in Figure 1.2, a decrease in fluid damping is observed for the edge-to-edge configuration while the converse is true for the face-to-face configuration. The reduction in damping in case of the edge-to-edge configuration while the in-phase vibration causes the same behavior in the face-to-face configuration is because the fans travel in the low-pressure wake of their neighbour.

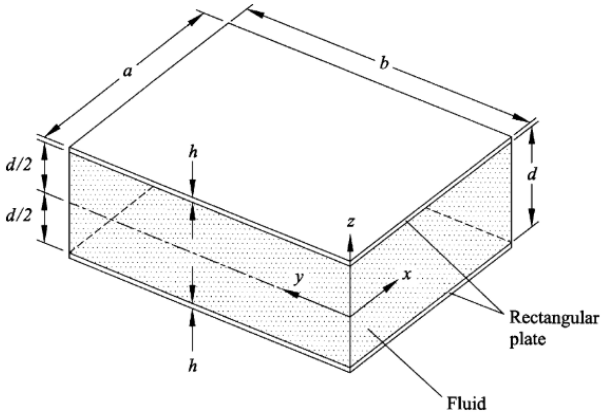

Figure 1.1: Two identical rectangular plates coupled with bounded fluid with a clamped boundary condition along each plate edge. [27]

Figure 1.2: Piezoelectric fans operating in a out-of-phase fashion: (a) edge-to-edge configuration, (b) face-to-face configuration. [31]

Recently Intartaglia et al. [25] combined theoretical, numerical and experimental work to study the flexural vibration of two thin beams coupled in an unbounded, incompressible and viscous fluid. They formulated a hydrodynamic matrix to incorporate the fluid coupling coefficients for two beams placed on top of each other (face-to-face configuration). They validated their proposed approach by performing numerical simulations and experiments on centimetre sized compliant beams. The key findings were that the hydrodynamic loading experienced by each beam was not only due to its absolute motion but it was also affected by its neighbour. The added mass effect was magnified for decreasing gaps and reduced with increasing oscillatory Reynolds number. Choi et al. [11] studied the effect of distance between two cantilevers vibrating in-phase and out-of-phase. They concluded that optimal performance is obtained when cantilevers are operated in an out-of-phase manner and the distance between them is 6 to 8 times the size of a fully grown vortex.

Knowledge of coupled oscillator nonlinear dynamics in the macro-scale domain reaches back as far as Huygens clock [24] and is well established. However, micro-/nano- systems are less probable of operating in the linear regime because of the strong influence of nonlinearities and different physics governs their dynamic behaviour i.e. gravitational forces are negligible. The hydrodynamic coupling effects of arrays of multiple beams operating in liquids in proximity to a surface is currently not understood, which will be the focus of our study here. Studying the coupling dynamics of AFM arrays in proximity to a surface is very critical because it directly relates to the precise interpretation of observed images. For instance, a

shift in frequency may sometimes be misinterpreted as a source of Q-factors or long range interaction forces whereas it may be due to the dominant fluid coupling effects.

Micro Arrays

Hosako et al. [23] analysed the coupled vibration of two micro-cantilevers by modelling the cantilevers as continuous spheres (considering small oscillatory Reynolds number, Re $\ll$ 1) and derived formulas for vibrational coupling amplitude and damping ratio by combining the elastic beam equation and fluid dynamics from Navier-Stokes equation. They validated their theoretical model with actual size (micro) and enlarged (macro) experimental investigations. Coupling amplitude and damping ratio were observed to increase with decreasing beam dimensions and were dependent on the distance between the vibrating beams and resonant frequencies. Clark et al. [13] explored the cantilever dynamics in fluid caused by constant buffeting of fluid particles using a thermodynamic approach. It was shown that the force on the adjacent cantilever due to fluid-induced coupling is more than three times smaller than the Brownian force on the individual cantilever itself. Basak et al. [5] explored the fluid-structure coupling for the same orientation as that of Hosako's model [23] by considering higher oscillatory Reynolds numbers ($Re = 0.01$ to 1000) and provided a deterministic method to obtain the hydrodynamic response of beams. In addition, they assumed that the beams are coupled only through the intervening fluid and ignored structural coupling. They further extended the analysis to an array of five microbeams and suggested that the collective dynamics of the system can be tuned in a manner that will maximize or minimize the hydrodynamic loads on each individual microbeam. Ghatkesar et al. [20] performed experiments on an array of eight microcantilever beams immersed in fluids. They verified the experimental results of eigenfrequency with four available analytical models and found a good match with Sader's extended viscous model [53] which estimates the theoretical eigenfrequency. Lee et al. [35] experimentally investigated the dynamics of a microbeam array consisting of three beams with the middle beam as the operating cantilever and the outer beams as auxiliary cantilevers. Numerical solutions provided insights into the design of experiments. They found that the dynamics of the operating cantilever can be tuned by varying the phase and excitation magnitude of operating cantilevers.

In summary, single cantilever dynamics in fluid is well understood in both unbounded and bounded fluid media in which it has a lesser natural frequency when vibrating in fluid compared to air or vacuum. Also, when the cantilever oscillates in close proximity to a surface an increase in hydrodynamic loading is found and the dissipative component in particular increases dramatically for Reynolds number $Re \leq 1$ and nondimensional height $\frac{h_0}{b} \leq 1$. Hydrodynamic coupling effects of a pair of cantilevers of arbitrary cross-sections in an infinite fluid medium have been studied for different beam configurations: a) edge-to-edge configuration in which the cantilevers are placed side-by-side [5, 31] and b) face-to-face configuration in which they are placed on top of each other [25] . Few others have performed experiments on an array comprising more than two cantilevers [5, 35]. However no existing work on an array of cantilevers vibrating in close proximity to different wall configurations is available. Also, a combined theoretical and experimental approach does not exist

for an array of cantilevers in an edge-to-edge configuration.

1.3 Motivation

Most of the biological processes are faster than the time it takes to capture a full frame with current AFM technology. Hence, it is very demanding to track the real-time motion of tiny cells at faster rates using non-contact AFM technology comprising a single cantilever. Also, spatial resolution for AFM imaging of a whole mammalian cell is only about 50 nm [40]. Therefore, a continuing goal of AFM imaging is to increase the spatial resolution while maintaining the temporal resolution.

Currently atomic and molecular-scale biological processes are not well understood as we lack a technology with which to make these processes visible when operated in their native environments. The targeted non-contact operation mode is largely characterized by nonlinear effects such as geometric, material, tip-sample interactions and coupling effects which can be of mechanical, thermal or fluidic in nature.

Accuracy in measurements and predicted properties are dependent on the underlying physics governing the dynamic behaviour of individual resonators as well as the coupling effects between the cantilevers in an array. One particular technology uses an array of cantilevers but has not been investigated in liquids yet in which biological samples are preserved.

The sample was scanned using a 4-cantilever array and the images were stitched together as seen in Figure 1.3 in which cantilever 3 seemed to have picked the dust particle seen by cantilever 2 but in reality, it is an artifact. The artifact could have arisen from any form of coupling between the cantilevers (mechanical or thermal or fluid (squeeze-film/air)). In our work we are particularly interested in the insights and research outcomes of fluid-coupling effects for the application of an array in fluids to scan living cells which could be of direct use to AFM developers. While the origin of coupling may not be the same in air and liquids, we predict our investigation on fluid-coupling effects will provide a picture of the implications it may have on avoiding artifcats.

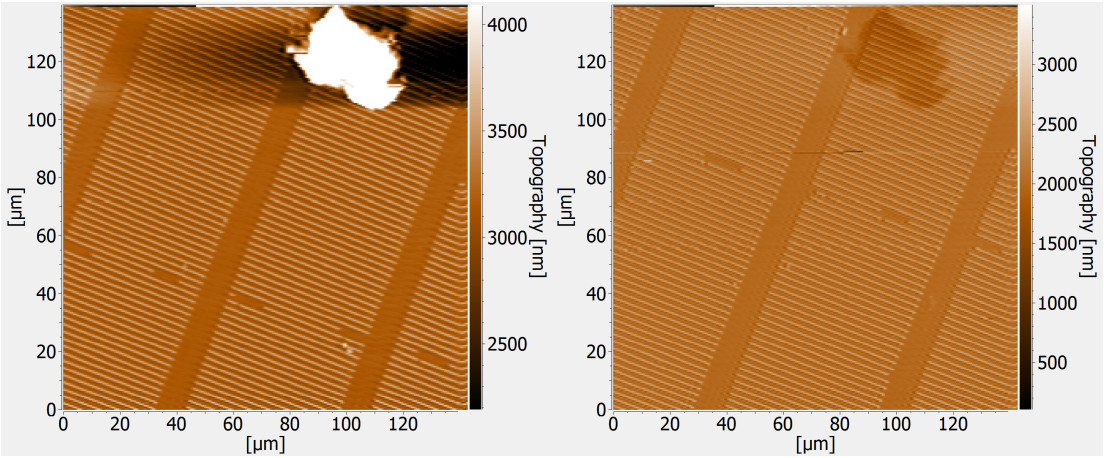

Figure 1.3: Scanned sample using a 4-cantilever array: a) cantilever 2 identifies a dust particle (white area), b) cantilever 3 also identifies the dust particle (shaded area - same location as for cantilever 2) but it is an artefact which is portrayed onto cantilever 3 from cantilever 2, *Courtesy of Rangelow Group at TU Ilmenau, Germany.*

1.4 Objectives

The overall aim of this work is to theoretically and experimentally investigate the coupling dynamics of small-sized arrays of cantilever beams in fluids. We aim to understand the hydrodynamic coupling effects of these array configurations analytically as well as experimentally for a range of Reynolds numbers.

Detailed research objectives include:

1. Parametric analysis and accurate estimation of overall hydrodynamic loading (added mass and damping) and coupling effects when incorporating non-neighbouring members for an array in an infinite fluid domain.
2. Formulating a multi-physics mathematical model incorporating hydrodynamic coupling effects in presence of a nearby wall for an array of beams vibrating in fluids.
3. Experimental design to investigate and make comparisons against numerical results of small-sized arrays in fluids.

1.5 Layout of the Thesis

The thesis is laid out as follows:

Chapter 1 - Introduction describes the motivation for studying the hydrodynamic coupling effects of multiple beams vibrating in close proximity to a surface. It also identifies the existing gaps in literature and the work on which this thesis is built upon.

Chapter 2 - Arrays in an infinite fluid domain reviews the existing array models in an infinite fluid domain and incorporates non-neighbouring members to study its effect on the accuracy of hydrodynamic terms in a three- and a five-beam array.

Chapter 3 - Arrays in close proximity to a surface presents a model for an array of beams vibrating in close proximity to a surface with results presented for an active-passive configuration in two beams, a three- and a five-beam array for different Reynolds numbers.

Chapter 4 - Experimental Design of a test-rig and Comparison of Results contains details of the experimental test-rig design and comparisons against numerical results of coupling effects in small-sized arrays vibrating in fluid.

Chapter 5 - Conclusions and Future Outlook summarizes the research findings and lists limitations of this research work which can be implemented in the future work.

This research work aims to understand the hydrodynamic coupling effects between members of the array both in a bounded (in close proximity to the sample surface) and an unbounded fluid domain with non-neighbouring member effect incorporated, which will be the very first investigation of its kind ever providing an understanding of their effects on the overall array dynamics and thus allowing biologists to vividly understand the physics behind observed images and make reasonable conclusions.

Chapter 2

Arrays in an infinite fluid domain

In this chapter we review existing models for an array of oscillators vibrating in an infinite fluid domain and incorporate the effects of non-neighbouring members in our work to make predictions on hydrodynamic loading and compare it against the predictions of existing models without incorporation of non-neighbouring members in the hydrodynamic coupling matrix. Further, some of the analytical techniques reviewed in this chapter will be the basis for our proposed work in Chapter 3 on an array of oscillators vibrating in close proximity to a rigid surface.

With recent improvements and increased performance specifications of MEMS (micro-electromechanical systems) based technologies such as e.g. scanning probe microscopy [41] or biosensors [22], but also larger scale applications like piezoelectric fans [31] and flapping wings for propulsion [55], there has been a growing interest in understanding the collective dynamics of coupled oscillators, especially when immersed in a fluid. Other examples of coupled nonlinear oscillators include networks of pacemaker cells in the heart [44], congregations of synchronously flashing fireflies [28], crickets chirping in unison [50] and cochlea hair cells [51]. While dominating coupling effects can be of different origin (fluid, mechanical, thermal, etc.) and size, in this work we focus purely on hydrodynamic interactions between members of the array and the ways in which these influence the collective dynamics of the array. More specifically, we investigate the hydrodynamic influences of non-neighbouring members on the local and global array dynamics. The aim of this work is to be able to distinguish between parameter domains at which coupling effects of non-neighbouring members significantly influence or even determine the overall performance of the system and for which these can be neglected.

Basak and Raman [5] studied the hydrodynamic coupling effects between nearest neighbour members of an array of M micro-mechanical beams. The array under investigation was an edge-to-edge configuration and the authors studied the effects of hydrodynamic forces for a range of gap widths, amplitude ratios and relative phases analytically and computationally. They concluded that the dynamics of microbeams in an array can be tuned to either maximize or minimize the hydrodynamic loading on individual microbeams. Intartaglia et al. [25] investigated the hydrodynamic coupling effects of a pair of cantilevers in a face-to-face configuration. Their work sheds light on mutual influences of the two beams, manifested in added mass and dissipation effects. They showed that the added mass effect is magnified for decreas-

ing gaps and hydrodynamic damping decreases as the gap increases. Their proposed theoretical approach was also validated experimentally in water on centimeter sized compliant beams subject to base excitation. Cellini et al. [8] investigated hydrodynamic coupling effects in a parallel array (face-to-face configuration) of five identical ionic polymer metal composites (IPMCs) subjected to low frequency base excitation limiting the interactions only to nearest neighbours. Their analysis suggests that closely spaced IPMCs result in higher harvested powers, which is also validated experimentally. While these works have studied the nearest neighbour interactions, they have ignored the effects of non-neighbouring members.

In this chapter we focus on small sized arrays with three and five beams in an edge-to-edge configuration (considering motion in transverse direction only), see Figure 2.1 for the cross-sectional view of cantilevers in fluid. The beams are long, slender cantilever structures immersed in an incompressible, viscous fluid. While the hydrodynamic coupling effects of a pair and local neighbours of cantilevers in an array have been studied in detail [5], we will focus on the theoretical analysis of hydrodynamic coupling on the effects stemming from non-neighbouring members and/or global array properties.

In what follows, we present the boundary integral theory resulting in matrix-vector equations to compute the added mass and hydrodynamic dissipation effects over the width of the beam.

2.1 General Formulation of the Array Model

2.1.1 Streamfunction formulation

In this section we extend the boundary integral formulation [46] for an array of M beams in general matrix form. The final expression determines the hydrodynamic forces along the width of each beam. We consider small amplitude oscillations of infinitely thin cantilever beams of rectangular cross section, each of width $2b$ and spaced $2g$ apart, see Figure 2.1. The derivations are based on previous work by Tuck [57], Tung [58] and Raman [5]. We, however, highlight new and additional terms of non-neighbouring members and compare, validate and discuss our results against theirs.

We base the derivations of mathematical expressions on the following assumptions:

1. Each microbeam can be of arbitrary cross section as long as the cross section remains uniform along its length.

2. The fluid motion along the axial direction $\mathbf{E_x}$ can be neglected for lower flexural modes.

3. Only transverse vibrations of the beam along $\mathbf{E_z}$ are considered and any lateral motion along $\mathbf{E_y}$ is ignored.

4. Only hydrodynamic coupling effects are considered, ignoring any effects arising from structural coupling.

5. The fluid is incompressible as the acoustic wavelength in both liquids and gases typically exceeds the characteristic length scale of the microbeam.

6. Furthermore, all beams are assumed to oscillate with the same frequency and with small amplitudes and possibly different phases.

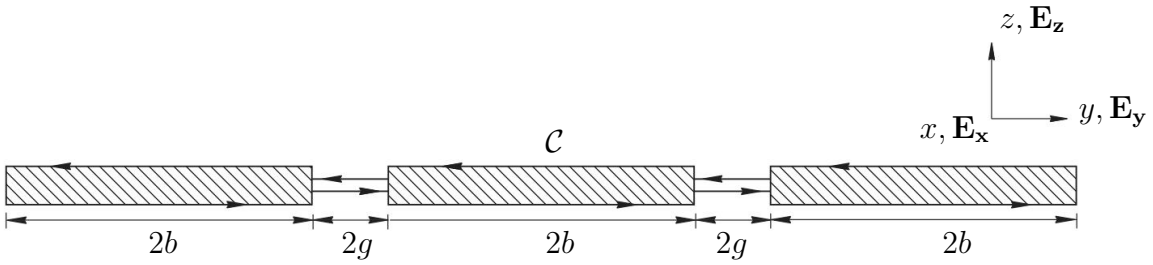

Figure 2.1: Sketch of the boundary value problem for three oscillating rectangular cross-sectional beams. $\mathbf{E_x}$,$\mathbf{E_y}$,$\mathbf{E_z}$ is the vector basis corresponding to the x, y and z coordinate system.

Since nonlinear convective effects are negligible due to the small amplitude assumption, the fluid flow is governed by the linearized Stokes and the continuity equation [21]. The Fourier transformed unsteady Stokes and continuity equations for the fluid is given by [58]

$$i\omega\rho\mathbf{u} = -\nabla P + \mu\nabla^2\mathbf{u},\ \nabla.\mathbf{u} = 0, \tag{2.1}$$

where ω is the driving frequency, $\mathbf{u}(y, z|\omega)$ is the fluid velocity vector given by $\mathbf{u} = v(y, z|\omega)\mathbf{j} + w(y, z|\omega)\mathbf{k}$, where v and w are magnitudes of velocities in the lateral and transverse directions respectively, $p(y, z|\omega)$ is the pressure field in the fluid, and ρ and μ are the density and dynamic viscosity of the fluid respectively. The beam cross sections in the $y - z$ plane are separated from the fluid domain by a closed contour $\mathcal{C}$. The contributions due to the gaps between the beams cancel each other out.

The far-field boundary condition is that $\mathbf{u} \to 0$ as $y, z \to \pm\infty$ and the velocity at the solid-fluid interface is given by:

$$v = 0,\ w = W_m, \tag{2.2}$$

at z = 0 (beam), where v and w are flow velocities along $\mathbf{E_y}$ and $\mathbf{E_z}$, respectively and W_m is the transverse velocity amplitude of the beam cross section.

Following Tuck's work [57], we introduce a stream function $\psi(y, z)$ to satisfy the continuity equation in 2.1

$$v = \psi_z,\ w = -\psi_y. \tag{2.3}$$

Thus, the boundary conditions at the solid-fluid interface in terms of the streamfunction are

$$\psi_z = 0, \quad -\psi_y = W_m. \tag{2.4}$$

Reformulating Equation (2.3) in terms of the streamfunction and application of Green's theorem yields the following expression for the streamfunction; [5]:

$$\begin{aligned}\psi(y,z|\omega) = \int_{\mathcal{C}} (&\psi(y',z'|\omega)G_n(y,z|y',z') \\ &- \psi_n(y',z'|\omega)\Omega(y,z,|y',z') - \zeta(y',z'|\omega)\Psi_n(y,z|y',z') \\ &+ \frac{1}{\mu}P(y',z'|\omega)\Psi_l(y,z|y',z'))\mathrm{d}l,\end{aligned} \tag{2.5}$$

where (y,z) are the coordinates of a point in the fluid domain, (y',z') are the coordinates of a point on the contour $\mathcal{C}$, ζ is the fluid vorticity, and G, Ω and Ψ are the Green's functions for the Laplace operator, the Helmholtz operator and for the operator $\nabla^4(.) - iRe\nabla^2(.)$, respectively. The subscripts n and l define derivatives in normal (transverse) and parallel (lateral) directions to the contour $\mathcal{C}$, respectively.

and the Green's function Ψ is given by

$$\Psi = \frac{1}{\alpha^2}(G - \Omega) \tag{2.6}$$

where $G = \frac{1}{2\pi}\log R$, $\Omega = \frac{-1}{2\pi}K_0(\alpha R)$, $\alpha = \sqrt{iRe}$, K_0 is the modified Bessel function of third kind, order zero and $R = \sqrt{(y-y')^2 + (z-z')^2}$.

Since the lower and upper curves of the beam are infinitesimally close to each other ψ and ψ_n must be continuous (no relative motion between top and bottom surfaces, i.e. $\psi = \psi_n = 0$) across the beam. This results in vanishing of the first two terms in the integral equation (2.5). The problem then involves differentiating the above equation with respect to z and y and evaluating it at $z = 0$ yields the following expressions for the lateral and transverse velocities of the beam:

$$v(y,0|\omega) = 0 = -\int_{-b}^{+b} \Delta\zeta(y',0|\omega)\Psi_{z'z}(y,0|y',0)dy' \tag{2.7a}$$

$$w(y,0|\omega) = W_m = -\int_{-b}^{+b} \frac{1}{\mu}\Delta P(y',0|\omega)\Psi_{y'y}(y,0|y',0)dy' \tag{2.7b}$$

where $\Delta\zeta$ and ΔP are the differences in vorticities and pressures between the top and bottom surfaces of the beam. A numerical scheme is used to convert the

system of integral equations into a corresponding system of matrix equations using quadrature. A nonuniform discretization technique is employed to discretize the beam into N unequal segments, to avoid square root singularities. The existence of logarithmic singularity makes the matrix compliant in its inversion properties and hence we do not eliminate it [57]. Note, however that at the edges when $\xi = \pm 1$ singularities exist which is eliminated by allowing the equations to hold at the mid-point. Once all the matrix entries are computed, the linear system is solved with an ordinary algorithm in Matlab using Gauss-Legendre quadrature to obtain the unknown pressure jumps. A more detailed procedure on computing the pressure differences across the width of the beams can be found in [5].

2.2 Hydrodynamic loading of a single beam

Following the boundary integral method described in the Section 2.1, we present numerical results for the hydrodynamic loading acting on a thin beam undergoing small transverse oscillations in an unbounded fluid domain for a particular Reynolds number $Re = 1$. The pressure differences on the top and bottom surfaces across an infinitely thin ribbon is shown in the Figures 2.2 - 2.4 with the imaginary component of the pressure representing the added mass and the real component of the pressure representing the dissipative effects.

The solution for hydrodynamic loading acting on a single beam of finite width and negligible thickness undergoing small transverse vibrations in an unbounded fluid domain is validated against Tuck's results [57] with the number of discretization elements being $N = 49$. Sader et al. [53] numerically fitted Tuck's results for transverse vibrations of rectangular cross-section microcantilevers and expressed it as a function of the circular cylinder hydrodynamic function.

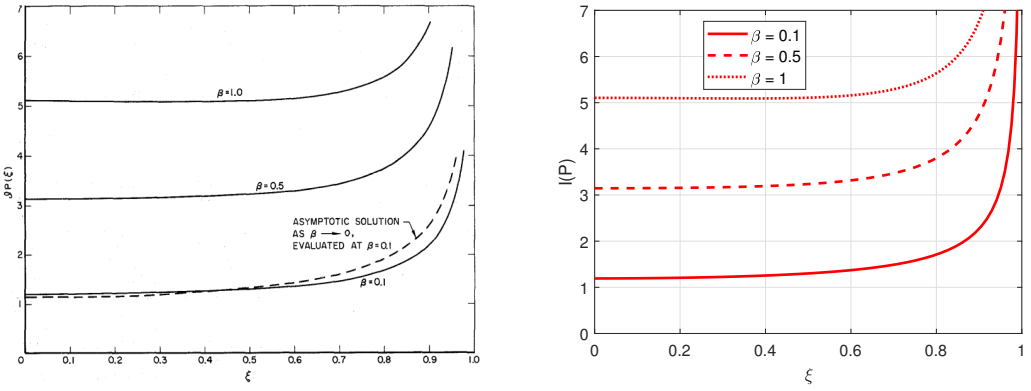

Figure 2.2: Variation of the imaginary part of pressure difference across the ribbon at low frequencies (a) Tuck's results [left panel] validation of our results against Tuck's [right panel].

The imaginary part of pressure is in phase with the acceleration of the beam and hence, is proportional to the added mass. The real part of pressure in phase with velocity of the beam and hence, is proportional to the dissipative effects. Note that we lack a sufficient density of intervals near the edges of the beam causing pressure

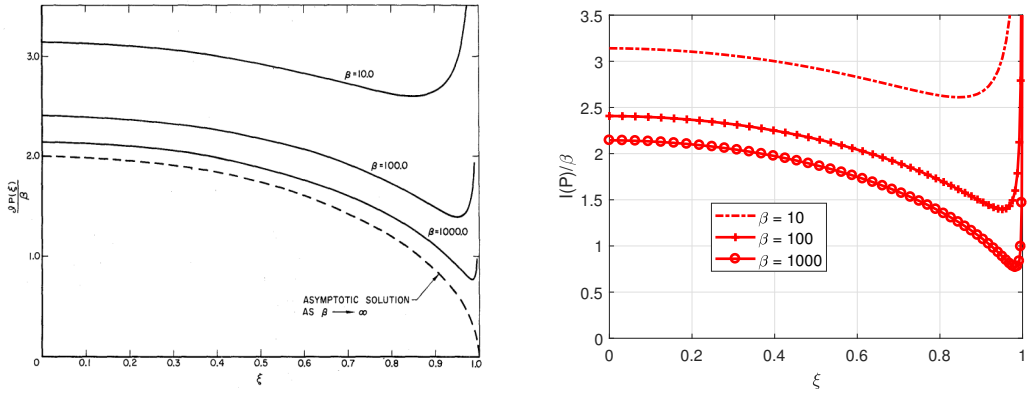

Figure 2.3: Variation of the imaginary part of pressure difference across the ribbon at high frequencies scaled with respect to β Tuck's results [left panel] and validation of our results against Tuck's [right panel].

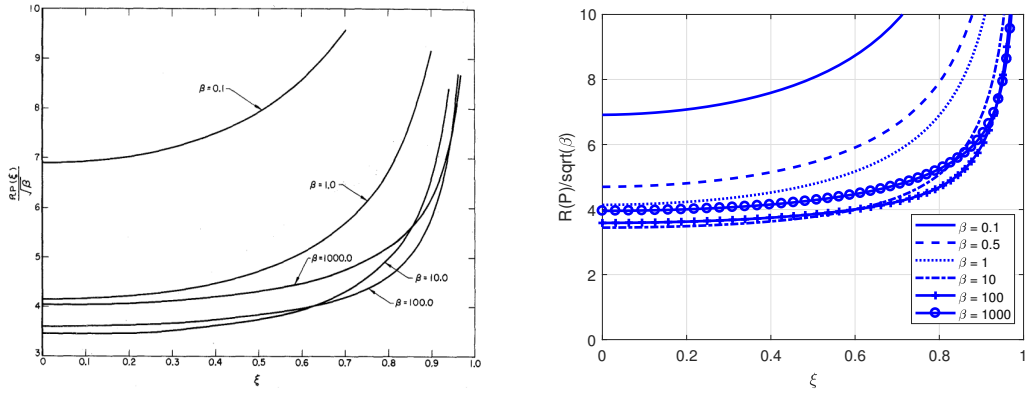

Figure 2.4: Variation of the real part of pressure difference across the ribbon at low and high frequencies scaled with respect to $\sqrt{\beta}$ Tuck's results [left panel] and validation of our results against Tuck's [right panel].

jumps towards the edges, in particular with increasing Reynolds numbers resulting in a loss in accuracy of the numerical solution. We do observe the manifestation of Stokes' Paradox [56] with the limiting solution for velocity of the beam in the lateral direction not satisfying the boundary condition at infinity, the details of which are provided by Tuck [57].

2.3 Hydrodynamic coupling of a pair of beams

Basak and Raman [5] defined the microbeams to be hydrodynamically decoupled when the hydrodynamic loading over each microbeam in the array is 99% of that on an isolated microbeam. We consider the scenario in which both beams are actuated at their maximum amplitudes i.e. 1-1 configuration. The nondimensional transverse force per unit length on microbeam 1 as a function of $\bar{g}$ is plotted for different Re values and is validated against the results provided by Basak and Raman.

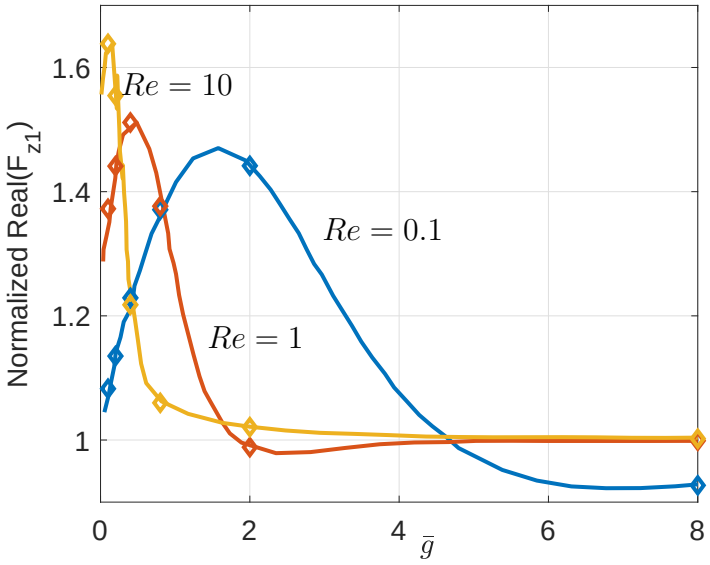

Figure 2.5: Variation of the real part of nondimensional hydrodynamic force across microbeam 1 for two beams vibrating in-phase (1-1 configuration) over $\bar{g}$ normalized by their corresponding values at the same Re in an unbounded fluid with solid lines representing Basak's results and markers our validation against it.

A higher Re results in smaller boundary layer thickness since it scales as $Re^{-1/2}$ implying that the pressure and velocity fields are more localized resulting in weak interactions between beams in the array. Also increasing Re may have nonlinear effects invalidating the existing model. However, for lower Re, as a result of overlapping boundary layers a significant difference can be noticed as the hydrodynamic loading approaches it's corresponding isolated beam value at a larger gap compared to a higher Re [5].

Though Basak and Raman have defined two beams to be hydrodynamically decoupled when the hydrodynamic loading on each beam reaches 99% of it's corresponding value of an isolated beam vibrating in an unbounded fluid domain, the relative effects of microbeam 1 on microbeam 2 do not give any useful information about the mutual coupling. For instance, for any gap between the microbeams the ratio of hydrodynamic loading on beam 2 with respect to beam 1 is always 1 for this particular configuration in which both beams oscillate in-phase. Hence, in our work we define "coupling" as the relative influence of the active beam on the passive beam and hence, we excite beam 1 and keep beam 2 passive (1-0 configuration) to study the mutual coupling effects unlike Raman who studied the 1-1 configuration.

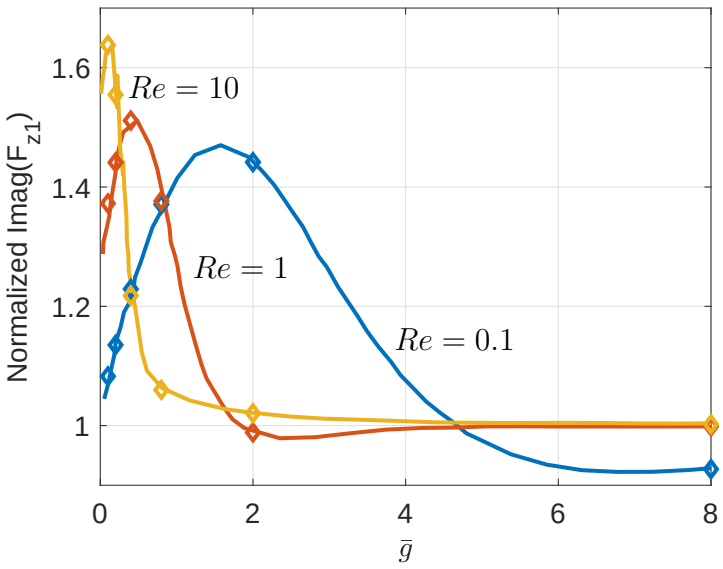

Figure 2.6: Variation of the imaginary part of nondimensional hydrodynamic force across microbeam 1 for two beams vibrating in-phase (1-1 configuration) over $\bar{g}$ normalized by their corresponding values at the same Re in an unbounded fluid with solid lines representing Basak's results and markers our validation against it.

Here, we plot the real and imaginary parts of hydrodynamic force over both active and passive beams to see the mutual coupling effects.

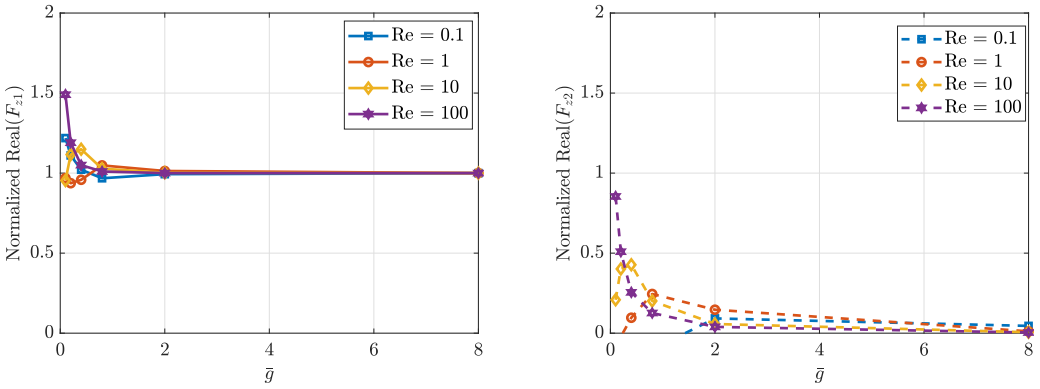

Figure 2.7: Variation of the real part of hydrodynamic force over (a) beam 1 and (b) beam 2 for different Re and $\bar{g}$ normalized by its corresponding value at the same Re in an unbounded fluid domain (1-0 configuration).

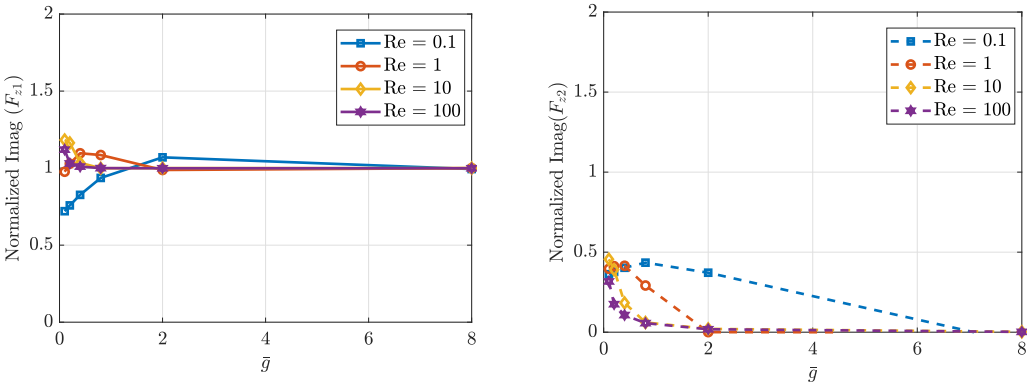

Figure 2.8: Variation of the imaginary part of hydrodynamic force over (a) beam 1 and (b) beam 2 for different Re and $\bar{g}$ normalized by its corresponding value at the same Re in an unbounded fluid domain (1-0 configuration).

2.4 Hydrodynamic coupling in arrays

We focus in this section on the hydrodynamic coupling effects between members in an array. We provide a generalized matrix formulation for an array of beams incorporating coupling contributions of all members and study the influence of non-neighbouring members in a three- and a five-beam array.

Derivation of the hydrodynamic coupling matrix of the nearest neighbour model is based on existing work by Basak and Raman [5] whereas our new contribution in this work is the consideration, analysis and discussion of coupling contributions of all members. We consider identical beams (similar dimensions and geometrical properties) equally spaced apart. The width of each beam is $2b$ and the gap between members is $2g$. The unsteady streamfunction in Equation 2.5 is computed for transverse vibrations and the velocity matching conditions are formulated for M beams. The transverse velocity of the m^{th} beam in the array is given by $W_m(z) = \hat{W}_m e^{i(\omega t+\theta_m)}$, where $\hat{W}_m$ is the velocity amplitude and θ_m is the phase of vibration of the m^{th} beam. Also velocity matching conditions for each beam is formulated following a similar procedure as that by Basak and Raman [5]. We nondimensionalise gaps, pressure differences, velocity amplitudes and unsteady Reynolds number to make comparisons meaningful. The uncoupled integral equations are then solved using a numerical procedure similar to the one used by Tuck [57] and Basak and Raman [5]. The hydrodynamic matrix elements for an array of M beams incorporating interactions between all members in the array are given by

$$G_{m,n} = \left[A_{kj}\right]_{m,n},$$

where $m, n \in 1...M$ and A_{kj} is given by

$$\begin{aligned} A_{kj} &= \int_{\xi_j}^{\xi_{j+1}} L(\sqrt{iRe}|\xi' - \xi|)d\xi', \\ &= \frac{1}{2\pi}[f(Re, \xi'_{j+1}, \xi_k) - f(Re, \xi'_j, \xi_k)], \end{aligned} \tag{2.8}$$

where the kernel function

$$L = \Psi_{\xi\xi'}$$

is obtainable from [57]
and

$$f(Re,\xi_j{}',\xi_k) = \frac{i}{Re}\left(\frac{1}{\xi_j'-\xi_k} + sgn(\xi_j'-\xi_k)i\sqrt{iRe}K_1 \times(-i|\xi_j'-\xi_k|\sqrt{iRe})\right). \tag{2.9}$$

where ξ_j' is any node on the beam, ξ_k is the midpoint between any two nodes, K_1 is the modified Bessel function of the third kind.

Each diagonal entry contains hydrodynamic influence coefficients due to the segments of the same microbeam whereas each off diagonal entry comprises of elements representing the hydrodynamic coupling generated by the neighbouring ($(m+1)^{th}$ and $(m-1)^{th}$) and non-neighbouring members on the m^{th} beam. For example, G_{11} in the coupling matrix contains hydrodynamic influence coefficients on the first microbeam due to the segments of the same microbeam whereas G_{12} contains hydrodynamic influence coefficients on the first microbeam due to the segments of the second microbeam, and so on. Equations are designed to hold at the midpoint of each segment while the square-root singularities at the edges are taken care of by dividing each beam into unequal number of segments N. In order to compute the elements of sub-matrix G_{11} a loop is run over the number of nodes j $(0,...,N)$ for each k $(0,...,N-1)$ which is the midpoint of each segment on the first beam [57].

The velocity matching equations when the left-most beam is active while the rest are passive (1-0-0, 1-0-0-0-0) can be written in matrix notation as follows:

$$[1\,0...0]^T = \hat{\boldsymbol{G}}[P_m]^T, \tag{2.10}$$

Note that in Chapter 3 (p.44) when the wall equations are ignored, one obtains an uncoupled set of equations in the transverse and lateral directions. This can then be simplified to equation (2.10) with the left-most beam active and the rest passive from which the unknown pressures can be obtained as follows:

$$\left[\boldsymbol{P}\right] = \left[\hat{\boldsymbol{G}}\right]^{-1}\left[\boldsymbol{V}\right] \tag{2.11}$$

The coupling matrix $\hat{\boldsymbol{G}}$ incorporating all member interactions for a three and a five-beam array are given by:

$$\hat{\boldsymbol{G}}_{\boldsymbol{III}} = \begin{bmatrix} G_{11} & G_{12} & G_{13} \\ G_{21} & G_{22} & G_{13} \\ G_{31} & G_{32} & G_{33} \end{bmatrix},$$

$$\hat{\boldsymbol{G}}_{\boldsymbol{V}} = \begin{bmatrix} G_{11} & G_{12} & G_{13} & G_{14} & G_{15} \\ G_{21} & G_{22} & G_{23} & G_{24} & G_{25} \\ G_{31} & G_{32} & G_{33} & G_{34} & G_{35} \\ G_{41} & G_{42} & G_{43} & G_{44} & G_{45} \\ G_{51} & G_{52} & G_{53} & G_{54} & G_{55} \end{bmatrix},$$

where the elements in red represent the coupling contributions of non-neighbouring members and are set to zero as in previous work [5, 25, 58] for only considering nearest neighbour interactions. The solutions for the nondimensional pressure jump are found simply by inverting the coupling matrix $\hat{\boldsymbol{G}}$ and multiplying it by the velocity vector. Once the pressure differences across the beams are calculated the corresponding nondimensional hydrodynamic force per unit length acting on the beams is given by:

$$\bar{F}_z = \Sigma P_{i,j}(\xi'_{j+1} - \xi'_j) \tag{2.12}$$

where i is the respective beam under consideration.

2.5 Results

Nondimensional parameters that influence the coupled hydrodynamics are the gap $\bar{g} = g/b$, the amplitude ratio r_{m1}, the relative phase θ_{m1}, the unsteady Reynolds number Re and the non-neighbouring members. The effect of the first four parameters have been studied for nearest neighbour interactions [5]. The focus in this chapter is on the influence of non-neighbouring members and on the mutual coupling for different gaps for two different arrays, a three- and a five-beam array.

2.5.1 Three-beam array

The influence of the gaps between the beams and the effect of non-neighbouring members on the overall array dynamics are analyzed by comparing the imaginary, real and absolute values of hydrodynamic loading over the beams for different Reynolds numbers. Also, we consider different actuations in the form of 1-0-0, 0-1-0 and 1-1-1 configurations in which 1 denotes the active beam and 0 denotes the passive beam in order to compare the coupling ratios when the position of the actuated beam is varied (1-0-0 and 0-1-0 cases) but not in the 1-1-1 case since we do not get to see any useful information about the mutual coupling effects as described in Section 2.3. However, we study the overall hydrodynamic loading profile in the 1-1-1 case for different Reynolds numbers.

Effect of the gap

Below we present our analysis of the influence of gaps by considering only nearest neighbour influence at $Re = 1$ as an example. The leftmost beam in the following figures is the active beam actuated with a constant velocity amplitude.

We observe that when the beams are far apart from each other (solid lines) i.e. for a gap of $\bar{g} = 8$, beams 2 and 3 are hydrodynamically decoupled from beam 1. Also, the pressure difference across the width of the beams is symmetric for larger gaps. However, as the gaps between the beams decrease, the passive beams become hydrodynamically coupled, with beam 2 being significantly influenced (28

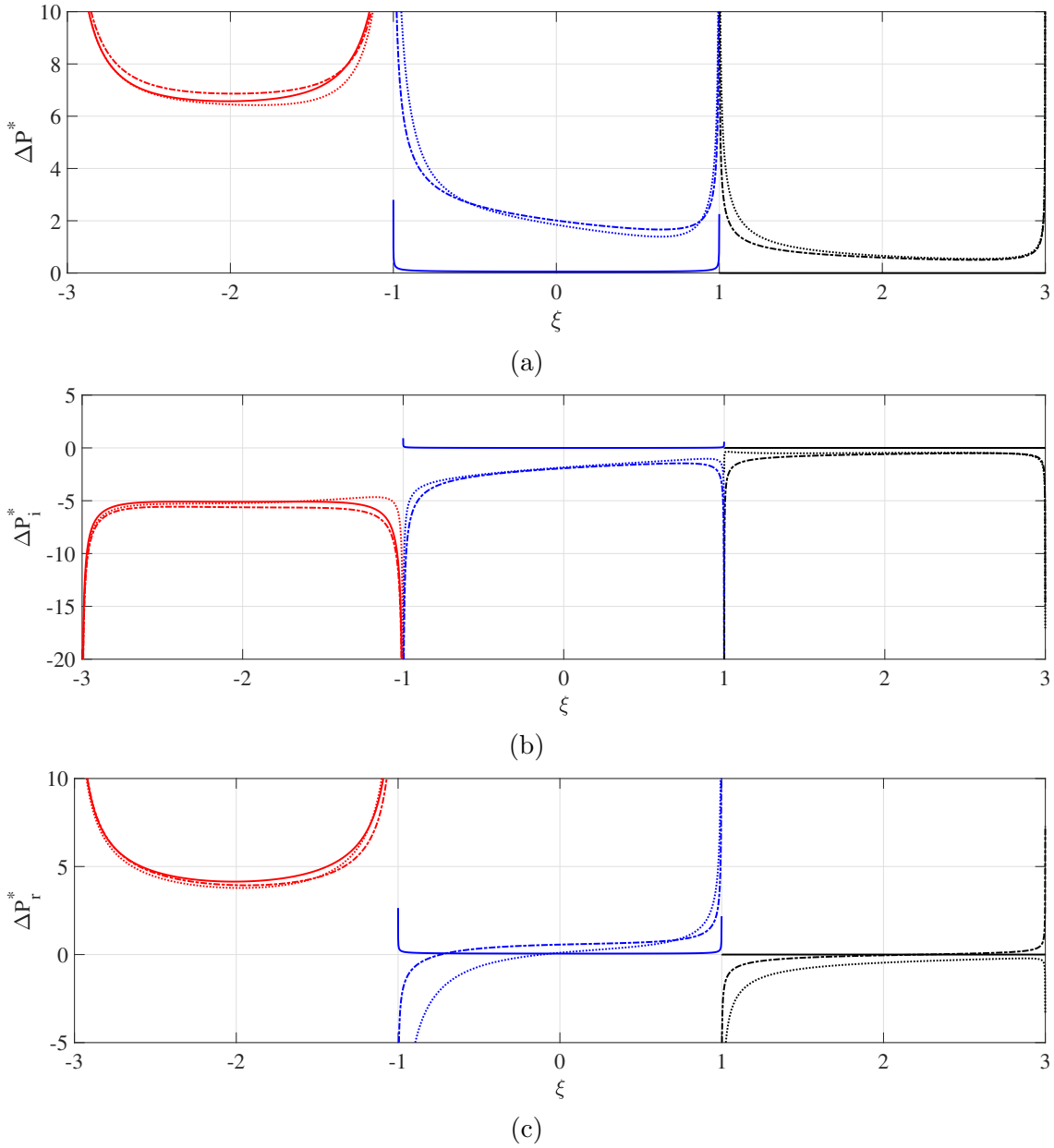

Figure 2.9: Variation of the (a) absolute, (b) imaginary and (c) real values of nondimensional pressure difference across three beams incorporating only nearest neighbour influence at $Re = 1$; solid lines: $\bar{g} = 8$, dash-dotted lines: $\bar{g} = 0.4$, dotted lines: $\bar{g} = 0.1$ for a 1-0-0 configuration.

%) in comparison to beam 3 (10 %) implying that the coupling strength decreases with increasing distances from the active beam. Note that the percentage of coupling influence is calculated by taking ratios of the pressures at the midpoints of the passive beam with respect to the active beam. The pressure differences across the width of the beams become asymmetric when the gaps decrease between the beams indicating a pressure profile over the array as a whole rather than many individual beams confirming the presence of hydrodynamic coupling.

The imaginary and real parts of nondimensional pressure jump across the three beams are plotted in Figure 2.9, for different nondimensional gaps $\bar{g} = g/b$ between

the beams at $Re = 1$. In Figure 2.10 and Figure 2.11 we observe that as the gaps between the beams decrease, the added mass and damping behave in non-intuitive ways. Computing the added mass and damping effects at the midpoint of each beam we find that as $\bar{g}$ decreases they display a non-monotonic behaviour. Also, the range of $\bar{g}$ over which added mass and damping display this behavior is different, for instance the critical gaps for added mass is $\bar{g} = 0.4$ while for damping it is $\bar{g} = 0.8$ which agrees with the existing results in literature resulting in constructive or destructive zones of hydrodynamic interference [5].

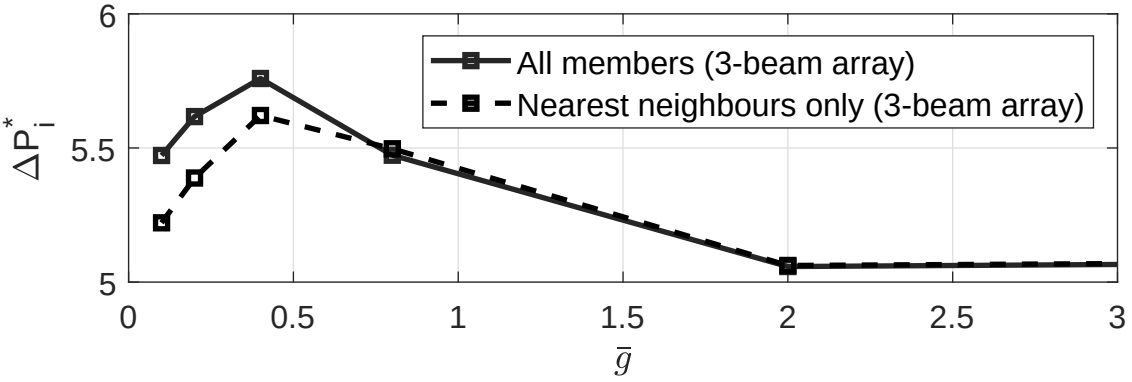

Figure 2.10: Imaginary parts of nondimensional pressure evaluated at the mid point of the active beam in a three-beam array (1-0-0 configuration) at $Re = 1$ for different nondimensional gaps; nearest neighbours only (dashed lines) and all members incorporated (solid lines).

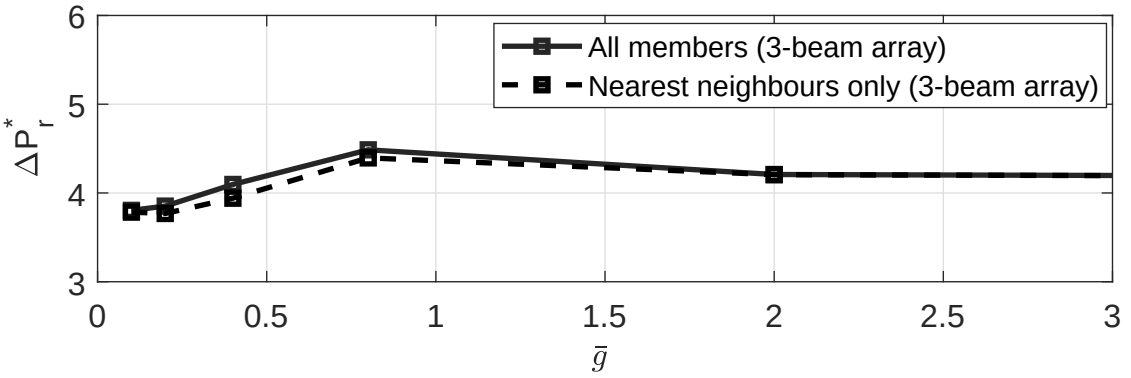

Figure 2.11: Real parts of nondimensional pressure evaluated at the mid point of the active beam in a three-beam array (1-0-0 configuration) at $Re = 1$ for different nondimensional gaps; nearest neighbours only (dashed lines) and all members incorporated (solid lines).

Effect of the non-neighbouring members

Next, we consider the influence of all members and plot the differences in absolute, imaginary and real parts of nondimensional pressure when all beams are incorporated and only when nearest neighbours are incorporated to study the influence of non-neighbouring members.

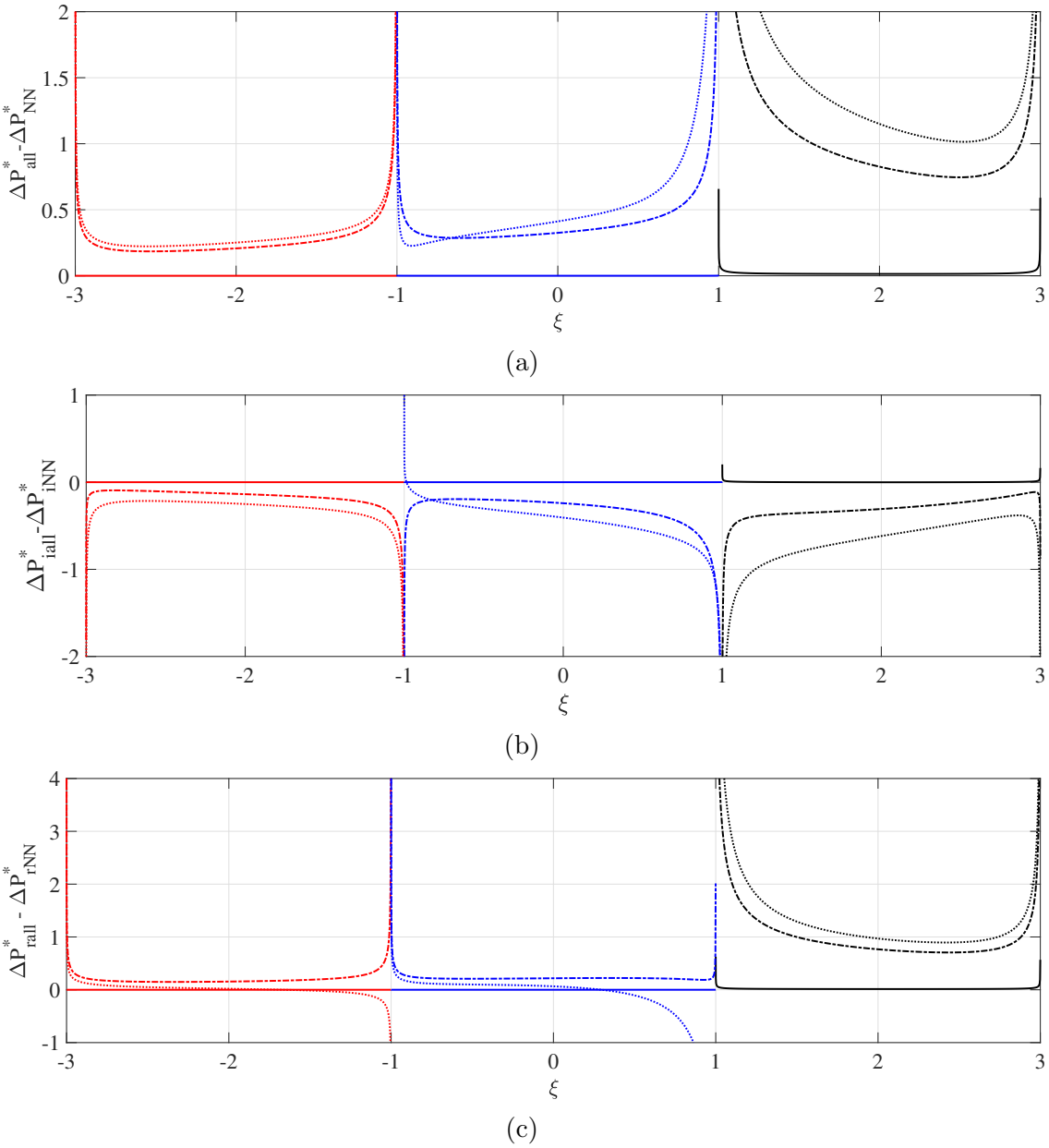

Figure 2.12: Difference in (a) absolute, (b) imaginary and (c) real values of nondimensional pressure difference across three beams incorporating all members and when only nearest neighbors are incorporated at $Re = 1$; solid lines: $\bar{g} = 8$, dash-dotted lines: $\bar{g} = 0.4$, dotted lines: $\bar{g} = 0.1$ for a 1-0-0 configuration.

For a nondimensional gap $\bar{g} = 8$, the pressure difference represented by the solid line is zero implying that non-neighbouring members do not affect the array dynamics and hence, can be neglected as each beam behaves as a single beam vibrating in an unbounded fluid domain for larger gaps. As the gap decreases between the beams, the significance of non-neighbouring beams increases with decreasing gaps and hence, contribute significantly to the overall dynamic behaviour. Also, unlike the case with only nearest neighbours considered in which the hydrodynamic coupling strength decreases with increasing distances from the active beam, here we notice an increase in coupling strength on beam 3 when non-neighbouring beams are incorporated. This implies that there is transfer of energy not only between

nearest neighbours but between non-neighbours as well, especially significant for smaller gaps i.e. $\bar{g} < 0.4$. The pressure difference on beam 3 (0.82) at a critical gap of $\bar{g} = 0.4$ is comparatively higher than that of beam 2 (0.32), implying that the non-neighbouring beams do play a significant role.

We now investigate the significance of non-neighbouring members by plotting the differences in imaginary and real parts of pressure when all members are incorporated and compare it to the results of when only nearest neighbours are incorporated. From Figure 2.12 we observe that the added mass and damping computed at the midpoint of beam 3 is higher in comparison to beam 2. Hence, beam 3 is significantly influenced when non-neighbouring beams are incorporated. When the effect of non-neighbouring beams are ignored the beam closest to the active beam is significantly coupled and the coupling strength decreases with decreasing distances from the active beam. However, non-intuitive behavior on beam 3 signifies that non-neighbouring beams do play a significant role and hence, cannot be ignored especially with decreasing gaps as they affect the overall array dynamics. Note (on beam 1), that there is also a difference on beam 1, not only beams 2 and 3.

Coupling effects

1-0-0 We consider the case in which only nearest neighbours are accounted for denoted by dashed lines and also the case in which we incorporate all members denoted by solid lines. The outputs are the imaginary and real parts of the hydrodynamic loading acting over all three beams as presented before. However, here it is valuable to present the coupling ratios i.e. the ratio of absolute values of nondimensional hydrodynamic force over passive beam ($\bar{F}_p$) to that of the active beam ($\bar{F}_a$). The reader is referred to Equation 2.12 for the definition of nondimensional hydrodynamic force. Note that F_{21} and F_{31} denote the ratio of hydrodynamic forces of the passive beams (2 and 3, respectively) with respect to the active beam 1 and is presented in Figure 2.13 for different Reynolds numbers.

Note, that the 0-0-1 configuration is symmetric to the 1-0-0 configuration and therefore not presented here. We observe that for lower Reynolds numbers i.e. $Re = \{0.1,\ 1\}$ in Figures 2.13a and 2.13b, there is a marked difference for the effect of non-neighbouring members. This can be explained by the fact that the boundary layers overlap whereas for higher Reynolds numbers i.e $Re = \{10,\ 100\}$ the influence of non-neighbouring members can be neglected (inviscid flow limit) in Figures 2.13c and 2.13d. The reader is referred to Section 2.3 for the physics that describes the boundary layer thickness for different Reynolds numbers.

0-1-0 We consider the case in which the middle beam is active while the outer beams are passive to investigate if shifting the position of the active beam in the array alters the mutual coupling. Note that the ratio of any outer beam to the middle beam is the same. Hence, we only plot the ratio of one of the outer beams to the middle beam i.e. beam 1 (leftmost) with respect to beam 2 in Figure 2.14.

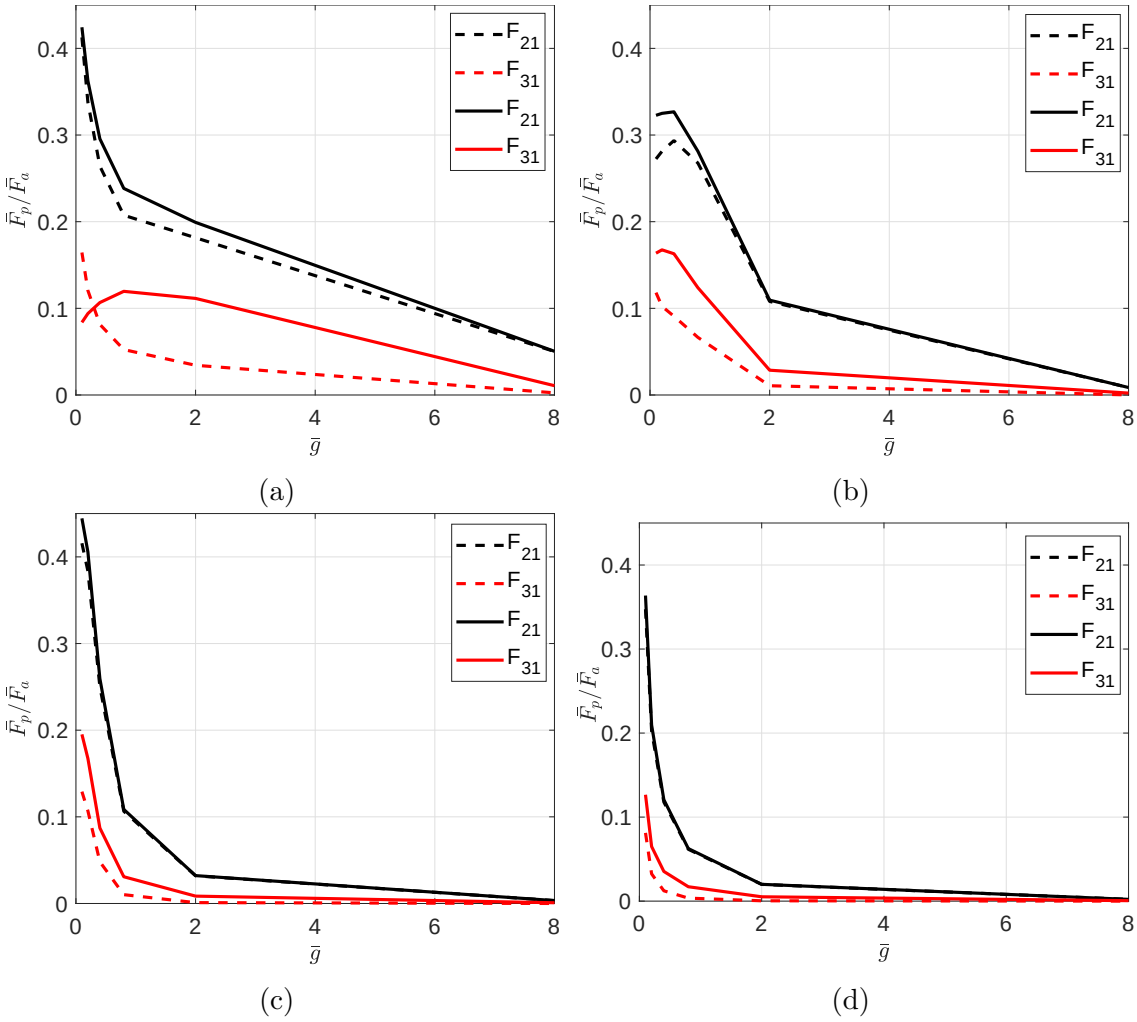

Figure 2.13: Coupling ratios of the passive beam with respect to active beam over a range of gaps in a three-beam array for the 1-0-0 configuration at (a) $Re = 0.1$, (b) $Re = 1$, (c) $Re = 10$ and (d) $Re = 100$; nearest neighbours only (dashed lines) and all members (solid lines).

A similar trend can be observed in the 0-1-0 configuration in which for larger Re as seen in Figures 2.14c and 2.14d, one can ignore the effects stemming from non-neighbouring members. A comparison between the 1-0-0 and a 0-1-0 configuration shows that there are significant differences in the coupling ratios of passive cantilever with respect to the cantilever, in particular at lower Reynolds numbers with the coupling being higher for the 1-0-0 case at smaller gaps (compare Figures 2.13a and 2.14a).

1-1-1 In this case all three beams are excited to investigate how the overall hydrodynamic loading over individual beams and the whole array varies with different Reynolds numbers.

We observe that when the beams are in close proximity to each other, i.e. $\bar{g} = 0.1$, the hydrodynamic loading across the three beams remains constant when only nearest neighbour effects are incorporated as seen in Figure 2.15a. However, when non-

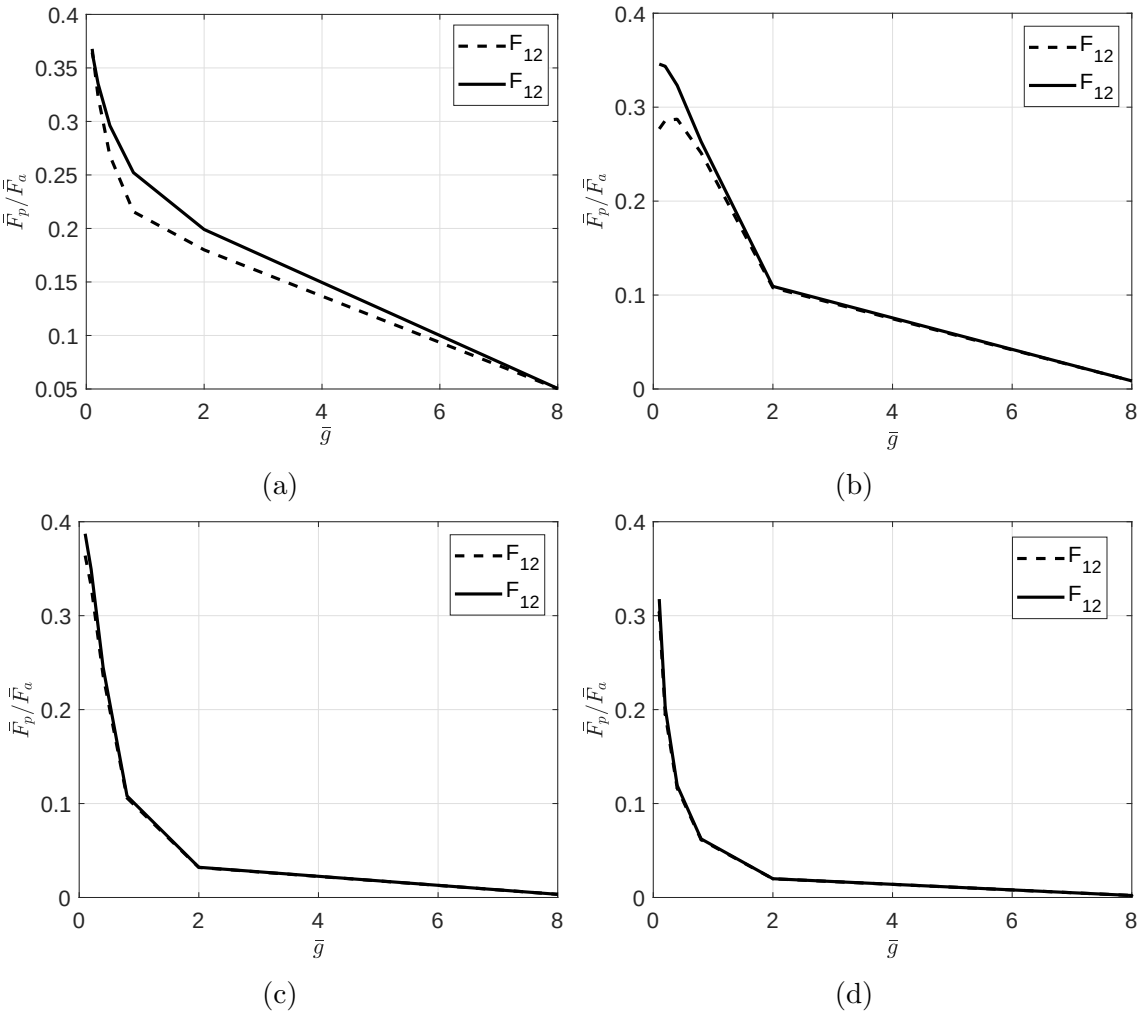

Figure 2.14: Coupling ratios of the passive beam with respect to active beam over a range of gaps in a three-beam array for the 0-1-0 configuration at (a) $Re = 0.1$, (b) $Re = 1$, (c) $Re = 10$ and (d) $Re = 100$; nearest neighbours only (dashed lines) and all members (solid lines).

neighbouring members are incorporated we notice a concave pressure profile across three beams for $\bar{g} = 0.1$ (Figure 2.15b), implying that the pressure profile cannot be ignored for predicting the overall hydrodynamic loading effects with respect to real life applications. This can be explained by the overlapping viscous layers (see Section 2.3) when in close proximity resulting in reduced hydrodynamic load on the middle beam. When the three beams are far apart, i.e. $\bar{g} = 8$, the hydrodynamic loading across three beams remains fairly constant irrespective of the non-neighbouring member effects, see Figure 2.15.

When all three beams are excited at a higher $Re = 100$ (see Figure 2.16), we note that the overall hydrodynamic loading profile across three beams is concave down when the beams are close to each other whereas when they are far apart it remains fairly constant. The change in overall hydrodynamic loading observed when the beams are close to each other ($\bar{g} = 0.1$) with the inclusion of non-neighbouring members is significant in the case of $Re = 0.1$ compared to that at $Re = 100$ (compare Figure 2.15 and Figure 2.16). This can be explained by the fact that the

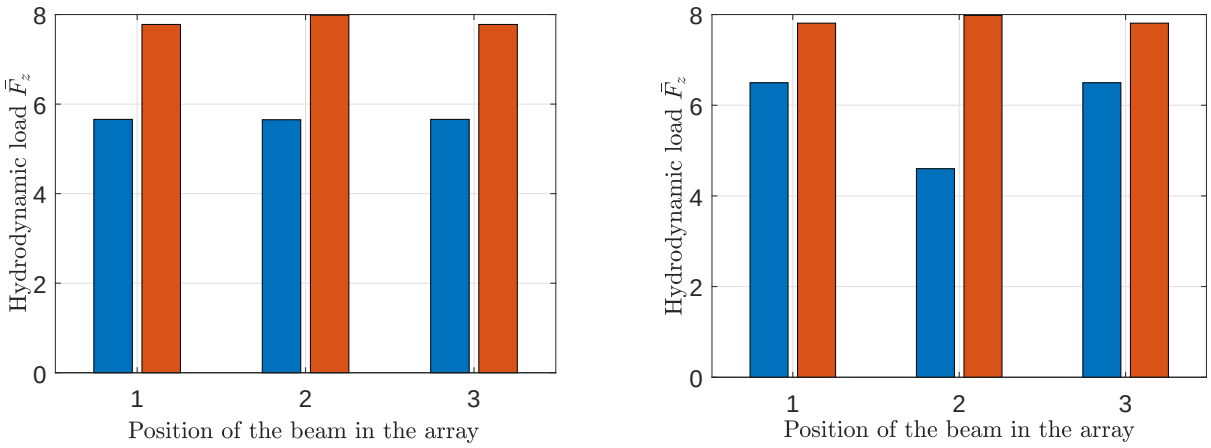

Figure 2.15: Variation of the overall hydrodynamic load over three beams for $Re = 0.1$ in an unbounded fluid domain for two different gap widths $\bar{g} = 0.1$ (blue) and $\bar{g} = 8$ (orange); (a) with nearest neighbours only and (b) with all members incorporated for a 1-1-1 configuration.

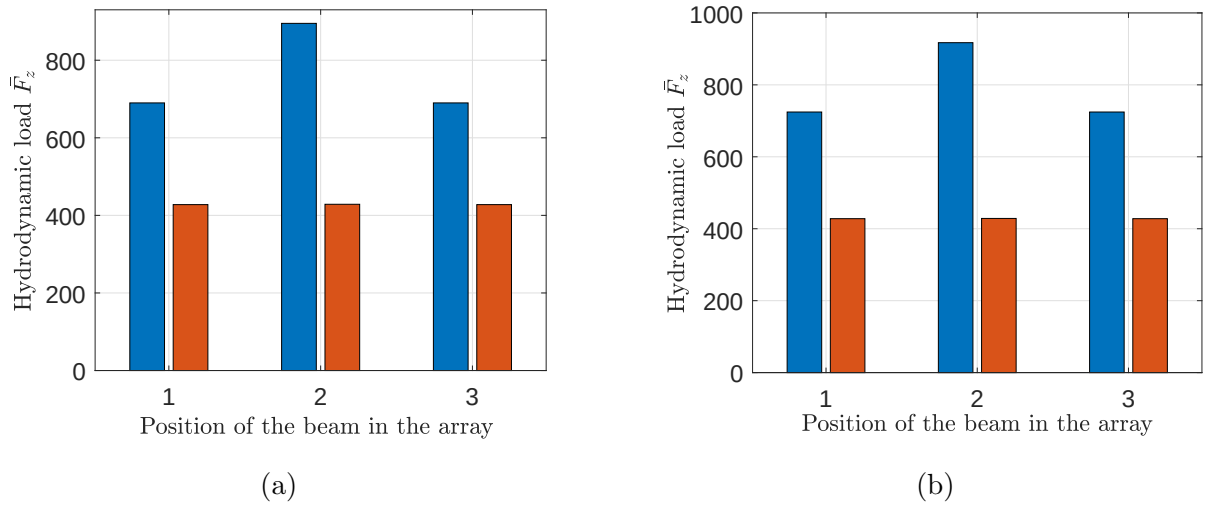

Figure 2.16: Variation of the overall hydrodynamic load over three microbeams for $Re = 100$ in an unbounded fluid domain for two different gap widths $\bar{g} = 0.1$ (blue) and $\bar{g} = 8$ (orange); (a) with nearest neighbours only and (b) with all members incorporated for a 1-1-1 configuration.

boundary layers are really thin for higher Re and hence, a fairly constant load is observed when the beams are far apart ($\bar{g} = 8$) irrespective of the incorporation of non-neighbouring member effects. However, when in close proximity a small overlap in the boundary layers results in increased loading over the middle beam and the additional load increase on top of it can be noticed when non-neighbouring members are incorporated (compare Figure 2.16a and Figure 2.16b).

2.5.2 Five-beam array

A similar structure is followed as in the case of a three-beam array in which we study the influence of the gaps between the beams and the effect of non-neighbouring members on the overall array dynamics by comparing the absolute, imaginary and real values for different Reynolds numbers for the 1-0-0-0-0 configuration.

Effect of the gap

Below, we perform a similar analysis on an array comprising of five beams with a constant amplitude on beam 1 while the remaining beams are passive and as an example we present the pressure profiles for $Re = 1$.

We observe again that when the beams are far apart i.e. for a gap of $\bar{g} = 8$, all passive beams are hydrodynamically decoupled from beam 1 (beam 1 is moving while beams 2 - 5 are stationary). As the distance from the active beam increases, the hydrodynamic coupling strength decreases for the passive beam under consideration. Also we notice a similar trend in pressure difference distribution for larger gaps with it being symmetric and for increasing influence the nondimensional pressure jump becomes distorted and asymmetric.

The imaginary and real parts of nondimensional pressure difference across the five beams are plotted in Figure 2.17 for different nondimensional gaps $\bar{g}$ between the beams for $Re = 1$. The added mass and damping display a non-monotonic trend here as observed in a three-beam array with the magnitude of added mass (compare Figure 2.10 and Figure 2.18) and damping (Figure 2.11 and Figure 2.19) being more significant to that in a three-beam array at the same critical gaps.

Effect of the non-neighbouring members

Next, we consider the influence of all members and plot the differences in absolute, imaginary and real parts of nondimensional pressure when all beams are incorporated and when only nearest neighbors are incorporated to study the influence of non-neighbouring members in a five-beam array at a particular Reynolds number $Re = 1$.

A similar effect is observed as in the case of a three-beam array for a nondimensional gap $\bar{g} > 8$ implying that non-neighbouring members can be neglected for such gaps as they do not affect the overall array dynamics, see figure 2.20. However, they increasingly become significant with decreasing gaps between the beams and with increasing array size. From figure 2.20 we note that the active beam (beam 1) is also affected when non-neighbouring members are incorporated and not just the passive beams i.e. (beam 2, beam 3, beam 4 and beam 5) further strengthening our argument from the case of a three-beam array of the onset of array effects with increasing size of the array and decreasing gaps. This implies that one cannot ignore the collective dynamics with increasing size of the array and in particular for decreasing gaps.

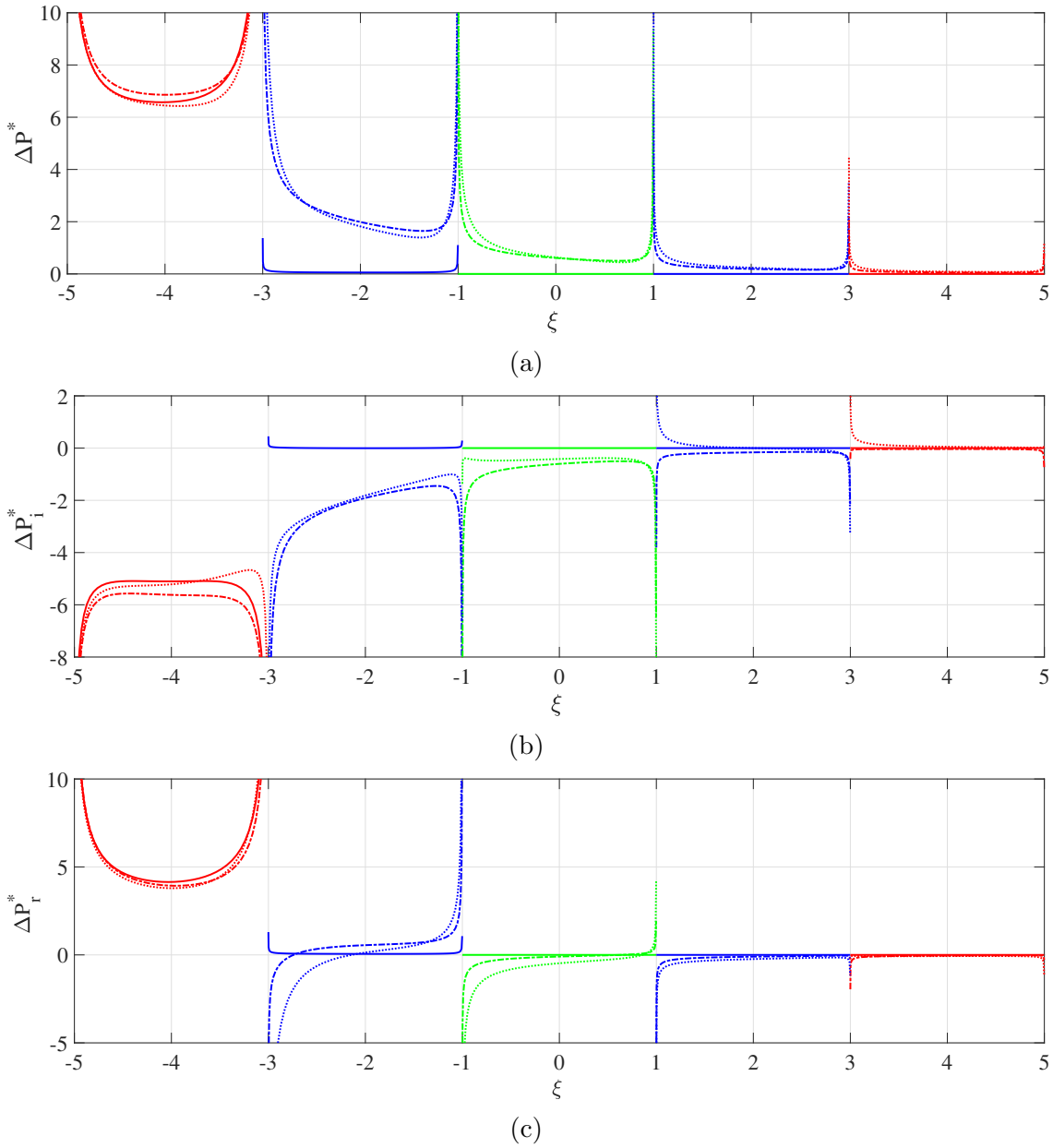

Figure 2.17: Variation of the (a) absolute, (b) imaginary and (c) real values of nondimensional pressure difference across five beams incorporating only nearest neighbour influence at $Re = 1$; solid lines: $\bar{g} = 8$, dash-dotted lines: $\bar{g} = 0.4$, dotted lines: $\bar{g} = 0.1$ for a 1-0-0-0-0 configuration.

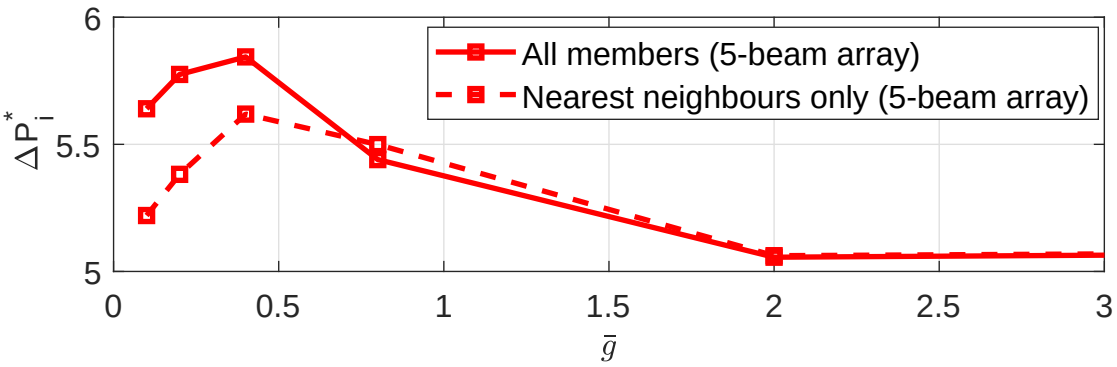

Figure 2.18: Imaginary parts of nondimensional pressure evaluated at the mid point of the active beam in a five-beam array (1-0-0-0-0 configuration) at $Re = 1$ for different nondimensional gaps; nearest neighbours only (dashed lines) and all members incorporated (solid lines).

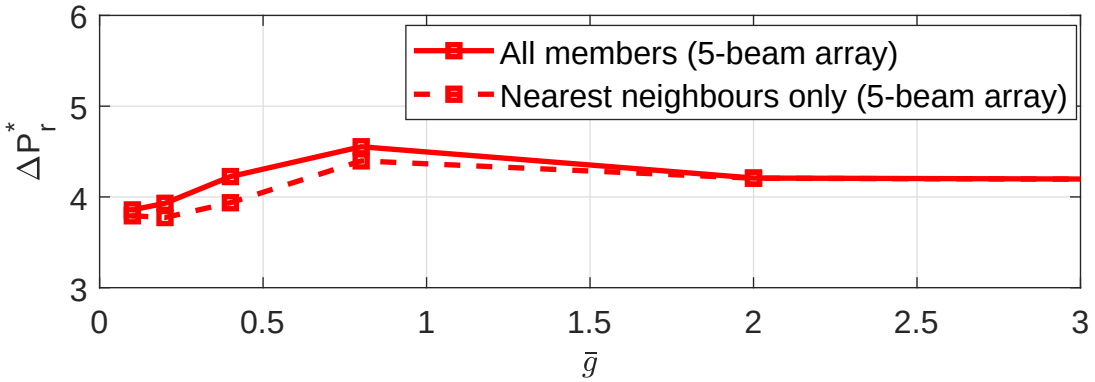

Figure 2.19: Real parts of nondimensional pressure evaluated at the mid point of the active beam in a five-beam array (1-0-0-0-0 configuration) at $Re = 1$ for different nondimensional gaps; nearest neighbours only (dashed lines) and all members incorporated (solid lines).

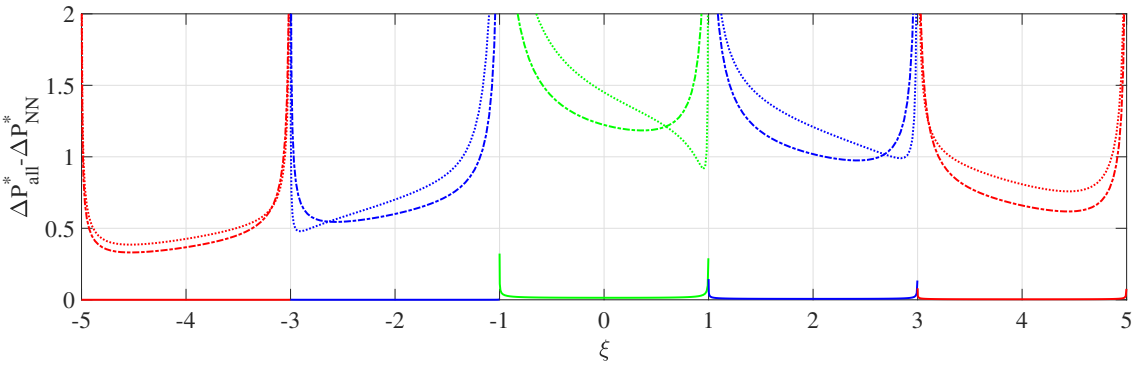

(a)

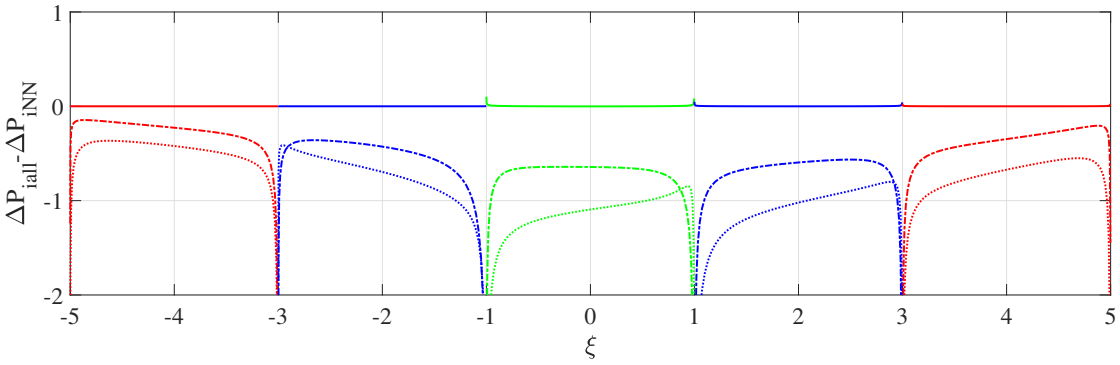

(b)

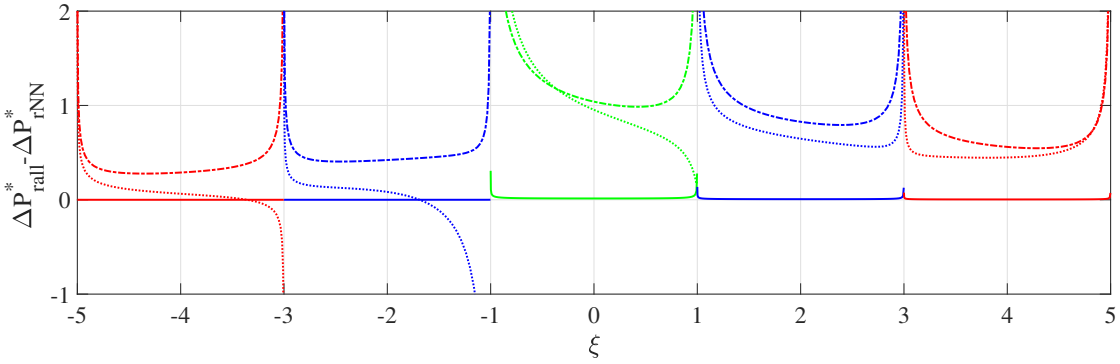

(c)

Figure 2.20: Difference in (a) absolute, (b) imaginary and (c) real values of nondimensional pressure difference across five beams incorporating all members and when only nearest neighbors are incorporated at $Re = 1$; solid lines: $\bar{g} = 8$, dash-dotted lines: $\bar{g} = 0.4$, dotted lines: $\bar{g} = 0.1$ for a 1-0-0-0-0 configuration.

2.6 Comparison of coupling effects with other array sizes

1-0-0-0-0 In this case we make a comparison between the coupling ratios of 1-0, 1-0-0 and 1-0-0-0-0 configurations to see what effect adding additional members to the array does with and without the effect of non-neighbouring members.

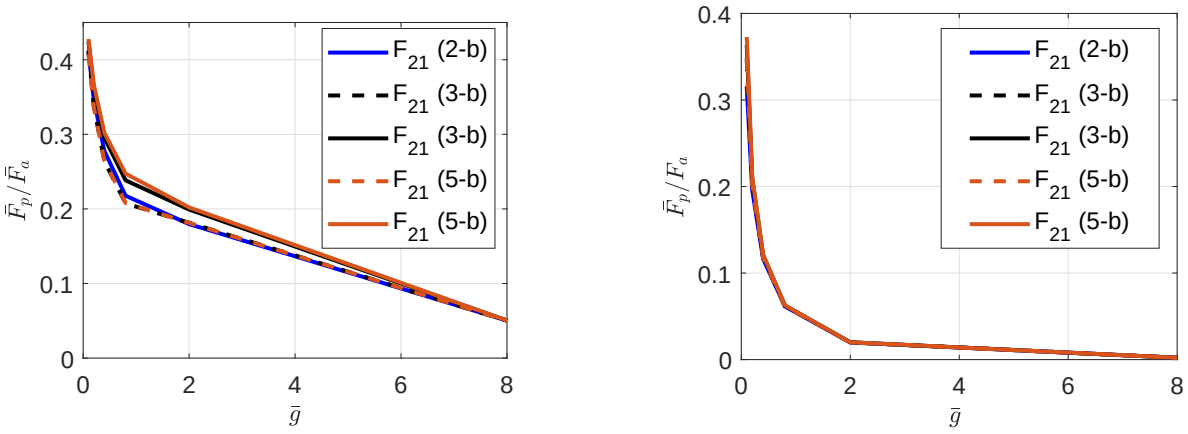

Figure 2.21: Coupling ratio of passive to active beam for different configurations for (a) $Re = 0.1$; (b) $Re = 100$; nearest neighbours:dashed line; all members:solid lines; with 1-0:blue, 1-0-0:black and 1-0-0-0-0:orange denoting the respective configurations under consideration.

F_{21} in the Figure 2.21 represents ratio of hydrodynamic loading of beam 2 (passive) with respect to beam 1 (active) for different array configurations: two-beam (2-b), three-beam (3-b) and five-beam (5b). As can be seen from the Figure 2.21, at $Re = 0.1$, the coupling ratio is slightly higher especially as the gaps get smaller with additional members in the array when all members are incorporated. Comparing the coupling ratios in a three- and a five-beam array to that of a two-beam array, we observe that when only nearest neighbours are incorporated the coupling ratio F_{21} (of a 2-b case) is underpredicted when only nearest neighbours are incorporated whereas it is overpredicted when all members are incorporated.

At $Re = 100$, no distinguishing difference is observed between the coupling ratio with and without non-neighbouring member effects, with and without additional members in the array. The reason is the boundary layers are more localized and hence, even with non-neighbouring members incorporated one cannot distinguish between a 1-0-0 and 1-0-0-0-0 configuration implying that at high Re, neither the number of members in the array nor the effect of non-neighbouring members matter due to shrinking boundary layers but can be slightly significant at very small gaps.

Also, a sharp increase in coupling can be noticed for $\bar{g} < 8$ at $Re = 0.1$ whereas it can only be seen for $\bar{g} < 2$ at $Re = 100$. This can again be attributed to the overlapping boundary layers at a much greater distance in case of low Re whereas it overlaps only at smaller gaps for high Re.

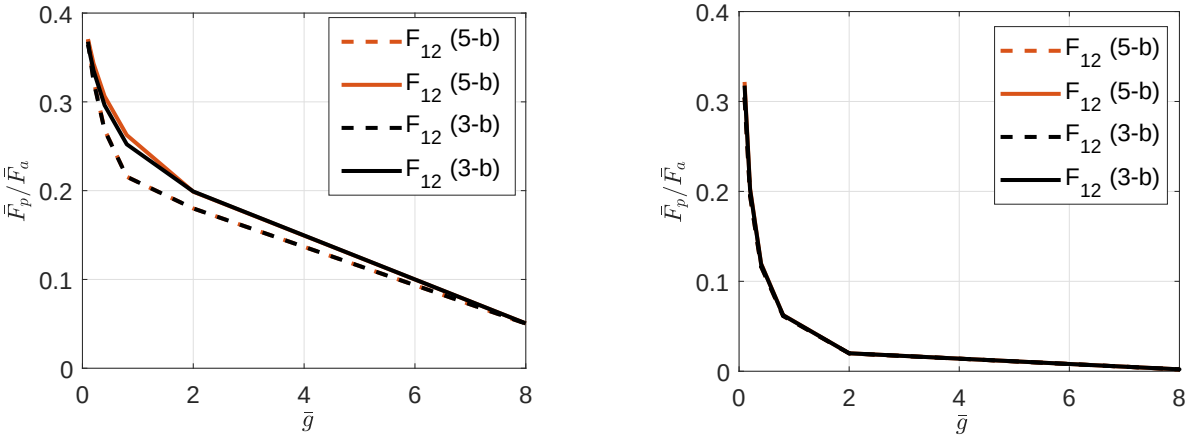

(a) (b)

Figure 2.22: Coupling ratio of passive (beam 1) to active (beam 2) for different configurations for (a) $Re = 0.1$; (b) $Re = 100$; nearest neighbours: dashed line; all members: solid lines; with 0-1-0: black and 0-1-0-0-0: orange denoting the respective configurations under consideration. (Note that the orange dashed line is beneath the black dashed line).

0-1-0-0-0 configuration Here we note that changing the position of the actuated beam in the array does affect the coupling ratio (for instance, compare Figures 2.21 and 2.22) especially for $\bar{g} < 1$ where one can note a higher ratio in the 1-0-0-0-0 case in comparison to 0-1-0-0-0 case. This can be explained by the fact that in the 1-0-0-0-0 case the actuated beam is subject to drag force from only beam 2 while in the 0-1-0-0-0 case it is subjected to drag from beams 1 and 3. Also, as seen before we observe a significant difference when non-neighbouring members are incorporated for low Re but not for high Re. Also with more members in the array at low Re, the coupling is generally higher in the case of 0-1-0-0-0 configuration compared to the 0-1-0 configuration (with all members incorporated) implying that additional beams at low Re for smaller gaps results in increased mutual coupling effects.

0-0-1-0-0 configuration In this case, we compare the coupling ratios of passive beam to active beam in a three (black) and a five-beam (orange) array. For instance, we compare the ratio of beam 1 to beam 2 in the 0-1-0 configuration and beam 2 to beam 3 in the 0-0-1-0-0 configuration. We note again that for low Re, with all members incorporated the mutual coupling in a five-beam array is higher than that of a three-beam array whereas with only nearest neighbours incorporated it is not distinguishable. The same case when performed for a high Re results in the coupling being independent of non-neighbouring members but a higher coupling can be noticed at very small gaps i.e. $\bar{g} < 0.2$ in a five-beam array compared to a three-beam array.

1-1-1-1-1 configuration In this case all five beams are excited at their maximum amplitudes.

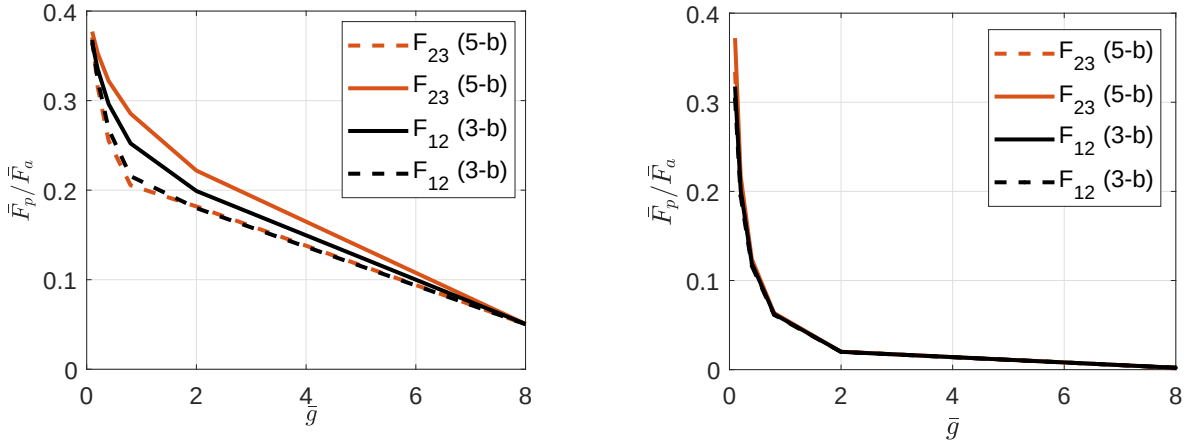

(a) (b)

Figure 2.23: Coupling ratio of passive beam to the active beam (middle) for different configurations for (a) $Re = 0.1$; (b) $Re = 100$; nearest neighbours:dashed line; all members:solid lines; with 0-1-0:black and 0-0-1-0-0:orange denoting the respective configurations under consideration.

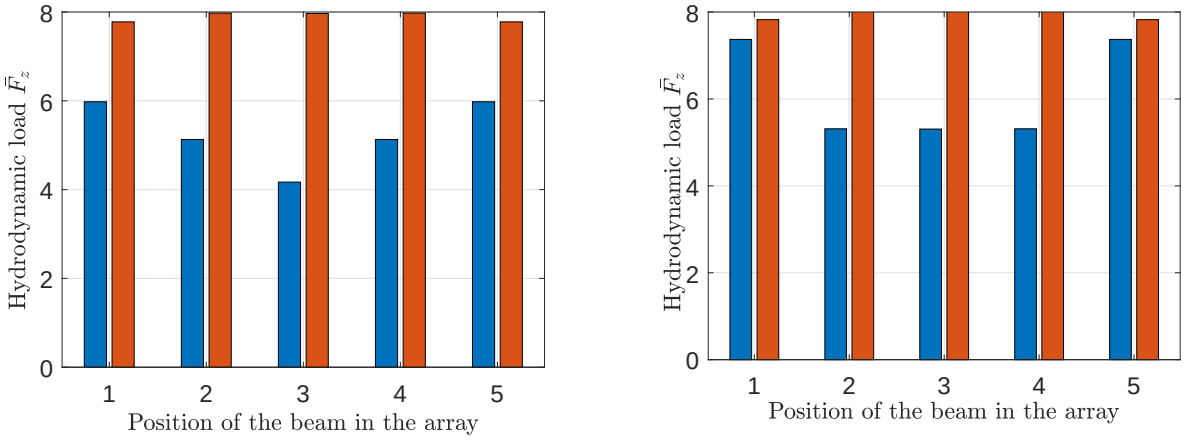

(a) (b)

Figure 2.24: Variation of the overall hydrodynamic load over five microbeams for $Re = 0.1$ in an unbounded fluid domain for two different gap widths $\bar{g} = 0.1$ (blue) and $\bar{g} = 8$ (orange), (a) with nearest neighbours only and (b) with all members incorporated for a 1-1-1-1-1 configuration.

We note that the overall hydrodynamic load has a profile that has a local minimum at the middle beam for $Re = 0.1$ while it has a local maximum at the middle beam for $Re = 100$ across five beams when the beams are close to each other i.e. $\bar{g} = 0.1$. This can be explained by the fact of overlapping viscous layers in case of low Re resulting in increased damping over the middle beam which is not the case for high Re. Also, note the difference in loading profile with the non-neighbouring members incorporated in Figure 2.24b, where the loading is flat across the three middle beams. Comparing Figure 2.24a with Figure 2.15, we can clearly observe a distinguishing feature in the loading profile when the beams are close ($\bar{g} = 0.1$) that it is parabolic in nature with increase in length of the array members i.e. in a

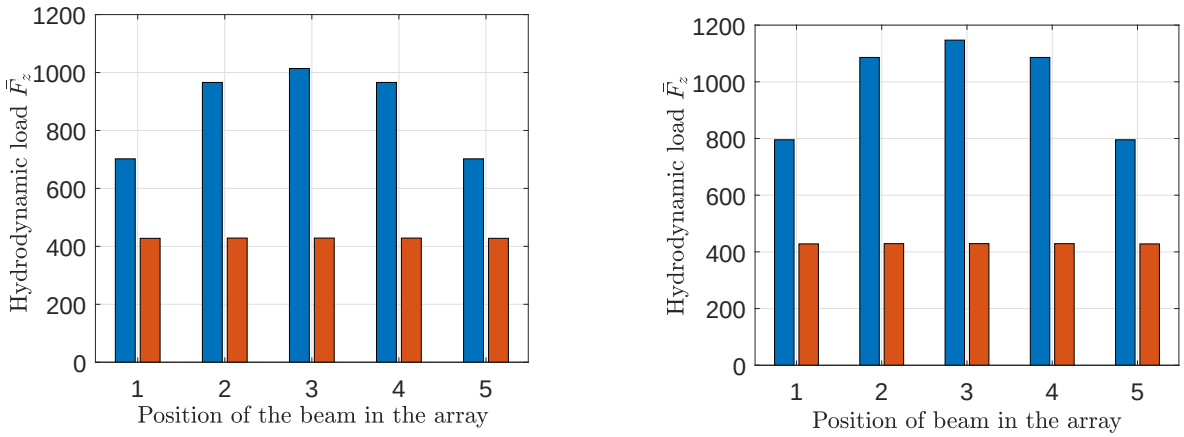

Figure 2.25: Variation of the overall hydrodynamic load over five microbeams for $Re = 100$ in an unbounded fluid domain for two different gap widths $\bar{g} = 0.1$ (blue) and $\bar{g} = 8$ (orange), (a) with nearest neighbours only and (b) with all members incorporated for a 1-1-1-1-1 configuration.

five-beam array compared to it being fairly constant across a three-beam array.

When the beams are far apart ($\bar{g} = 8$), we observe that the hydrodynamic load remains fairly constant across the array and is not dependent on the non-neighbouring members nor the Reynolds number except for the fact that the outer beams have a slightly less load at low Re.

2.7 Discussion and Conclusions

The underlying physics of the hydrodynamic interactions between multiple members in a two-, three- and a five-beam array have been systematically analyzed for active-passive configuration and other cases (1-1-1, 1-1-1-1-1), with and without the incorporation of non-neighbouring members for $Re = \{0.1, 1, 10, 100\}$. Based on the boundary element technique given by Tuck for a thin ribbon oscillating in an infinite fluid domain [57] and the generalized coupling matrix given by Basak et al. [5], we incorporated the additional coupling contributions due to non-neighbouring members to investigate their effects on the added mass and the damping of the whole array. In this chapter we focused only on the influence of the hydrodynamic effects (added mass and damping) due to different gaps and the effects of non-neighbouring members for different Reynolds numbers.

Figures 2.26 and 2.27 compares the imaginary and real parts of pressure evaluated at the midpoints of active beam both in a three- (black) and a five-beam array (red) when only nearest neighbours are incorporated (dashed line) and when all members are incorporated (solid line) to understand the significance of non-neighbouring members on the overall array dynamics.

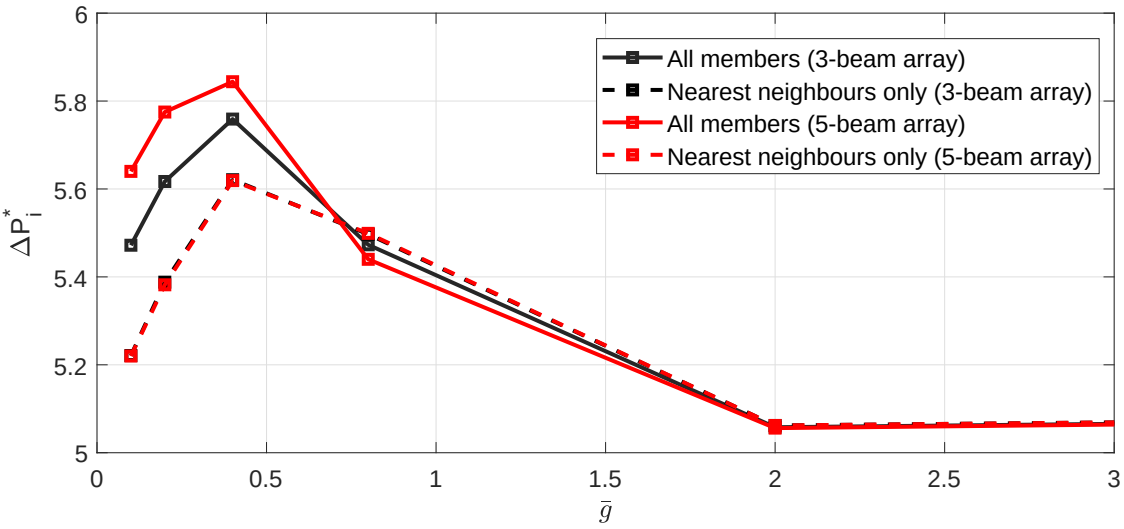

Figure 2.26: Imaginary parts of pressure at the mid point of active beam in a three- (solid line) and a five-beam (dashed line) array for different gaps with only nearest neighbours (black) and all members incorporated (red) at $Re = 1$ for a 1-0-0 and 1-0-0-0-0 configurations.

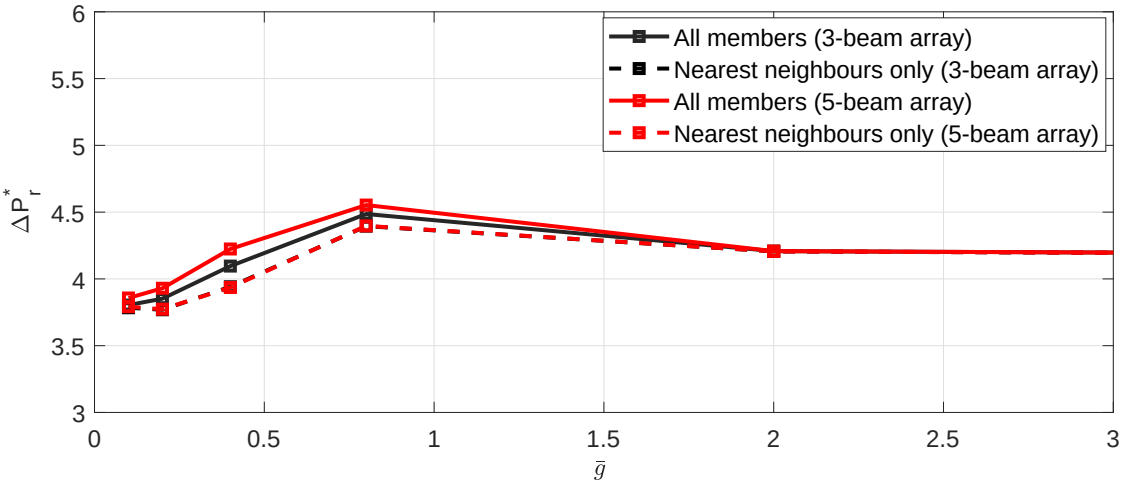

Figure 2.27: Real parts of pressure at the mid point of active beam in a three- (solid line) and a five-beam (dashed line) array for different gaps with only nearest neighbours (black) and all members incorporated (red) at $Re = 1$ for a 1-0-0 and 1-0-0-0-0 configurations.

The trend for added mass and damping remains the same in both arrays (three- and a five-beam array) when only nearest neighbours are incorporated with the black dashed line overlapping the red dashed line. Also, both added mass and damping increase as the beams are brought close to each other and then decrease with decreasing gaps with the critical gaps being $\bar{g} = 0.4$ for added mass and $\bar{g} = 0.8$ for damping.

There is no significant impact of non-neighbouring members in both a three- and a five-beam array when the beams are far apart i.e. for larger gap widths $\bar{g} > 2$, suggesting that they can be neglected for such cases as can be seen in Figures 2.26 and 2.27. When the beams are closely spaced, the overall hydrodynamic load increases with increase in size of the array. This implies that the effect of non-neighbouring members becomes significant as the array size increases resulting in additional contribution due to global array effects. For the damping, we observe a similar trend in which the non-neighbouring members do not influence the behaviour for gaps $\bar{g} > 2$. But for $\bar{g} < 2$ damping effects increase with the incorporation of all members with it being more significant for a five-beam array compared to a three-beam array, see Figure 2.27.

Hence, both added mass and damping effects are significantly impacted by the global array dynamics especially for increasing members in array. A key conclusion is that non-neighbouring members play a significant role as the size of the array increases and cannot be ignored for arrays having more than three members. Non-neighbouring members strongly impact the added mass and damping for $\bar{g} < 2$ and in particular, the effect is enhanced for $\bar{g} < 0.4$ implying that they cannot be ignored.

We also found that the position of the active beam in the array and the number of beams on either side of it does affect the coupling. Hence, the overall dynamics and the coupling effects seen are position dependent. The magnitude of added mass and damping at the critical gaps shifts in the case of both beams actuated (1-1) compared to one beam being active and the other passive (1-0) in a two-beam configuration. The 1-0 effect has to be incorporated in addition to the 1-1 effect when considering the overall hydrodynamic effects and coupling.

A conservative measure is that large arrays can be treated as a series of individual oscillators given the gap between each oscillator is sufficiently large i.e. $\bar{g} > 8$. However when the oscillators are in close proximity to each other i.e. $\bar{g} < 2$, additional effects are observed due to the significance of non-neighbouring members implying that array effects dominate the overall dynamics. The non-neighbouring members are insignificant for higher Re irrespective of the gap width between the beams due to the localized effects but for lower Re one cannot neglect the effects of non-neighbouring members due to overlapping boundary layers or global effects.

Chapter 3

Arrays in close proximity to a surface

In this chapter we develop a mathematical model for beams vibrating in close proximity to a rigid surface. The beams are considered mechanically decoupled and only fluid coupling effects are considered. The model is derived applying the boundary integral method [57] explained in Chapter 2 for an array of beams vibrating in an infinite fluid domain.

3.1 Hydrodynamic coupling of two beams in close proximity to a surface

Two long slender beams immersed in an incompressible viscous fluid vibrating in close proximity to a surface are shown in Figure 3.1. We define the Cartesian coordinate system x, y, z and its corresponding vector basis $\mathbf{E_x}, \mathbf{E_y}, \mathbf{E_z}$. The axis of the beam lies along the x-direction $\mathbf{E_x}$, the transverse motion is described along $\mathbf{E_z}$ and lateral motion along $\mathbf{E_y}$, respectively. While Raman has provided a mathematical model of multiple beams vibrating in an infinite fluid domain [5] and Sader has provided a model for a single beam vibrating in close proximity to a surface [21], our formulation is for two beams in close proximity to a surface and extend the same to an array of beams. We thus incorporate an array of beams in an unbounded fluid medium (Raman's model) and near wall effects (Sader's model) to study array dynamics for both far- and near-field cases. Based on this, we derive the hydrodynamic coupling matrices for the hydrodynamically coupled beams in close proximity to a surface and extend it to present results for a three- and a five-beam array later in this chapter.

In this case of two beams the contour required for the boundary integral technique is shown in Figure 3.1. Each hatched region in fact represents an infinitesimally thin region corresponding to one beam cross section. We assume that the beam vibrates in its fundamental mode only. Hence, the three dimensional phenomena ($3D$) relating to variation of the flow physics along the axis of the beam can be ignored. The gap between the beams is $2g$, whereas the beams are each $2b$ wide. Each cross section of a beam oscillates in the $y - z$ plane. Moreover, since the lower and upper

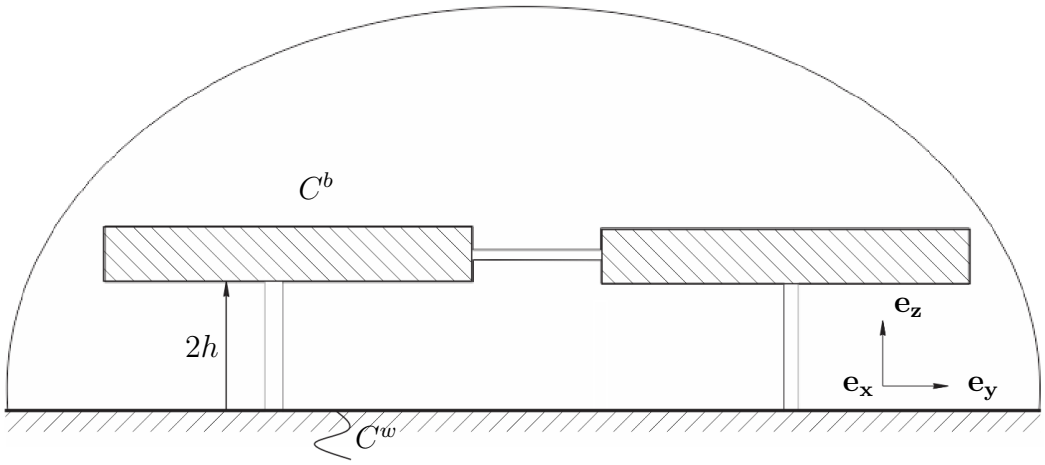

Figure 3.1: Sketch of the boundary value problem for two infinitely thin beams near a surface. The contours $\mathcal{C}^b$ and $\mathcal{C}^w$ denote the cross-sections of the beam and the wall respectively (anti-clockwise positive). The origin of the coordinate system is fixed on the wall with $\mathbf{e_x}, \mathbf{e_y}$ and $\mathbf{e_z}$ denoting the unit vectors in the respective directions.

curves (C^{b-} and C^{b+}) for each beam are infinitesimally close, we assume that there is no relative motion between the top and bottom faces of each beam resulting in ψ and ψ_n being continuous across each beam cross section, where n denotes differentiation normal to the boundary of the fluid $\mathcal{C}$.

Application of boundary integral method results in the following integral representation of the streamfunction for the unsteady Stokes equations. For further details of the derivation of the streamfunction and application of boundary integral method the reader is referred to [21].

$$\begin{aligned}\psi(y,z|\omega) = &\int_{-\infty}^{\infty}\left(\zeta^w(y',0|\omega)\Psi_{z'}(y,z|y',0) - \frac{1}{\mu}P^w(y',0|\omega)\Psi_{y'}(y,z|y',0)\right)dy' \\ &+\int_{-(2b+g)}^{-g}\left(\Delta\zeta_1(y',2h|\omega)\Psi_{z'}(y,z|y',2h) - \frac{1}{\mu}\Delta P_1(y',2h|\omega)\Psi_{y'}(y,z|y',2h)\right)dy' \\ &+\int_{g}^{(2b+g)}\left(\Delta\zeta_2(y',2h|\omega)\Psi_{z'}(y,z|y',2h) - \frac{1}{\mu}\Delta P_2(y',2h|\omega)\Psi_{y'}(y,z|y',2h)\right)dy'\end{aligned} \tag{3.1}$$

where limits of beam 1 (left) is defined from $-(2b+g)$ to $-g$, limits of beam 2 (right) is defined from g to $(2b+g)$, $\Delta\zeta_i$ and Δp_i are the differences in vorticity and pressure across the beam, i.e. $\Delta P = P^{b+} - P^{b-}$, where P^{b+} and P^{b-} are the pressures on the top and bottom face of the beam, respectively and the subscript $i \in 1, 2$ denotes the corresponding beam under consideration. Note that the pressure and vorticities are nondimensionalized.

Differentiating (3.1) with respect to z and y to obtain the velocity components v and w (the reader is referred to (2.3) in Chapter 2), and evaluating each integral at either the wall ($z = 0$) or the zero thickness beam ($z = 2h$), we obtain the following

coupled integral equations, lateral and vertical velocities of the wall (2 equations) and the lateral and vertical velocities at the beams (2 x 2(beams) = 4 equations), totalling to six coupled integral equations:

WALL:

$$v(y,0|\omega) = \int_{-\infty}^{\infty} \left(\zeta^w(y',0|\omega)\Psi_{z'z}(y,0|y',0) - \frac{1}{\mu}P^w(y',0|\omega)\Psi_{y'z}(y,0|y',0) \right) dy' + \int_{-(2b+g)}^{-g} \left(\Delta\zeta_1(y',2h|\omega)\Psi_{z'z}(y,0|y',2h) - \frac{1}{\mu}\Delta P_1(y',2h|\omega)\Psi_{y'z}(y,0|y',2h) \right) dy' + \int_{g}^{(2b+g)} \left(\Delta\zeta_2(y',2h|\omega)\Psi_{z'z}(y,0|y',2h) - \frac{1}{\mu}\Delta P_2(y',2h|\omega)\Psi_{y'z}(y,0|y',2h) \right) dy' \tag{3.2a}$$

$$w(y,0|\omega) = -\int_{-\infty}^{\infty} \left(\zeta^w(y',0|\omega)\Psi_{z'y}(y,0|y',0) - \frac{1}{\mu}P^w(y',0|\omega)\Psi_{y'y}(y,0|y',0) \right) dy' - \int_{-(2b+g)}^{-g} \left(\Delta\zeta_1(y',2h|\omega)\Psi_{z'y}(y,0|y',2h) - \frac{1}{\mu}\Delta P_1(y',2h|\omega)\Psi_{y'y}(y,0|y',2h) \right) dy' - \int_{g}^{(2b+g)} \left(\Delta\zeta_2(y',2h|\omega)\Psi_{z'y}(y,0|y',2h) - \frac{1}{\mu}\Delta P_2(y',2h|\omega)\Psi_{y'y}(y,0|y',2h) \right) dy' \tag{3.2b}$$

BEAMS:

$$v(y,2h|\omega) = \int_{-\infty}^{\infty} \left(\zeta^w(y',0|\omega)\Psi_{z'z}(y,2h|y',0) - \frac{1}{\mu}P^w(y',0|\omega)\Psi_{y'z}(y,2h|y',0) \right) dy' + \int_{-(2b+g)}^{-g} \left(\Delta\zeta_1(y',2h|\omega)\Psi_{z'z}(y,2h|y',2h) - \frac{1}{\mu}\Delta P_1(y',2h|\omega)\Psi_{y'z}(y,2h|y',2h) \right) dy' + \int_{g}^{(2b+g)} \left(\Delta\zeta_2(y',2h|\omega)\Psi_{z'z}(y,2h|y',2h) - \frac{1}{\mu}\Delta P_2(y',2h|\omega)\Psi_{y'z}(y,2h|y',2h) \right) dy' \tag{3.2c}$$

$$w(y,2h|\omega) = -\int_{-\infty}^{\infty} \left(\zeta^w(y',0|\omega)\Psi_{z'y}(y,2h|y',0) - \frac{1}{\mu}P^w(y',0|\omega)\Psi_{y'y}(y,2h|y',0) \right) dy' - \int_{-(2b+g)}^{-g} \left(\Delta\zeta_1(y',2h|\omega)\Psi_{z'y}(y,2h|y',2h) - \frac{1}{\mu}\Delta P_1(y',2h|\omega)\Psi_{y'y}(y,2h|y',2h) \right) dy' - \int_{g}^{(2b+g)} \left(\Delta\zeta_2(y',2h|\omega)\Psi_{z'y}(y,2h|y',2h) - \frac{1}{\mu}\Delta P_2(y',2h|\omega)\Psi_{y'y}(y,2h|y',2h) \right) dy' \tag{3.2d}$$

where $v(y,0|\omega)$ and $w(y,0|\omega)$ are the velocity components of the fluid at the wall in the y and z directions, respectively, and $v(y,2h|\omega)$ and $w(y,2h|\omega)$ are the corresponding velocity components of the fluid at the surface of the beams. Note that the

following derivatives of Green's function $\Psi_{y'z}(y,0|y',0)$, $\Psi_{y'z}(y,2h|y',2h)$,$\Psi_{z'y}(y,0|y',0)$ and $\Psi_{z'y}(y,2h|y',2h)$ equal zero by definition of Ψ [57].

Here we are primarily concerned with the beams undergoing pure normal motion only (i.e. motion in z direction only). Hence, $v(y,0|\omega)=0$, $w(y,0|\omega)=0$, $v(y,2h|\omega)=0$, $w(y,2h|\omega)=W(y|\omega)$, where $W(y|\omega)$ is the velocity of the beam in the z direction. We define velocities of beams 1 and 2 as $W_1(y)=\hat{W}_1 e^{i\omega t}$ and $W_2(y)=\hat{W}_2 e^{(i\omega t+\theta)}$ respectively where $\hat{W}_1$ and $\hat{W}_2$ are velocity amplitudes and θ is the relative phase between the two beams. We also define the following nondimensional parameters and variables: $\xi=y/b$, $\eta=z/b$, gap $\bar{g}=g/b$, height $\bar{h}=h/b$, amplitude ratio $r=\hat{W}_2/\hat{W}_1$, Reynolds number $Re=\rho\omega b^2/\mu$, where ρ is the density of the fluid, ω is the frequency of vibration and μ is the dynamic viscosity of the fluid . For transverse vibrations of the beams in an active-passive (1-0) configuration, the expressions for the transverse and lateral components are given as follows:

Transverse components

$$1=-\int_{-\infty}^{\infty}\left(\zeta^w(\xi',0|\omega)\Psi_{\eta'\xi}(\xi,\bar{h}|\xi',0)-P^w(\xi',0|\omega)\Psi_{\xi'\xi}(\xi,\bar{h}|\xi',0)\right)d\xi'$$
$$+\int_{-(2+\bar{g})}^{-\bar{g}}\Delta P_1(\xi',\bar{h})(\xi',\bar{h}|\omega)\Psi_{\xi'\xi}(\xi,\bar{h}|\xi',\bar{h})d\xi'+\int_{\bar{g}}^{(2+\bar{g})}\Delta P_2(\xi',\bar{h}|\omega)\Psi_{\xi'\xi}(\xi,\bar{h}|\xi',\bar{h})d\xi',$$
$$\xi'\in(-(2+\bar{g}),-\bar{g}),\quad (3.3a)$$

$$0=-\int_{-\infty}^{\infty}\left(\zeta^w(\xi',0|\omega)\Psi_{\eta'\xi}(\xi,\bar{h}|\xi',0)-P^w(\xi',0|\omega)\Psi_{\xi'\xi}(\xi,\bar{h}|\xi',0)\right)d\xi'$$
$$+\int_{-(2+\bar{g})}^{-\bar{g}}\Delta P_1(\xi',\bar{h})(\xi',\bar{h}|\omega)\Psi_{\xi'\xi}(\xi,\bar{h}|\xi',\bar{h})d\xi'+\int_{\bar{g}}^{(2+\bar{g})}\Delta P_2(\xi',\bar{h}|\omega)\Psi_{\xi'\xi}(\xi,\bar{h}|\xi',\bar{h})d\xi',$$
$$\xi'\in(\bar{g},2+\bar{g}),\quad (3.3b)$$

Lateral components

$$0=\int_{-\infty}^{\infty}\left(\zeta^w(\xi',0|\omega)\Psi_{\eta'\eta}(\xi,\bar{h}|\xi',0)-\frac{1}{\mu}P^w(\xi',0|\omega)\Psi_{\xi'\eta}(\xi,\bar{h}|\xi',0)\right)d\xi'$$
$$+\int_{-(2+\bar{g})}^{-\bar{g}}\Delta\zeta_1(\xi',\bar{h}|\omega)\Psi_{\eta'\eta}(\xi,\bar{h}|\xi',\bar{h})d\xi'+\int_{\bar{g}}^{(b+\bar{g})}\Delta\zeta_2(\xi',\bar{h}|\omega)\Psi_{\eta'\eta}(\xi,\bar{h}|\xi',\bar{h})d\xi',$$
$$\xi'\in(-(2+\bar{g}),-\bar{g}),\quad (3.3c)$$

$$0=\int_{-\infty}^{\infty}\left(\zeta^w(\xi',0|\omega)\Psi_{\eta'\eta}(\xi,\bar{h}|\xi',0)-\frac{1}{\mu}P^w(\xi',0|\omega)\Psi_{\xi'\eta}(\xi,\bar{h}|\xi',0)\right)d\xi'$$
$$+\int_{-(2+\bar{g})}^{-\bar{g}}\Delta\zeta_1(\xi',\bar{h}|\omega)\Psi_{\eta'\eta}(\xi,\bar{h}|\xi',\bar{h})d\xi'+\int_{\bar{g}}^{(b+\bar{g})}\Delta\zeta_2(\xi',\bar{h}|\omega)\Psi_{\eta'\eta}(\xi,\bar{h}|\xi',\bar{h})d\xi',$$
$$\xi'\in(\bar{g},2+\bar{g}),\quad (3.3d)$$

In what follows we describe the numerical procedure used to evaluate the six unknowns, namely, P^w, ζ^w, ΔP_1, $\Delta\zeta_1$, ΔP_2 and $\Delta\zeta_2$ which are pressures and vorticities at the wall and at beams 1 and 2, respectively. From the above equations we note that the transverse and lateral motion of the beams are described by two separate, uncoupled equations. Because the transverse motion is of greatest interest in typical AFM applications, our focus will be on the transverse motion which results in pressure jumps across the two beams. This involves transforming the system of integral equations by replacing the integrals with their Riemann sums [5] which results in a corresponding system of matrix-vector equations. The matrix system can then be solved by discretizing the integrals over the width of the wall and each beam into an equal number of segments N. Two singularities are typically identified in the problem [57]: (i) logarithmic singularity at $\xi = \xi'$ which is taken care of by forcing these equations to hold at the middle point of each segment, for instance, at the k^{th} segment, $\xi_k = \frac{1}{2}(\xi'_k + \xi'_{k+1})$, where $k = 0, 1, ..., N-1$ and (ii) square root singularity towards the edges of the beam is avoided by dividing the beam into an unequal number of segments N as follows $(j = 0, 1, ..., N)$:

$$\xi'_j = -1 - \bar{g} - \cos\left(\frac{\pi j}{N}\right), \qquad \xi' \in [-(2+\bar{g}), -\bar{g}], \tag{3.4a}$$

$$\xi'_j = 1 + \bar{g} - \cos\left(\frac{\pi j}{N}\right), \qquad \xi' \in (\bar{g}, 2+\bar{g}), \tag{3.4b}$$

Similarly, we assume that pressure and vorticity do not vary rapidly on the wall and approximate them to be constant over the segment like in the case of the beams. An unequal quadrature is used with the same number of segments N for the integral along the wall which now extends from $-L^w$ to L^w, where L^w is a positive constant far greater than unity.

The equivalent general matrix-vector equation is given as follows:

$$\begin{bmatrix} A_{ww} & B_{ww} & A_{w1} & A_{w2} & B_{w1} & B_{w2} \\ B_{ww} & C_{ww} & B_{w1} & B_{w2} & C_{w1} & C_{w2} \\ A_{1w} & B_{1w} & A_{11} & A_{12} & B_{11} & B_{12} \\ A_{2w} & B_{2w} & A_{21} & A_{22} & B_{21} & B_{22} \\ B_{1w} & C_{1w} & B_{11} & B_{12} & C_{11} & C_{12} \\ B_{2w} & C_{2w} & B_{21} & B_{22} & C_{21} & C_{22} \end{bmatrix} \begin{bmatrix} \zeta^w \\ P^w \\ \Delta\zeta_1 \\ \Delta\zeta_2 \\ \Delta P_1 \\ \Delta P_2 \end{bmatrix} = \begin{bmatrix} 0 \\ 0 \\ 0 \\ 0 \\ W_1 \\ W_2 \end{bmatrix}$$

The first two rows represent the coefficients of wall associated with the lateral and transverse velocities, respectively in which the subscripts ww represents the influence of the segments of the wall on the segments of the wall itself, and $w1$ represents the influence of the segments of beam 1 on the wall, and $w2$ finally, represents the influence of the segments of beam 2 on the wall. The next two rows represent the lateral velocities of beams 1 and 2 with the submatrices in red representing the vorticity coupling matrix implying that lateral velocities result in vorticity coupling only. The last two rows represent the transverse velocities of beams 1 and 2 with

the submatrices in blue representing the pressure coupling matrix implying that the transverse velocities contribute to pressure coupling only. As per our subscript naming convention, 12 represents the influence of the segments of beam 2 on the segments of beam 1 and likewise, 21 represents the influence of the segments of beam 2 on beam 1.

Applying the above assumptions and discretization method, the system of integral equations reduces to the following system of matrix-vector equations for an active beam 1 ($W_1 = 1$) and passive beam 2 ($W_2 = 0$):

$$\begin{bmatrix} A_1 & 0 & A_{2_{11}} & A_{2_{22}} & -A_{3_{11}} & -A_{3_{22}} \\ 0 & B_1 & -A_{3_{11}} & -A_{3_{22}} & B_{3_{11}} & B_{3_{22}} \\ C_1 & -C_2 & C_{3_{11}} & C_{3_{12}} & 0 & 0 \\ C_1 & -C_2 & C_{3_{21}} & C_{3_{22}} & 0 & 0 \\ -C_2 & D_2 & 0 & 0 & D_{3_{11}} & D_{3_{12}} \\ -C_2 & D_2 & 0 & 0 & D_{3_{21}} & D_{3_{22}} \end{bmatrix} \begin{bmatrix} \zeta^w \\ P^w \\ \Delta\zeta_1 \\ \Delta\zeta_2 \\ \Delta P_1 \\ \Delta P_2 \end{bmatrix} = \begin{bmatrix} 0 \\ 0 \\ 0 \\ 0 \\ 1 \\ 0 \end{bmatrix}$$

from which the unknown pressures and vorticities (i.e. $\boldsymbol{P}$ matrix) can be obtained by inverting the coupling matrix and multiplying it with the velocity vector:

$$[\boldsymbol{P}] = [\hat{\boldsymbol{G}}]^{-1} [\boldsymbol{V}] \tag{3.5}$$

where the partitioned coupling matrix $\hat{\boldsymbol{G}}_{\boldsymbol{II}}$ is given by:

$$\hat{\boldsymbol{G}}_{\boldsymbol{II}} = \begin{bmatrix} \mathbf{G}_{11} & \mathbf{G}_{12} & \mathbf{G}_{13} \\ \mathbf{G}_{21} & \mathbf{G}_{22} & \mathbf{G}_{23} \\ \mathbf{G}_{31} & \mathbf{G}_{32} & \mathbf{G}_{33} \end{bmatrix}$$

The details of the coupling matrix are given in Appendix A while the corresponding elements of the matrices are defined in Appendix B.

3.2 Results

Here we present results with effect of all members incorporated since it was found in Chapter 2 that non-neighbouring member effects cannot be ignored. Nondimensional parameters that influence the coupled hydrodynamics are the gaps $\bar{g}$, the heights from the surface $\bar{h}$ (see Figure 3.1), the amplitude ratio r between beams, the relative phase θ between beam 1 (left-most) and other members, the unsteady Reynolds number Re and the non-neighbouring members, see Chapter 2. Based on the analysis and insights of Chapter 2 here we consider the contributions of all members in the array. The effect of gaps between beams in an array and the effects of height on a single beam have been studied previously by Basak et al. [5] and Sader et al. [21], respectively. Our focus is laid on performing a parametric analysis on a combination of different gaps $\bar{g} = \{8, 0.4, 0.1\}$ and heights $\bar{h} = \{10, 1, 0.3\}$ to study and analyze the coupling influences on the overall array dynamics. Here, we present results for an active-passive configuration in a two-, three- and a five-beam array. Unlike in Chapter 2, where multiple configurations are considered with the position of the actuated beam being shifted in the array, here we consider only the leftmost

beam to be active while the rest are passive. We do not expect to see any additional interactive coupling effects stemming from shifting the position of the active beam in the array in addition to the effects already seen in Chapter 2 with the array in an infinite fluid domain. Also, we perform only a qualitative study and emphasis is placed only on the magnitudes and not on the phases.

We present numerical results for the hydrodynamic loading (absolute value of pressure), its inertial component (imaginary part of pressure) and its dissipative component (real part of pressure) across both the active and passive beams as they are brought closer to the surface for the above mentioned parameters. The results presented here are studied for three different Reynolds numbers $Re = \{0.1, 1, 100\}$ with the number of discretization elements $N = \mathcal{O}(100)$ for both the beams and the wall chosen based on the height from the surface. An extensive convergence study can be found in Appendix C, where the relationship between various parameters are discussed and it was found that N increases with decreasing $\bar{h}$. The length of the wall scales with respect to the number of beams M as follows $L_w = 15M$ with Gauss-Legendre quadrature nodes $n = 4$ and the active beam vibrating at its maximum amplitude ($\hat{W}_a = 1$). These parameters are chosen keeping in mind the compromise required between accuracy of obtained results and the computational time.

3.2.1 Two-beams with surface effects

In this section we present the absolute, imaginary and real parts of pressure difference across two beams in which the leftmost beam is active (red) and the other is passive (blue). The parameters chosen for the analysis are $Re = \{0.1, 1, 100\}$, nondimensional gaps $\bar{g} = 8$ (solid), $\bar{g} = 0.4$ (dash-dotted) and $\bar{g} = 0.1$ (dotted) and three different heights from the surface: $\bar{h} = 10$ (top panels), $\bar{h} = 1$ (mid panels) and $\bar{h} = 0.3$ (bottom panels). We study and analyze the overall hydrodynamic load and whether added mass or damping dominates the hydrodynamic coupling and the critical gaps and heights at which they dominate for different Reynolds numbers.

Re = 0.1

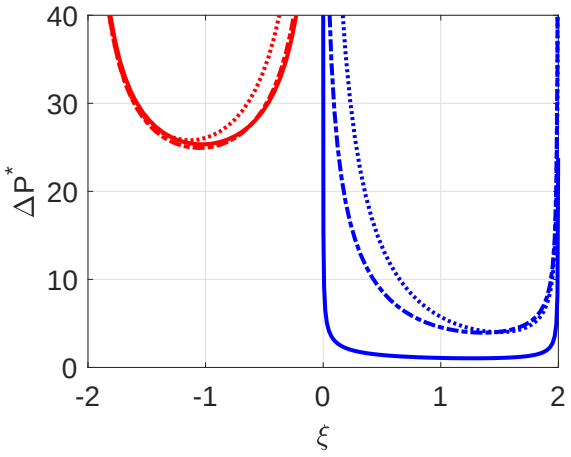

(a)

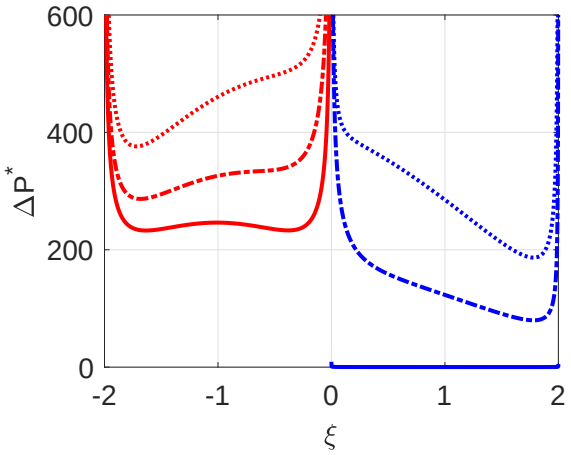

(b)

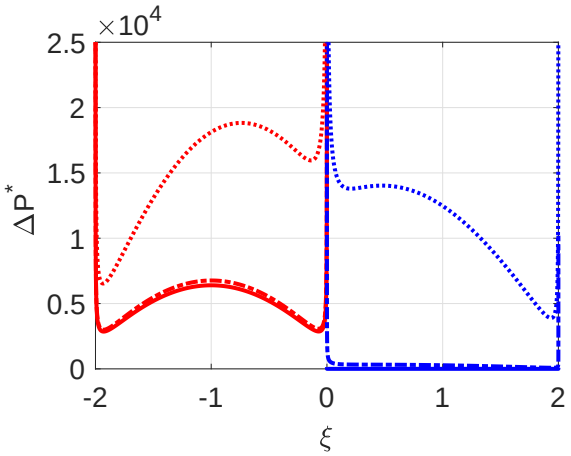

(c)

Figure 3.2: Absolute pressure difference across active (red) and passive (blue) beams at $Re = 0.1$ for heights (a) $\bar{h} = 10$, (b) $\bar{h} = 1$ and (c) $\bar{h} = 0.3$ for $\bar{g} = 8$ (solid), $\bar{g} = 0.4$ (dash-dotted) and $\bar{g} = 0.1$ (dotted).

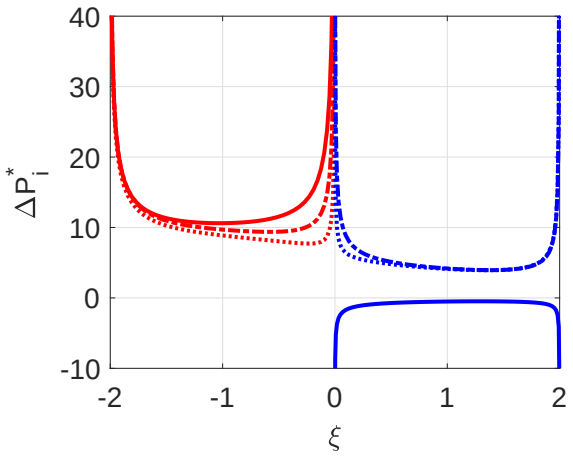

(a)

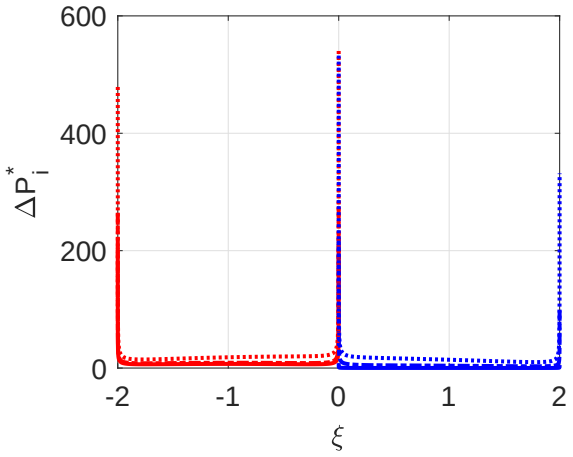

(b)

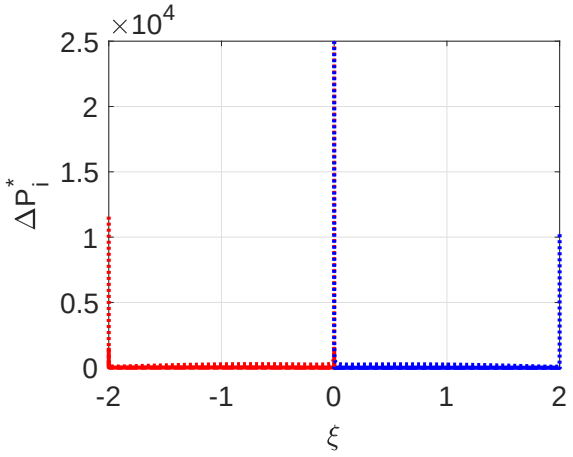

(c)

Figure 3.3: Imaginary part of pressure difference across active (red) and passive (blue) beams at $Re = 0.1$ for heights (a) $\bar{h} = 10$, (b) $\bar{h} = 1$ and (c) $\bar{h} = 0.3$ for $\bar{g} = 8$ (solid), $\bar{g} = 0.4$ (dash-dotted) and $\bar{g} = 0.1$ (dotted).

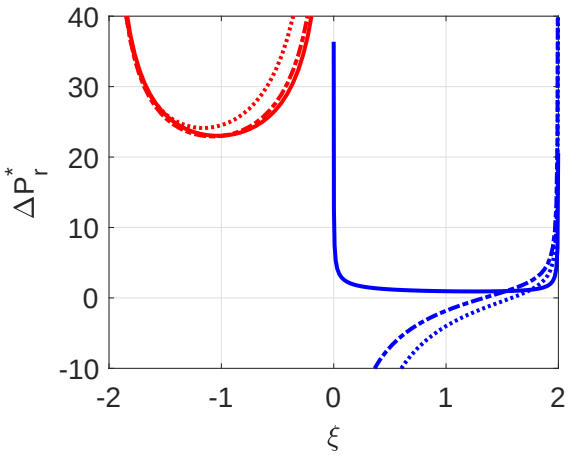

(a)

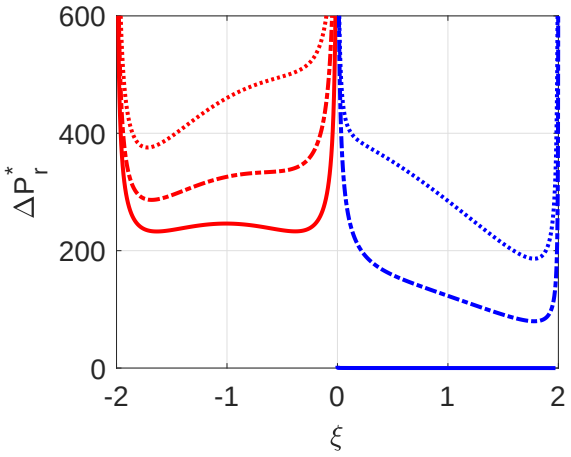

(b)

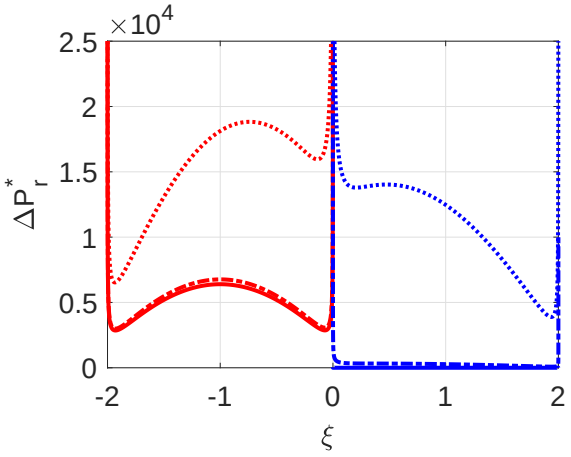

(c)

Figure 3.4: Real part of pressure difference across active (red) and passive (blue) beams at $Re = 0.1$ for heights (a) $\bar{h} = 10$, (b) $\bar{h} = 1$ and (c) $\bar{h} = 0.3$ for $\bar{g} = 8$ (solid), $\bar{g} = 0.4$ (dash-dotted) and $\bar{g} = 0.1$ (dotted).

Overall hydrodynamic load We observe that the overall hydrodynamic load increases by three orders of magnitude as the beams are brought in close proximity to the surface (from $\bar{h} = 10$ to $\bar{h} = 0.3$) as can be seen in Figure 3.2. The pressure profile becomes increasingly distorted and asymmetric for the smallest gap of $\bar{g} = 0.1$ between the beams with it being concave when far away from the surface and convex when in close proximity to the surface.

Coupling between members The coupling is highest for the closest gap i.e. $\bar{g} = 0.1$ between the beams and closest height $\bar{h} = 0.3$ from the surface. The viscous effects (real part) increasingly dominates the added mass effects (imaginary part) with increasing proximity to the surface as can be seen from Figures 3.2 - 3.4. The critical gaps at which the added mass and damping changes, appear to peak at different heights from the surface implying that the added mass and damping are mutually dependent on the gaps between the beams and the heights from which the beams are operated at.

Re = 1

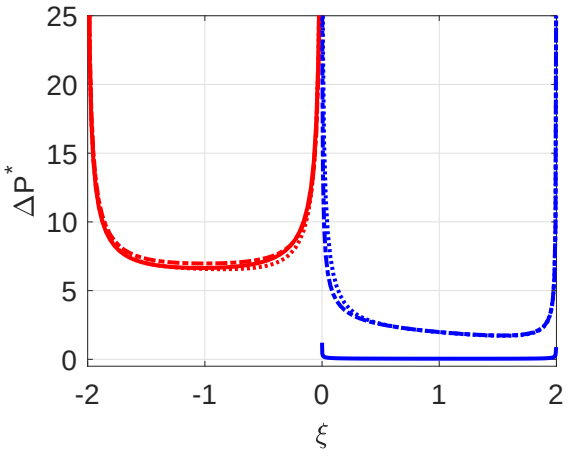

(a)

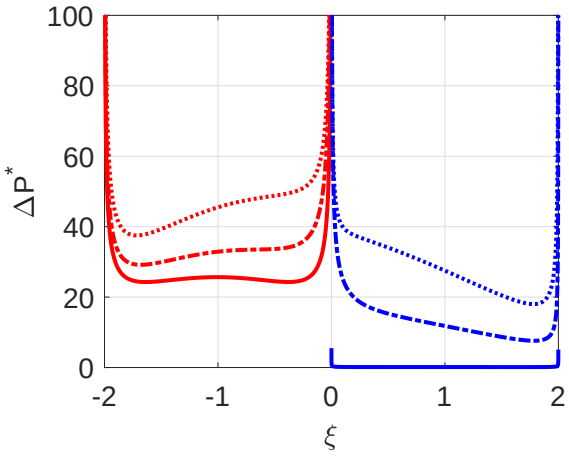

(b)

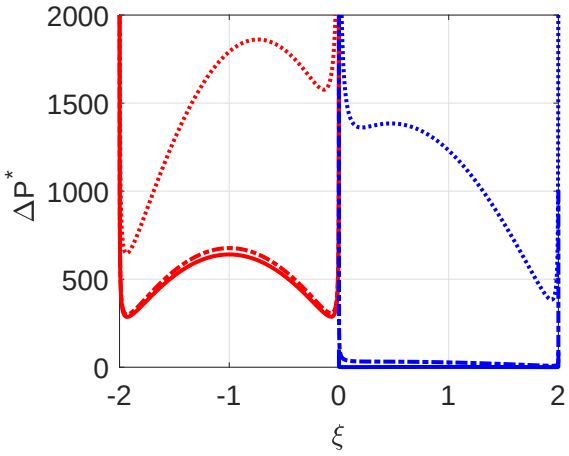

(c)

Figure 3.5: Absolute pressure difference across active (red) and passive (blue) beams at $Re = 1$ for heights (a) $\bar{h} = 10$, (b) $\bar{h} = 1$ and (c) $\bar{h} = 0.3$ for $\bar{g} = 8$ (solid), $\bar{g} = 0.4$ (dash-dotted) and $\bar{g} = 0.1$ (dotted).

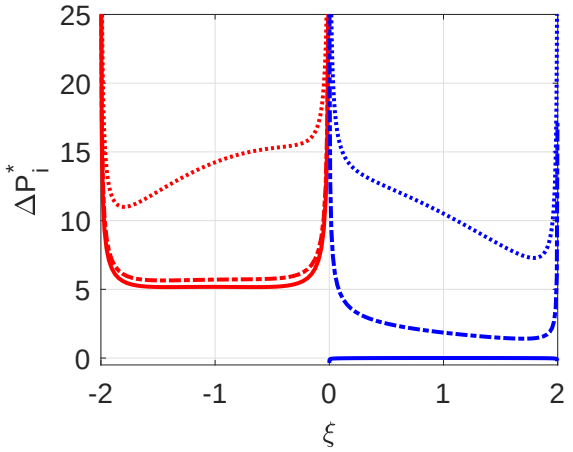

(a)

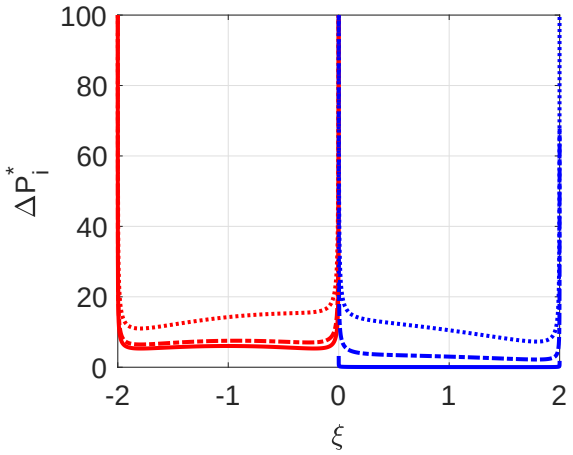

(b)

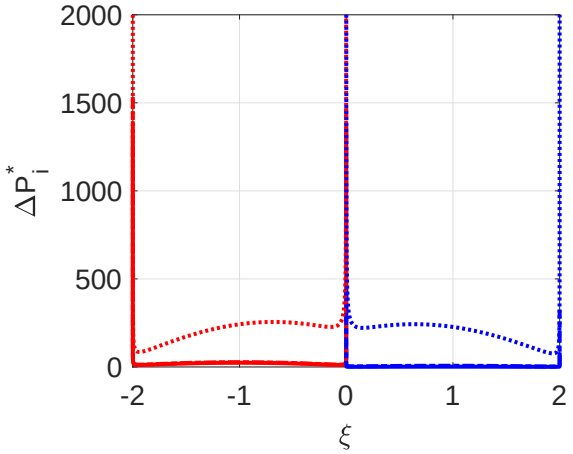

(c)

Figure 3.6: Imaginary part of pressure difference across active (red) and passive (blue) beams at $Re = 1$ for heights (a) $\bar{h} = 10$, (b) $\bar{h} = 1$ and (c) $\bar{h} = 0.3$ for $\bar{g} = 8$ (solid), $\bar{g} = 0.4$ (dash-dotted) and $\bar{g} = 0.1$ (dotted).

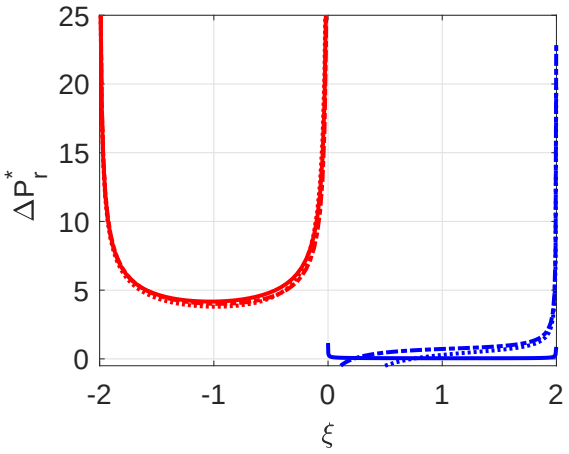

(a)

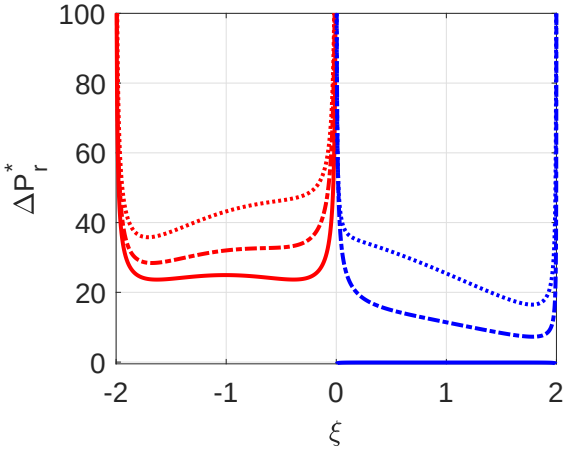

(b)

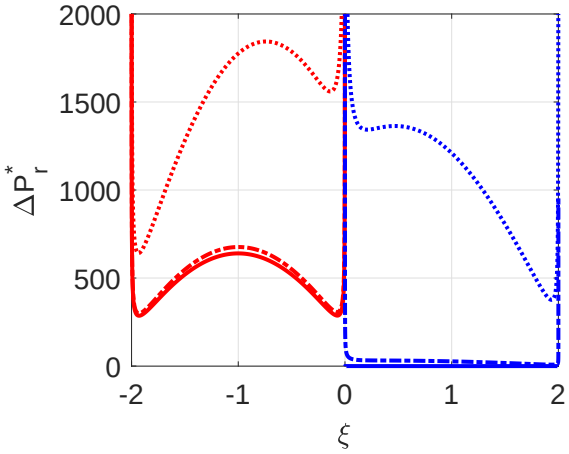

(c)

Figure 3.7: Real part of pressure difference across active (red) and passive (blue) beams at $Re = 1$ for heights (a) $\bar{h} = 10$, (b) $\bar{h} = 1$ and (c) $\bar{h} = 0.3$ for $\bar{g} = 8$ (solid), $\bar{g} = 0.4$ (dash-dotted) and $\bar{g} = 0.1$ (dotted).

Overall hydrodynamic load For $Re = 1$, we observe that the overall hydrodynamic load increases with decreasing heights as in the case of $Re = 0.1$ but with a reduction in magnitude from $\mathcal{O}(10^0)$ to $\mathcal{O}(10^3)$ when compared to the corresponding heights and gaps at $Re = 0.1$ implying that the hydrodynamic load is dependent on Reynolds numbers, gaps and heights.

Coupling between members Also, we note that the added mass effects (see Figures 3.5 - 3.7) dominate the overall behaviour when far away from the surface ($\bar{h} = 10$) whereas as the beams are brought in close proximity to the surface ($\bar{h} = 0.3$), we see that the viscous effects dominate the overall behaviour implying that the dominating mechanism is mutually dependent on both gaps $\bar{g}$, heights $\bar{h}$ and Reynolds numbers.

Re = 100

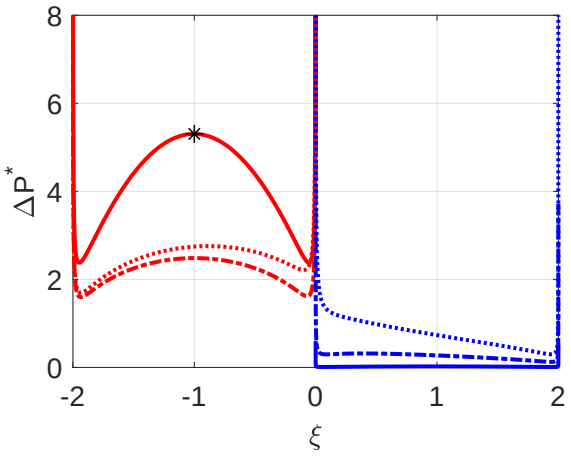

(a)

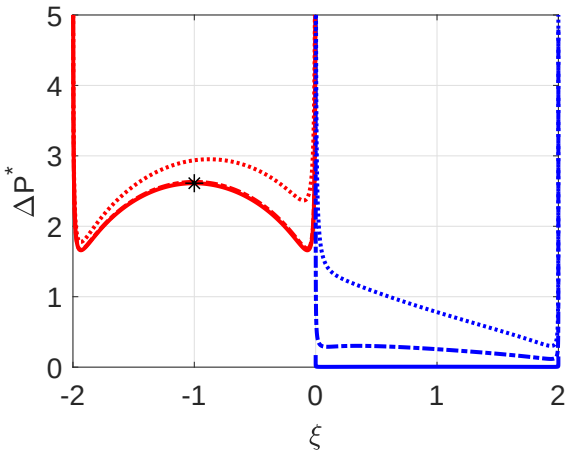

(b)

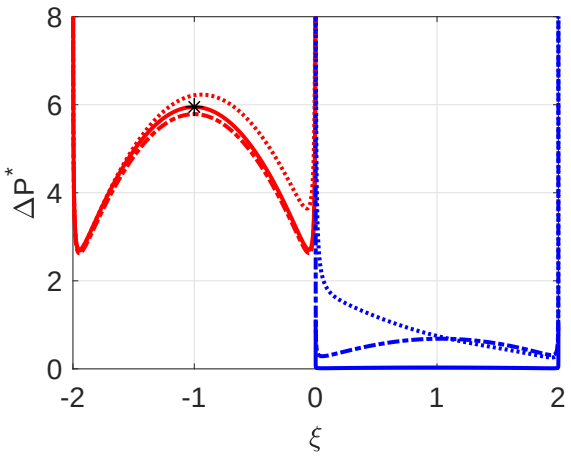

(c)

Figure 3.8: Absolute part of pressure difference across active (red) and passive (blue) beams at $Re = 100$ for heights (a) $\bar{h} = 10$, (b) $\bar{h} = 1$ and (c) $\bar{h} = 0.3$ for $\bar{g} = 8$ (solid), $\bar{g} = 0.4$ (dash-dotted) and $\bar{g} = 0.1$ (dotted).

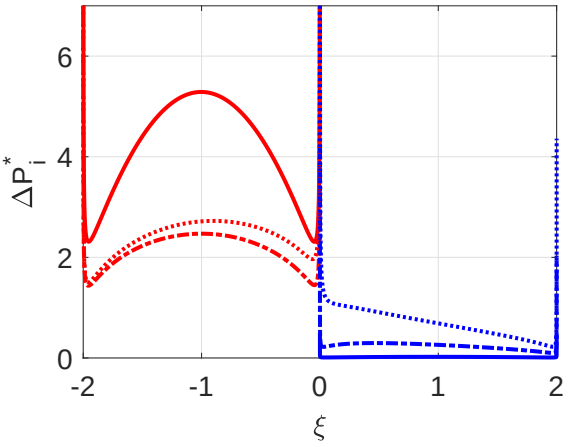

(a)

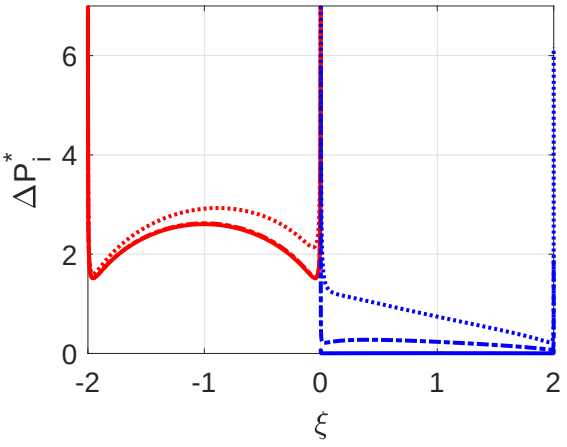

(b)

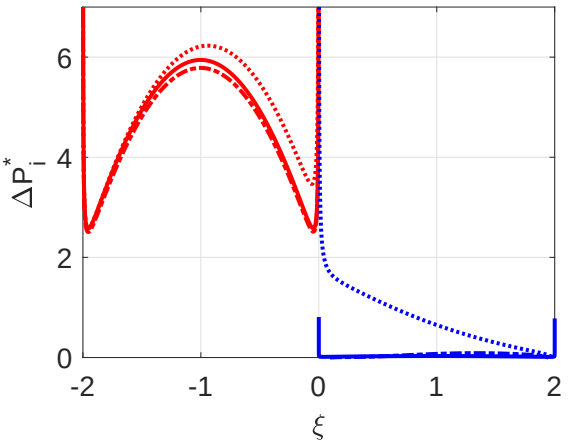

(c)

Figure 3.9: Imaginary part of pressure difference across active (red) and passive (blue) beams at $Re = 100$ for heights (a) $\bar{h} = 10$, (b) $\bar{h} = 1$ and (c) $\bar{h} = 0.3$ for $\bar{g} = 8$ (solid), $\bar{g} = 0.4$ (dash-dotted) and $\bar{g} = 0.1$ (dotted).

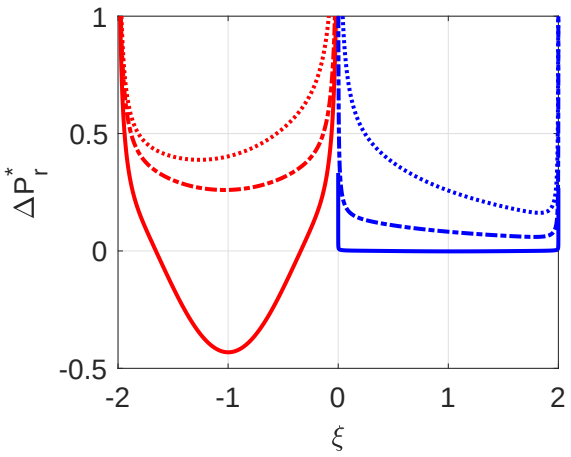

(a)

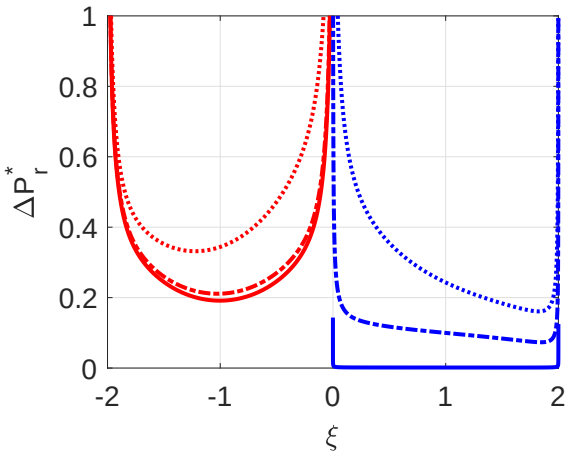

(b)

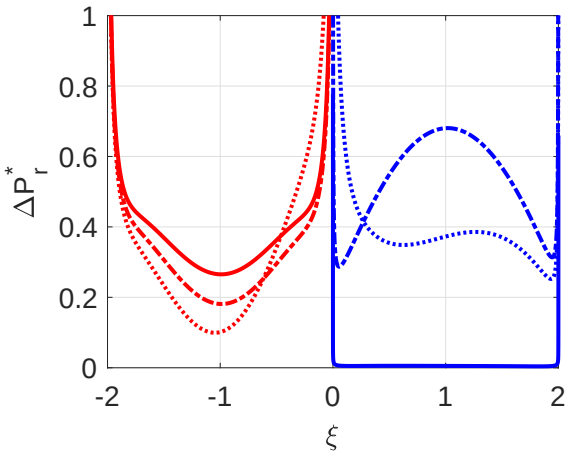

(c)

Figure 3.10: Real part of pressure difference across active (red) and passive (blue) beams at $Re = 100$ for heights (a) $\bar{h} = 10$, (b) $\bar{h} = 1$ and (c) $\bar{h} = 0.3$ for $\bar{g} = 8$ (solid), $\bar{g} = 0.4$ (dash-dotted) and $\bar{g} = 0.1$ (dotted).

Overall hydrodynamic load We observe that the overall hydrodynamic load is significantly reduced in comparison to low Reynolds numbers i.e. $Re = \{0.1, 1\}$, for instance, compare Figures 3.2, 3.5 and 3.8. In this particular case of $Re = 100$, the orders of magnitude with different heights remains constant ($\mathcal{O}(10^0)$), whereas at low Re the orders of magnitude varied with it being $\mathcal{O}(10^0)$ when the beams are far away while it is $\mathcal{O}(10^4)$ when the beams are in close proximity to the surface. This may be explained by the fact that with increasing Reynolds numbers the boundary layers shrink and hence, are more localized resulting in lower overall hydrodynamic load. Also, the load initially decreases with decreasing heights i.e. $\bar{h} = 10$ to $\bar{h} = 1$ but it starts to increase again as it is brought further closer to the surface i.e. $\bar{h} = 0.3$ implying that the hydrodynamic load has a non-monotonic behavior with decreasing heights for $Re = 100$, see markers in Figure 3.8.

Coupling between members Also, added mass is the dominating factor irrespective of the heights at $Re = 100$ unlike the low Re cases, in which the viscous effects dominated the overall dynamics with increasing proximity to the surface. This can again be attributed to the rather thin boundary layers resulting in diminishing viscosity between the beams implying that only added mass dominates the overall behaviour.

3.2.2 Three-beam array with surface effects

In this section, we perform a similar study (overall hydrodynamic load and coupling effects) in the case of a three-beam array with surface effects included as was the case with the two-beam configuration. The leftmost beam is the active beam (red) while beam 2 (blue) and beam 3 (black) are passive.

Re = 0.1

Overall hydrodynamic load We observe that the overall hydrodynamic load increases by four orders of magnitude ($\mathcal{O}(10^1)$ to $\mathcal{O}(10^5)$) with decreasing heights, see Figure 3.11 but is not necessarily the highest at the smallest gap (i.e. $\bar{g} = 0.1$) as can be seen in Figure 3.11c. Also, as observed in a two-beam array configuration, the overall dynamics is dominated by damping in comparison to added mass.

Coupling between members We observe that the real part is negative for $\bar{h} = 0.1$ and $\bar{g} = 0.1$ but we are concerned only with the magnitude in this thesis and leave out any discussions concerning phase. Also, from Figure 3.13c we see that the array modes start to set in implying the significance and effects of additional members in the array. Also, the critical gaps at which the added mass or damping shifts, changes with heights.

Array effects Unlike the two-beam configuration, here we observe distinct mode shapes implying that varying the number of members in the array influences these modes, for instance, see Figure 3.11b in which for the closest gap between the beams ($\bar{g} = 0.1$) the pressure profile across three beams nearly resembles a half-sine wave.

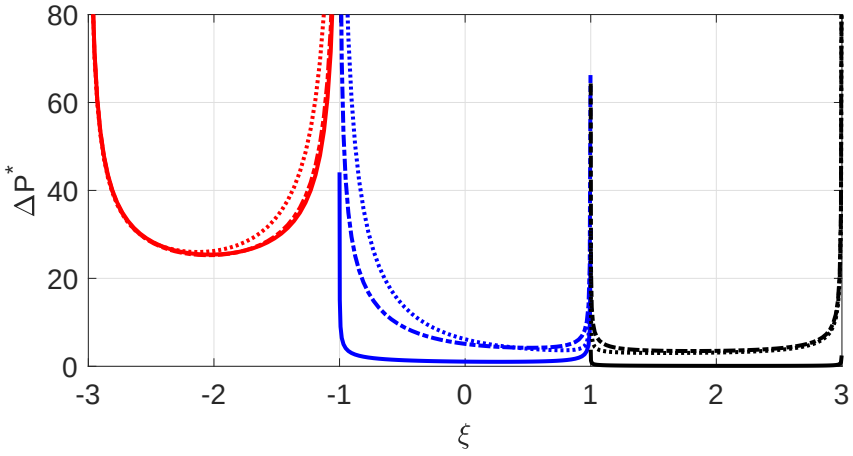

(a)

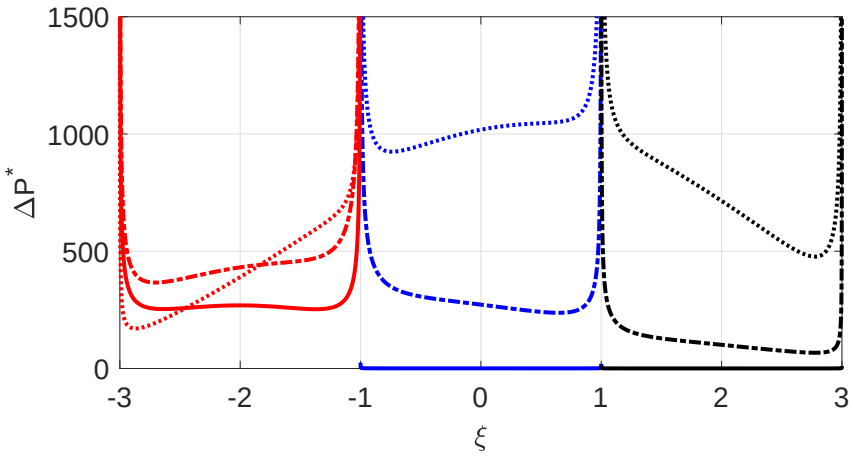

(b)

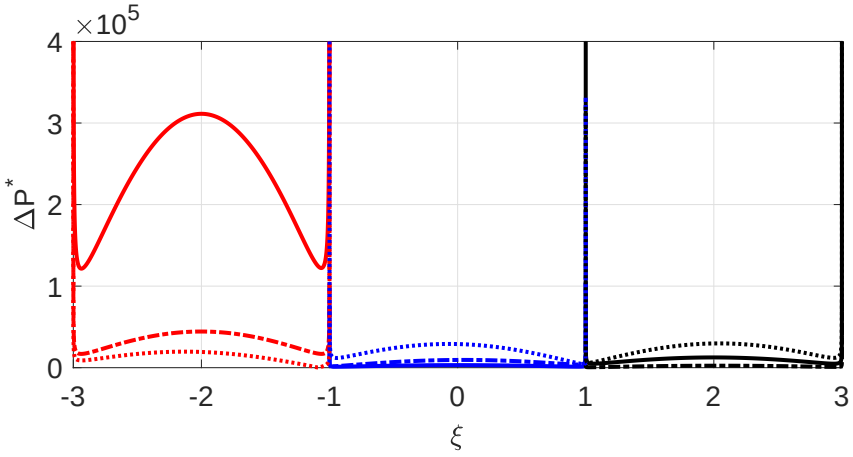

(c)

Figure 3.11: Absolute part of pressure difference across active (left-most) and passive (rest of them) beams at $Re = 0.1$ for heights (a) $\bar{h} = 10$, (b) $\bar{h} = 1$ and (c) $\bar{h} = 0.3$ for $\bar{g} = 8$ (solid), $\bar{g} = 0.4$ (dash-dotted) and $\bar{g} = 0.1$ (dotted).

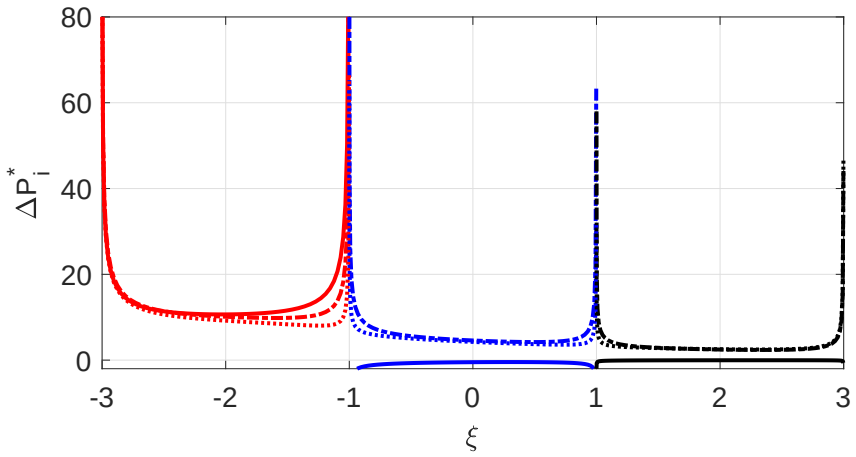

(a)

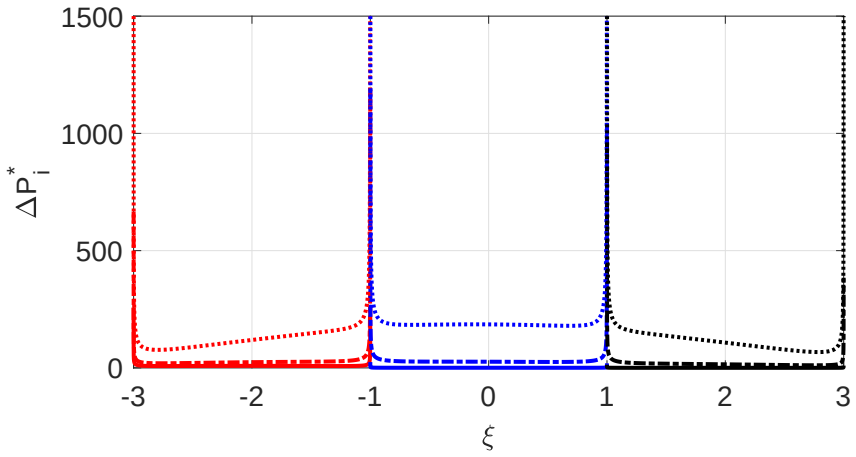

(b)

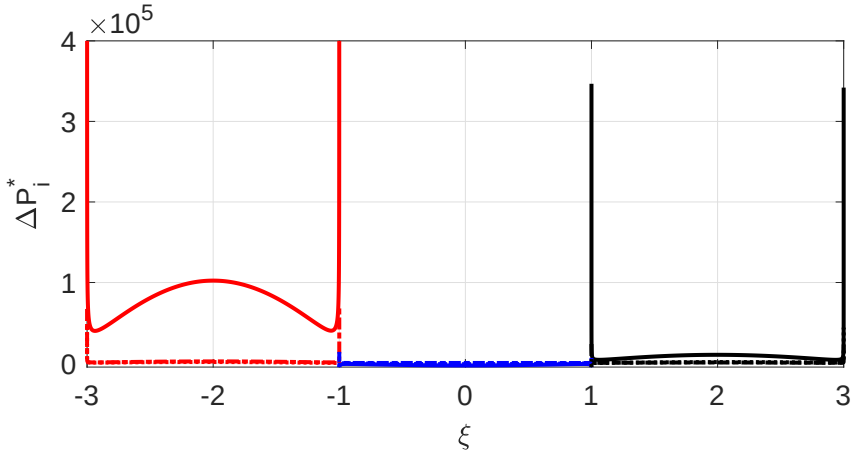

(c)

Figure 3.12: Imaginary part of pressure difference across active (left-most) and passive (rest of them) beams at $Re = 0.1$ for heights (a) $\bar{h} = 10$, (b) $\bar{h} = 1$ and (c) $\bar{h} = 0.3$ for $\bar{g} = 8$ (solid), $\bar{g} = 0.4$ (dash-dotted) and $\bar{g} = 0.1$ (dotted).

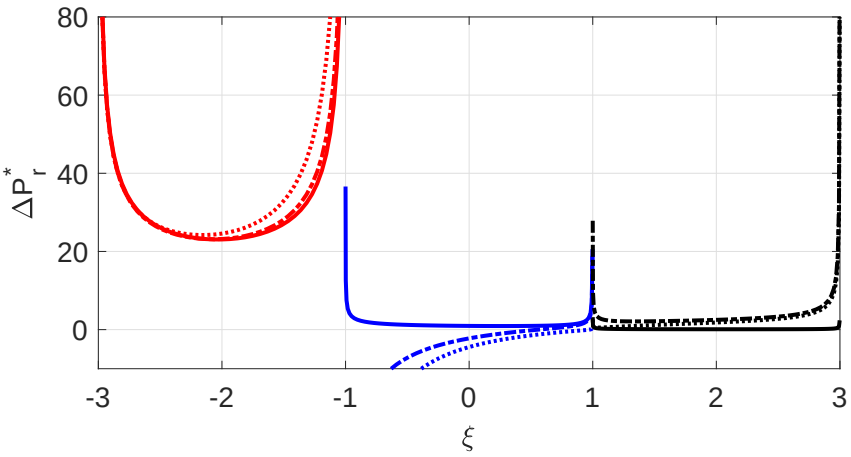

(a)

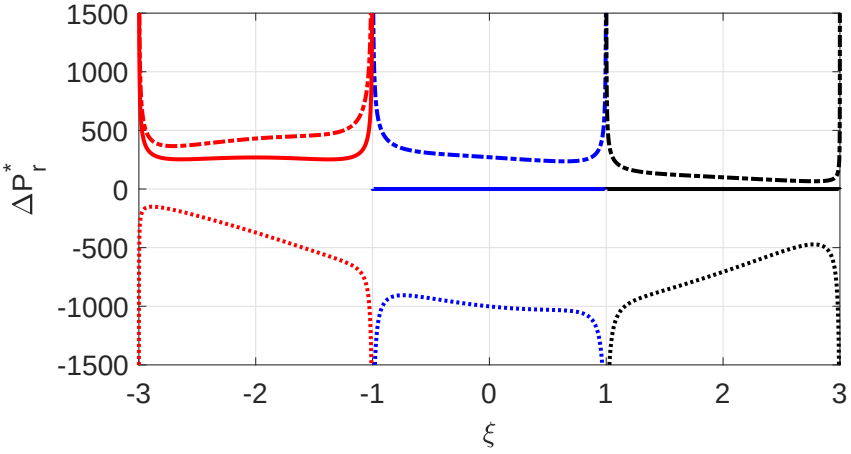

(b)

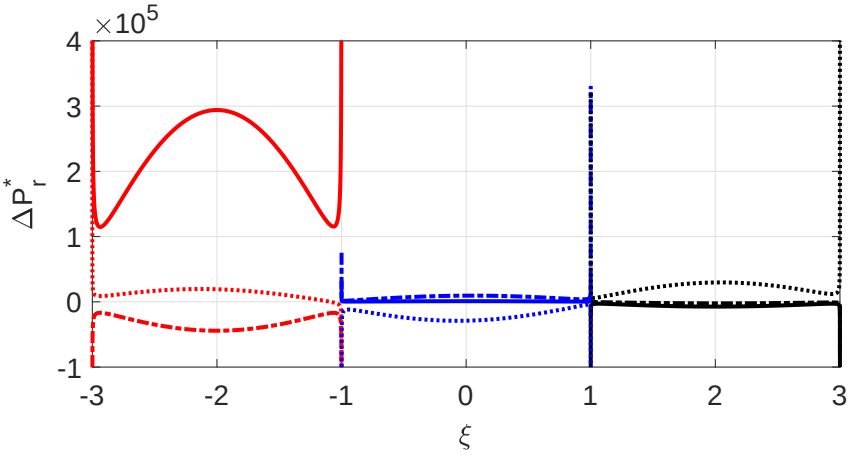

(c)

Figure 3.13: Real part of pressure difference across active (left-most) and passive (rest of them) beams at $Re = 0.1$ for heights (a) $\bar{h} = 10$, (b) $\bar{h} = 1$ and (c) $\bar{h} = 0.3$ for $\bar{g} = 8$ (solid), $\bar{g} = 0.4$ (dash-dotted) and $\bar{g} = 0.1$ (dotted).

Re = 1

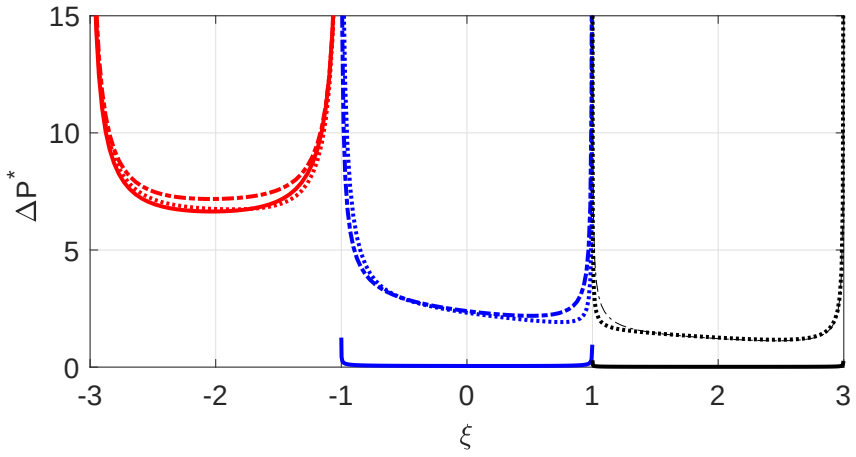

(a)

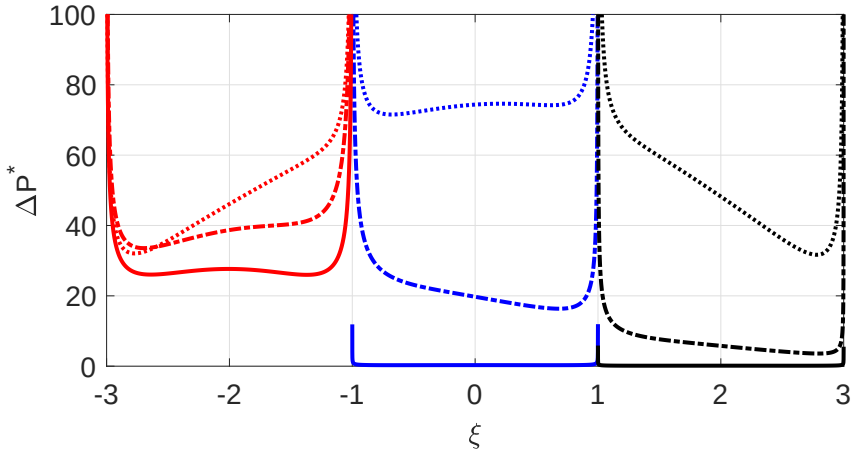

(b)

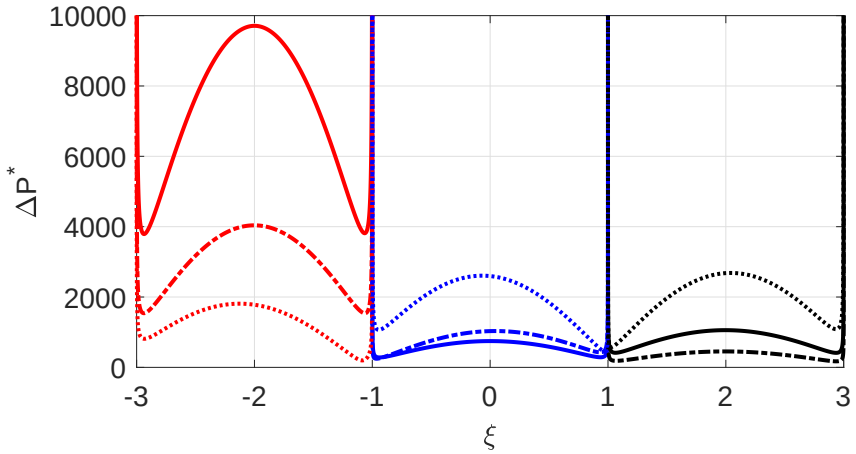

(c)

Figure 3.14: Absolute part of pressure difference across active (left-most) and passive (rest of them) beams at $Re = 1$ for heights (a) $\bar{h} = 10$, (b) $\bar{h} = 1$ and (c) $\bar{h} = 0.3$ for $\bar{g} = 8$ (solid), $\bar{g} = 0.4$ (dash-dotted) and $\bar{g} = 0.1$ (dotted).

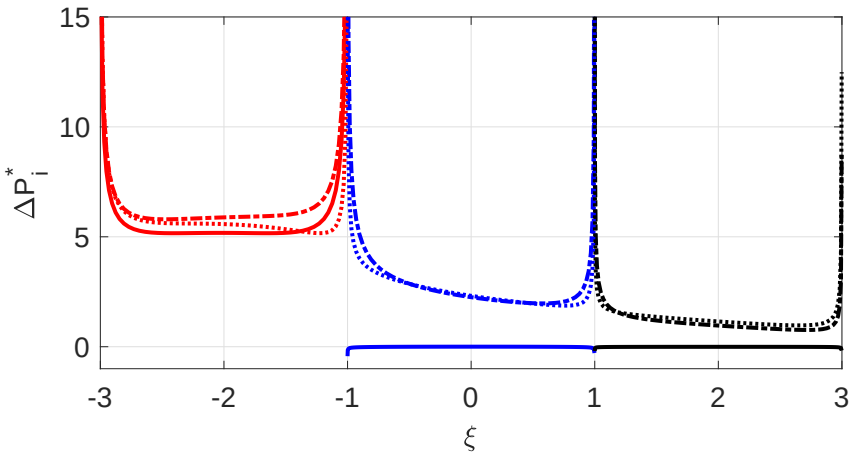

(a)

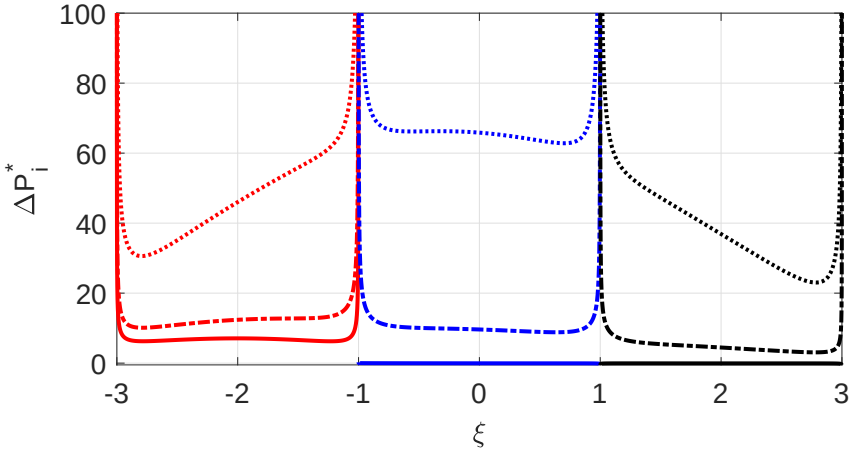

(b)

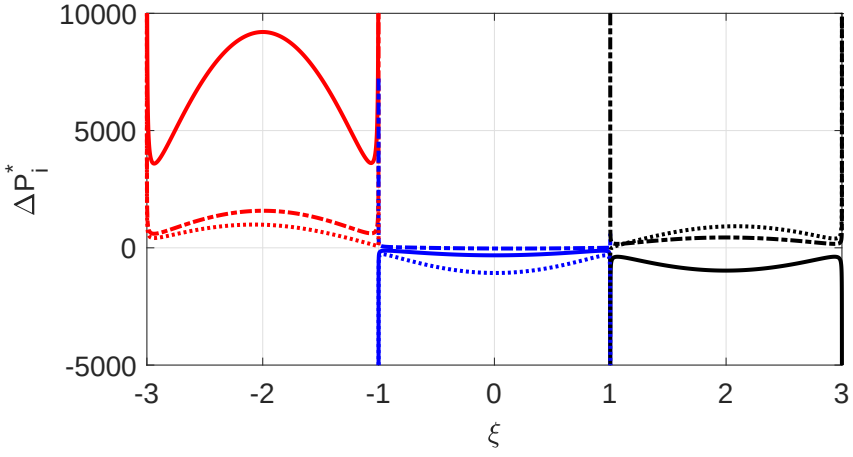

(c)

Figure 3.15: Imaginary part of pressure difference across active (left-most) and passive (rest of them) beams at $Re = 1$ for heights (a) $\bar{h} = 10$, (b) $\bar{h} = 1$ and (c) $\bar{h} = 0.3$ for $\bar{g} = 8$ (solid), $\bar{g} = 0.4$ (dash-dotted) and $\bar{g} = 0.1$ (dotted).

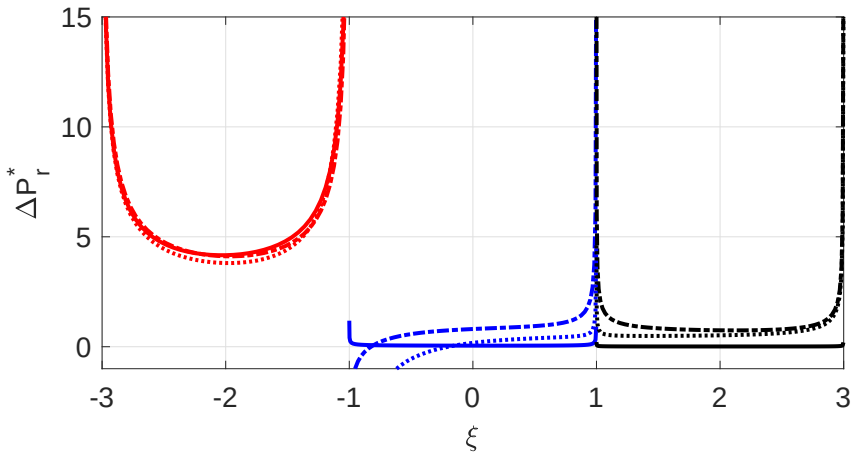

(a)

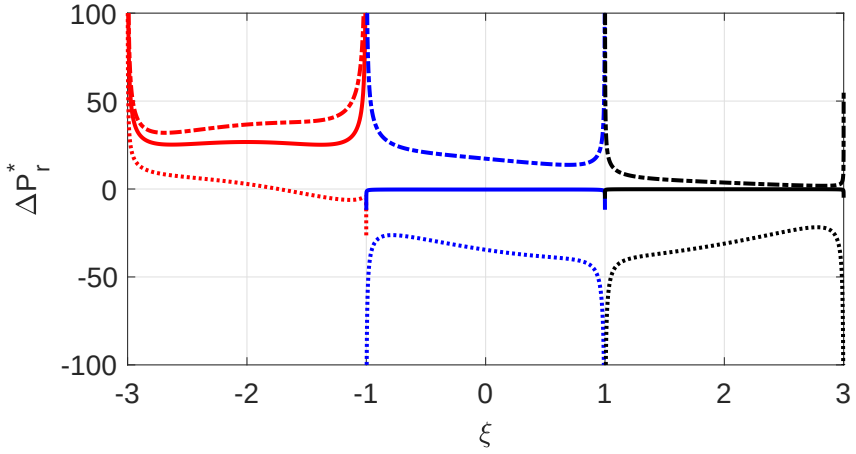

(b)

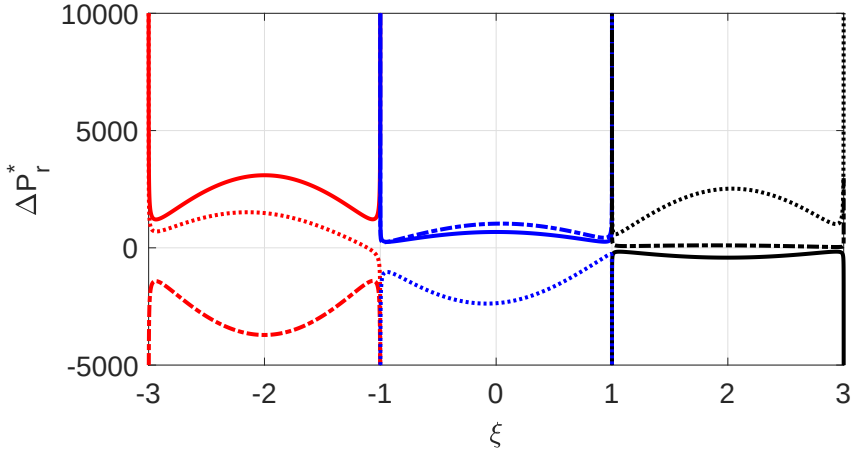

(c)

Figure 3.16: Real part of pressure difference across active (left-most) and passive (rest of them) beams at $Re = 1$ for heights (a) $\bar{h} = 10$, (b) $\bar{h} = 1$ and (c) $\bar{h} = 0.3$ for $\bar{g} = 8$ (solid), $\bar{g} = 0.4$ (dash-dotted) and $\bar{g} = 0.1$ (dotted).

Overall hydrodynamic load The overall hydrodynamic load for the corresponding heights in comparison to $Re = 0.1$ is significantly less. Also, as observed before the pressure profile becomes convex with decreasing heights with the onset of array modes for the closest gaps and heights under consideration.

Array effects With increasing proximity to the surface and decreasing gaps between the beams, we observe an increase in spatial periodicity of the modes with it being nearly a quarter in Figure 3.15a, a half in Figure 3.15b and one-and-a-half in Figure 3.15c.

Re = 100

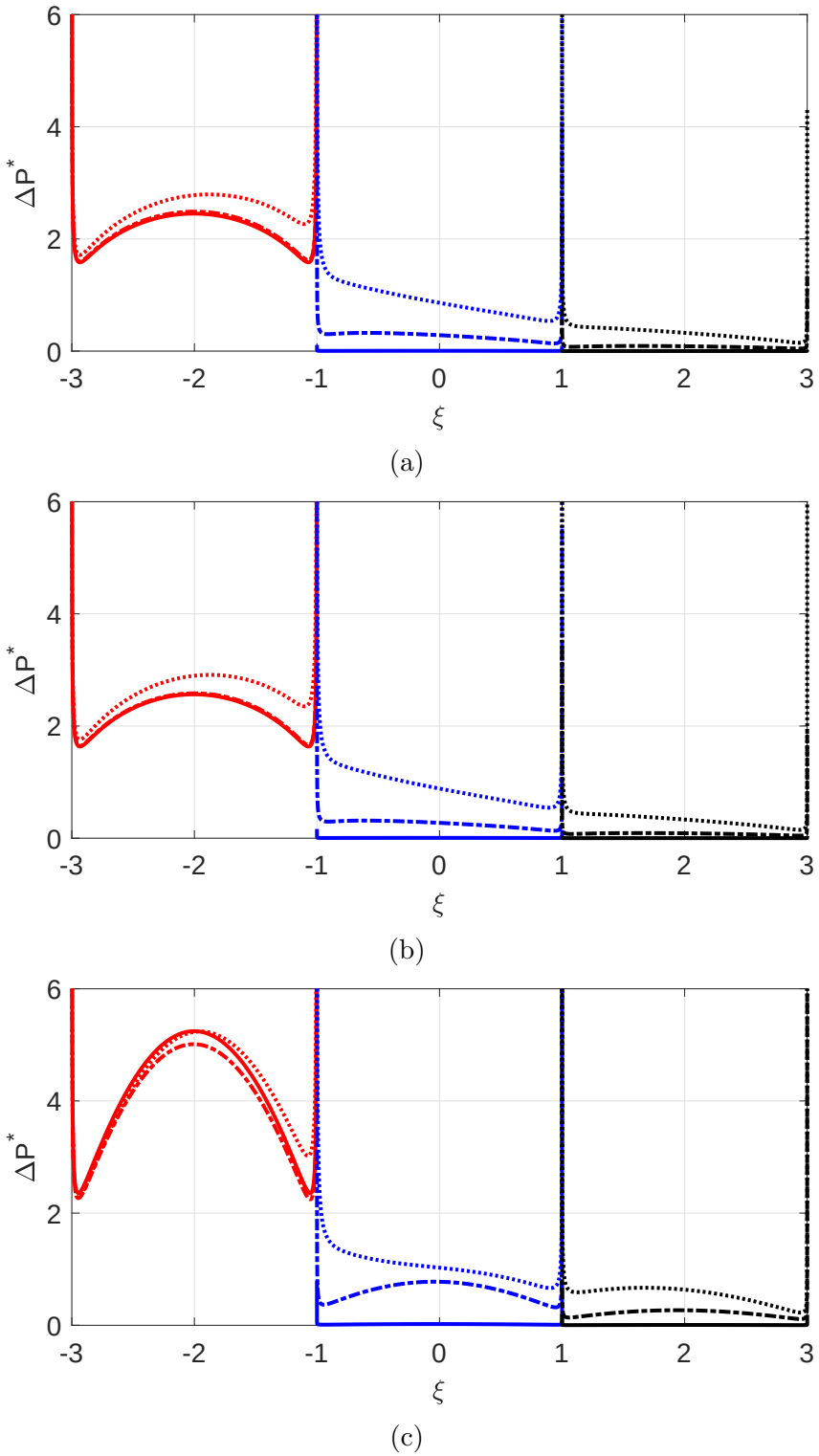

Figure 3.17: Absolute part of pressure difference across active (left-most) and passive (rest of them) beams at $Re = 100$ for heights (a) $\bar{h} = 10$, (b) $\bar{h} = 1$ and (c) $\bar{h} = 0.3$ for $\bar{g} = 8$ (solid), $\bar{g} = 0.4$ (dash-dotted) and $\bar{g} = 0.1$ (dotted).

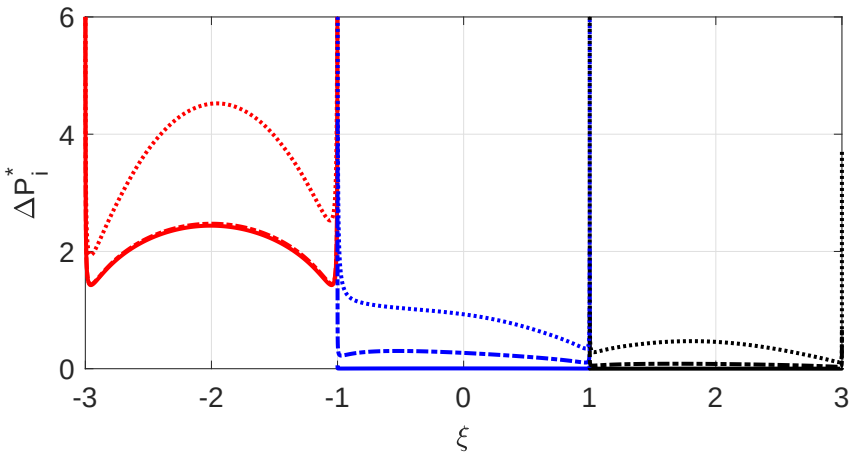

(a)

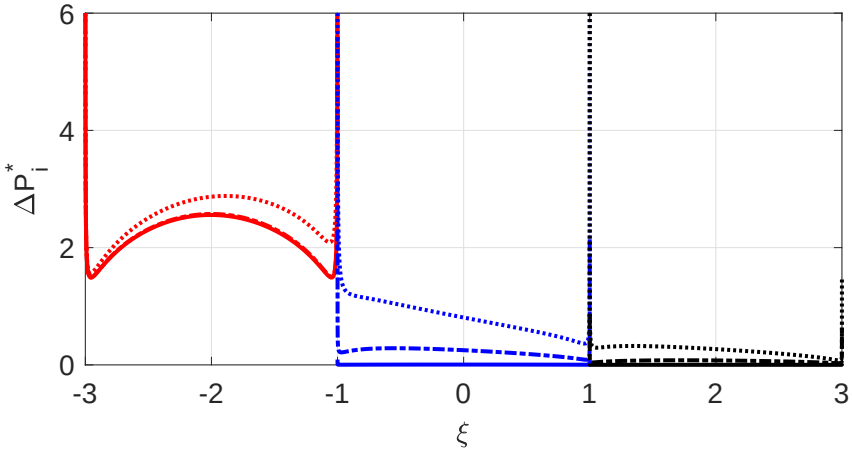

(b)

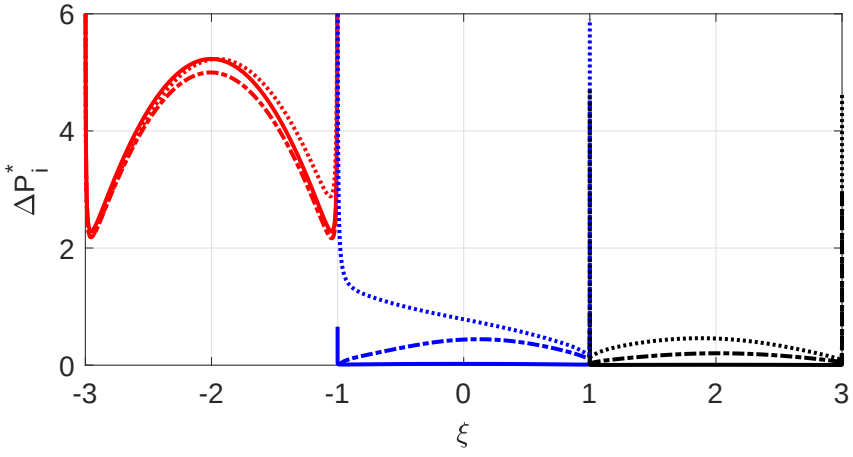

(c)

Figure 3.18: Imaginary part of pressure difference across active (left-most) and passive (rest of them) beams at $Re = 100$ for heights (a) $\bar{h} = 10$, (b) $\bar{h} = 1$ and (c) $\bar{h} = 0.3$ for $\bar{g} = 8$ (solid), $\bar{g} = 0.4$ (dash-dotted) and $\bar{g} = 0.1$ (dotted).

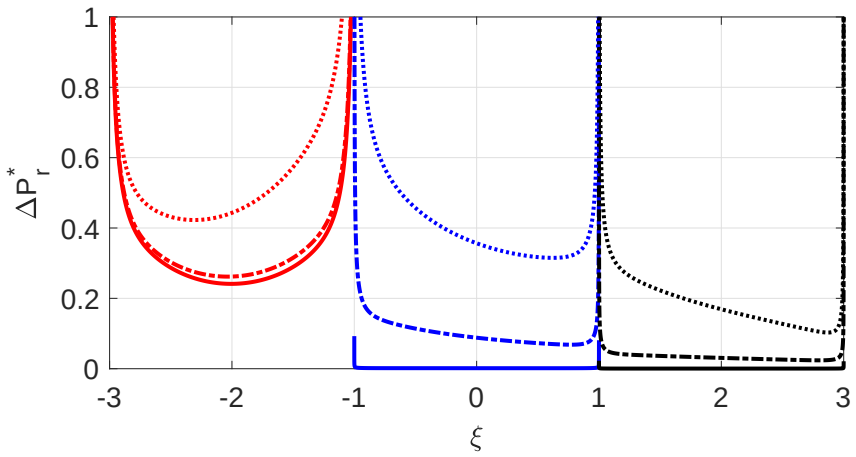

(a)

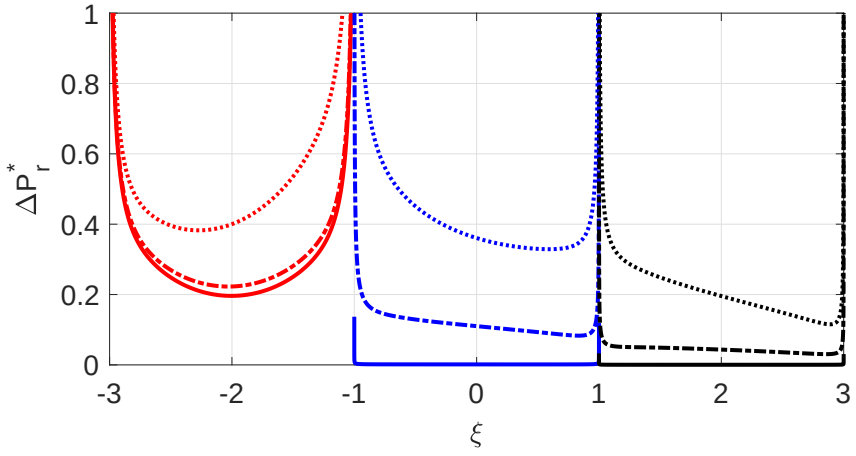

(b)

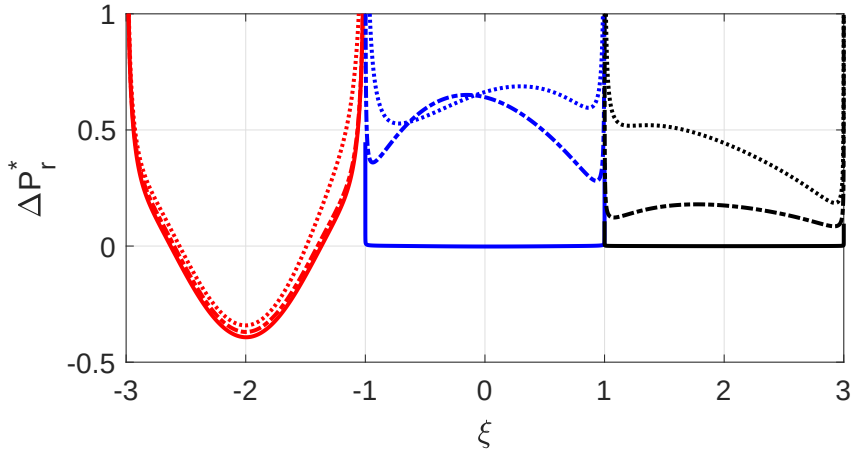

(c)

Figure 3.19: Real part of pressure difference across active (left-most) and passive (rest of them) beams at $Re = 100$ for heights (a) $\bar{h} = 10$, (b) $\bar{h} = 1$ and (c) $\bar{h} = 0.3$ for $\bar{g} = 8$ (solid), $\bar{g} = 0.4$ (dash-dotted) and $\bar{g} = 0.1$ (dotted).

Overall hydrodynamic load The overall hydrodynamic load is significantly less than $Re = 0.1$ and $Re = 1$. Here we note that the pressure profile is convex irrespective of the height.

Coupling between members Also, added mass is the dominating effect and we do not see a significant shift in critical gaps with decreasing heights implying that at high Re, heights dominate the overall coupling in comparison to gaps between the beams.

Array effects Unlike the low Re cases, we do not see any increase in spatial peridicity of the mode shapes with increasing proximity to the surface and decreasing gaps between the beams implying that at high Re, local effects are predominant.

3.2.3 Five-beam array with surface effects

In this section, we extend the length of the array to five members to study and analyze the overall hydrodynamic loading (absolute), added mass (imaginary) and damping (real) for a range of Reynolds numbers, gaps and heights as done previously. Also, having observed the increasing spatial periodicty of mode shapes with increasing proximity to the surface, we expect to see a similar trend in a five-beam array with surface effects included. The leftmost beam is the active (red) beam while the rest are passive.

Re = 0.1

Overall hydrodynamic load The overall hydrodynamic load increases with decreasing heights as was the case with two beams and a three-beam array.

Coupling between members The viscous part dominates the overall dynamics in comparison to the added mass effects.

Array effects The array modes set in when the beams are brought close to each other and increasing proximity to the surface, see Figure 3.22, in which the spatial periodicity of the mode shapes increase with the pressure profiles for the closest gap between the members ($\bar{g} = 0.1$) crossing the nodal line (zero line) five times for the smallest height from the surface ($\bar{h} = 0.1$) in comparison to it crossing the nodal line only once for $\bar{h} = 1$.

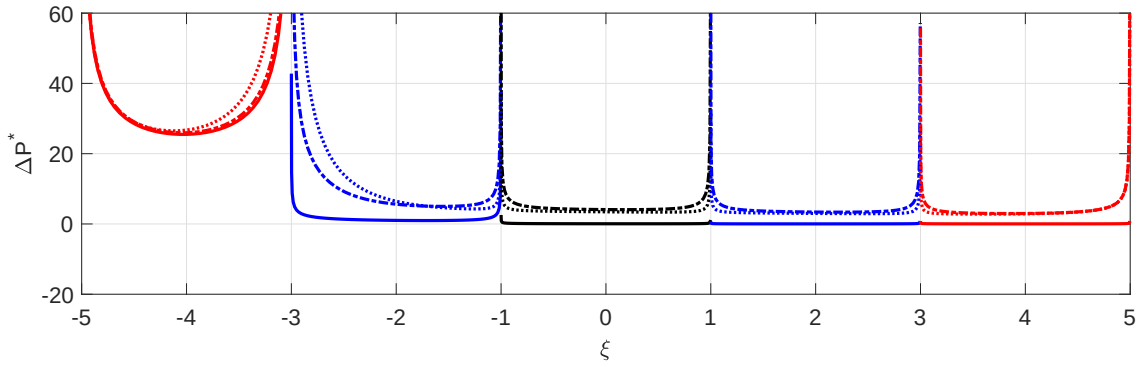

(a)

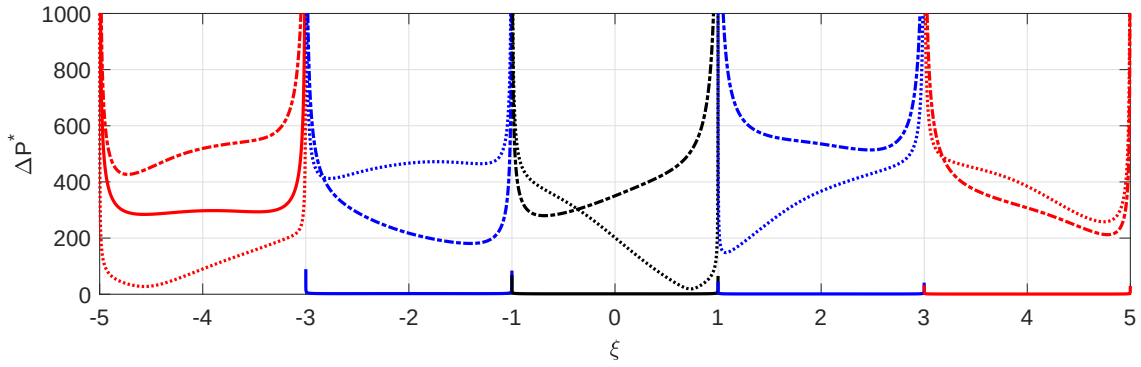

(b)

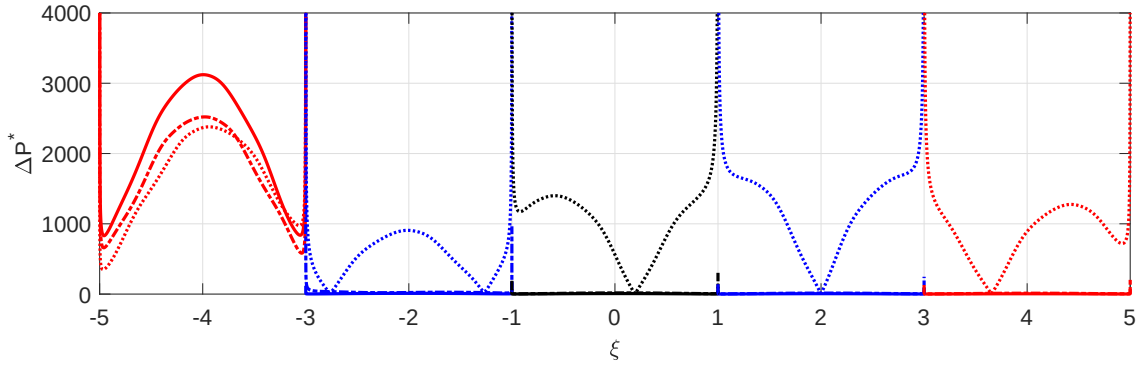

(c)

Figure 3.20: Absolute part of pressure difference across active (left-most) and passive (rest of them) beams at $Re = 0.1$ for heights (a) $\bar{h} = 10$, (b) $\bar{h} = 1$ and (c) $\bar{h} = 0.3$ for $\bar{g} = 8$ (solid), $\bar{g} = 0.4$ (dash-dotted) and $\bar{g} = 0.1$ (dotted).

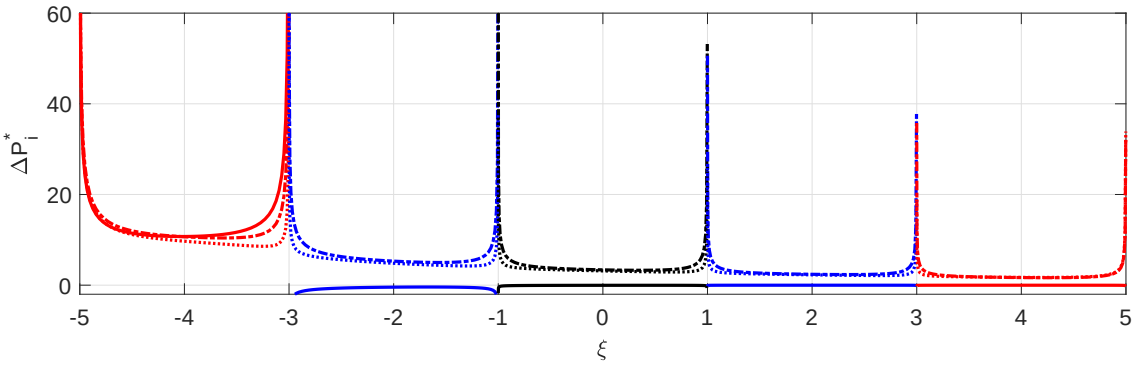

(a)

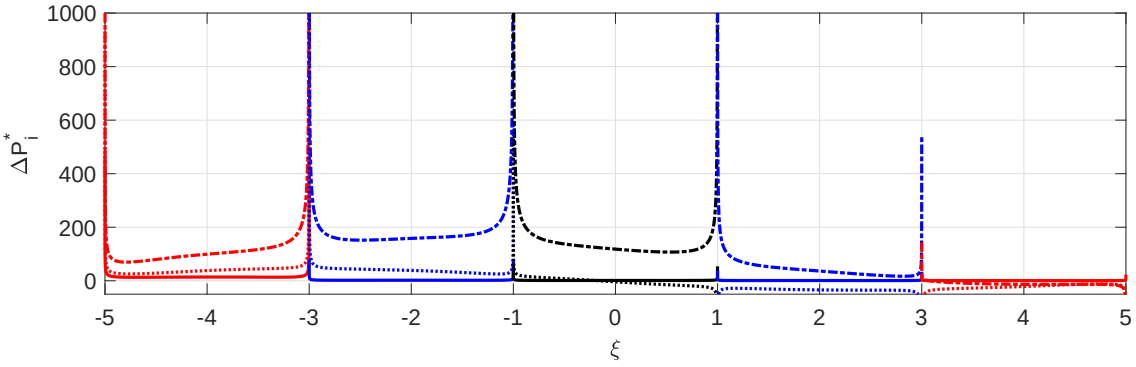

(b)

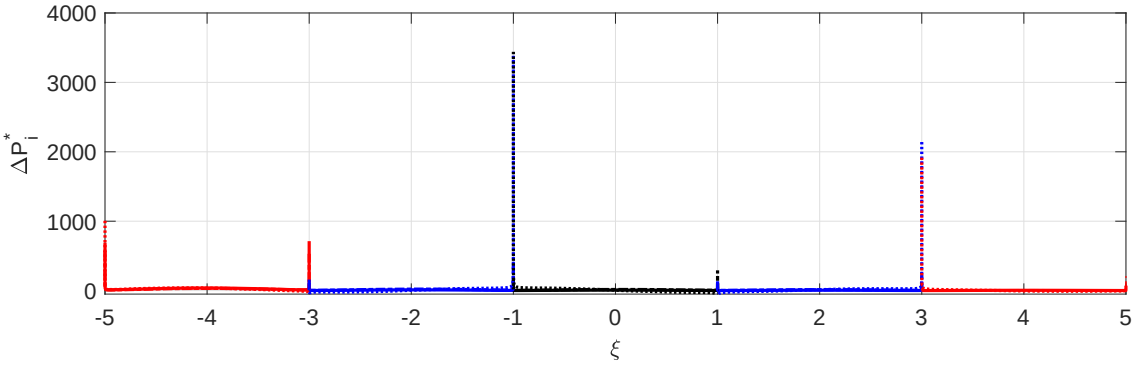

(c)

Figure 3.21: Imaginary part of pressure difference across active (left-most) and passive (rest of them) beams at $Re = 0.1$ for heights (a) $\bar{h} = 10$, (b) $\bar{h} = 1$ and (c) $\bar{h} = 0.3$ for $\bar{g} = 8$ (solid), $\bar{g} = 0.4$ (dash-dotted) and $\bar{g} = 0.1$ (dotted).

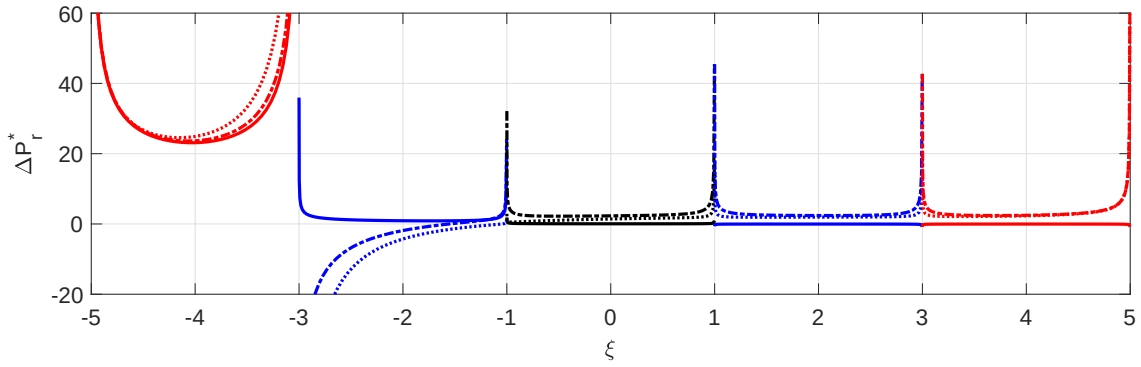

(a)

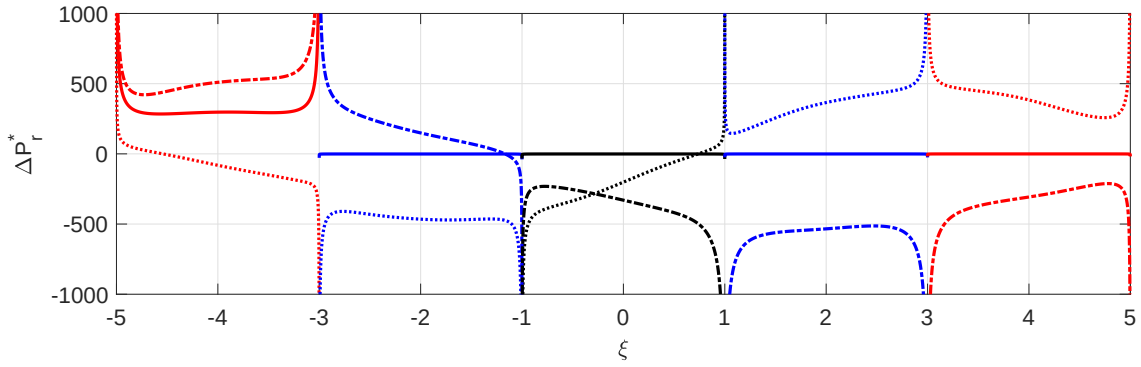

(b)

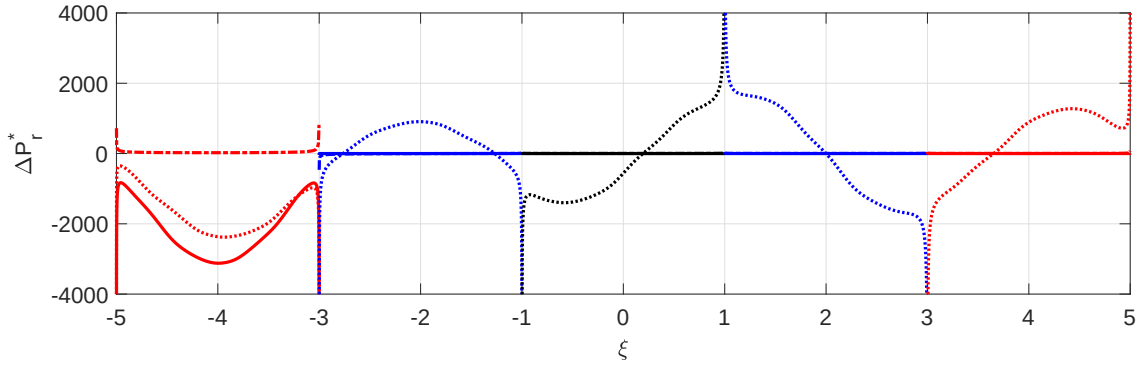

(c)

Figure 3.22: Real part of pressure difference across active (left-most) and passive (rest of them) beams at $Re = 0.1$ for heights (a) $\bar{h} = 10$, (b) $\bar{h} = 1$ and (c) $\bar{h} = 0.3$ for $\bar{g} = 8$ (solid), $\bar{g} = 0.4$ (dash-dotted) and $\bar{g} = 0.1$ (dotted).

Re = 1

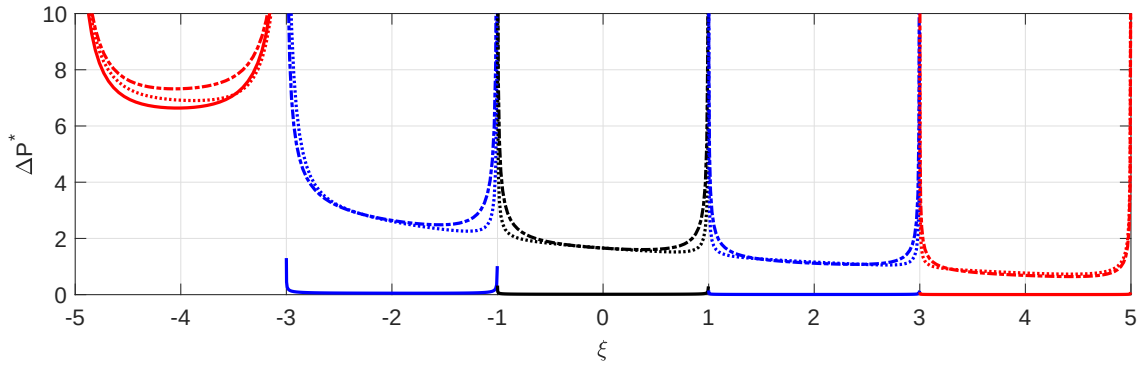

(a)

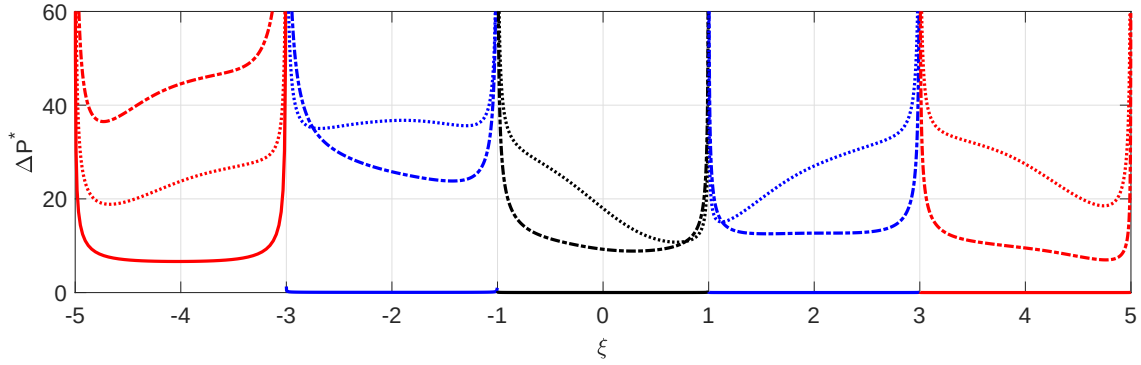

(b)

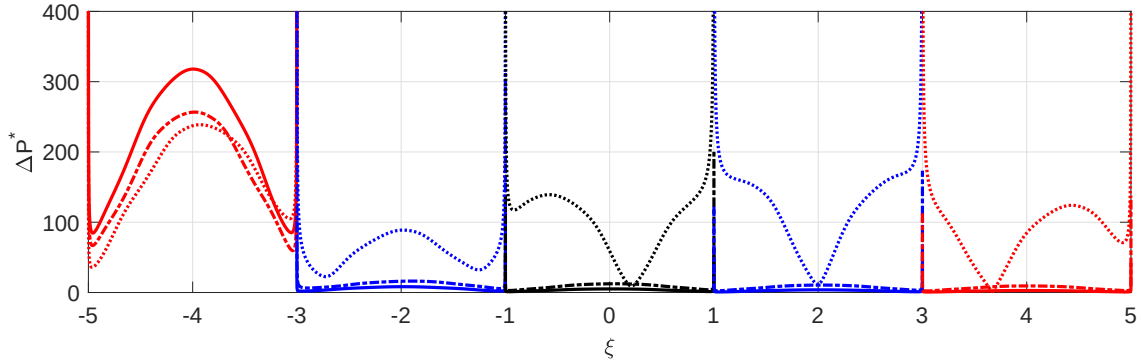

(c)

Figure 3.23: Absolute part of pressure difference across active (left-most) and passive (rest of them) beams at $Re = 1$ for heights (a) $\bar{h} = 10$, (b) $\bar{h} = 1$ and (c) $\bar{h} = 0.3$ for $\bar{g} = 8$ (solid), $\bar{g} = 0.4$ (dash-dotted) and $\bar{g} = 0.1$ (dotted).

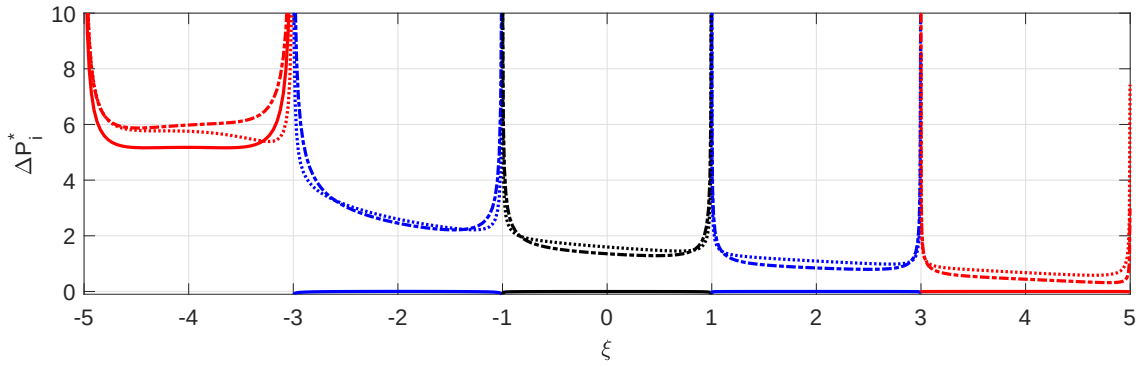

(a)

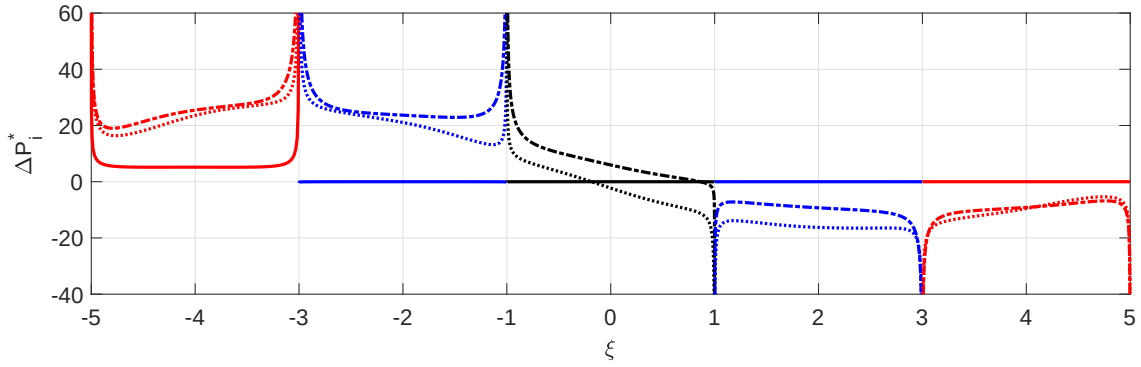

(b)

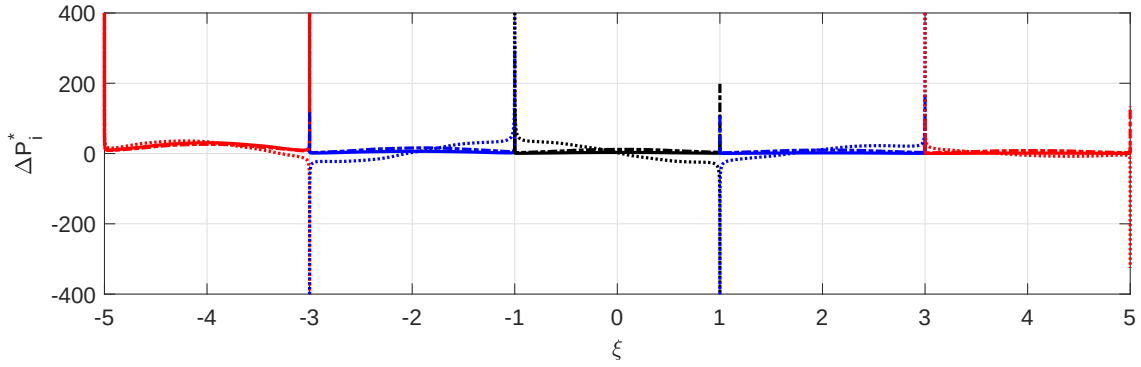

(c)

Figure 3.24: Imaginary part of pressure difference across active (left-most) and passive (rest of them) beams at $Re = 1$ for heights (a) $\bar{h} = 10$, (b) $\bar{h} = 1$ and (c) $\bar{h} = 0.3$ for $\bar{g} = 8$ (solid), $\bar{g} = 0.4$ (dash-dotted) and $\bar{g} = 0.1$ (dotted).

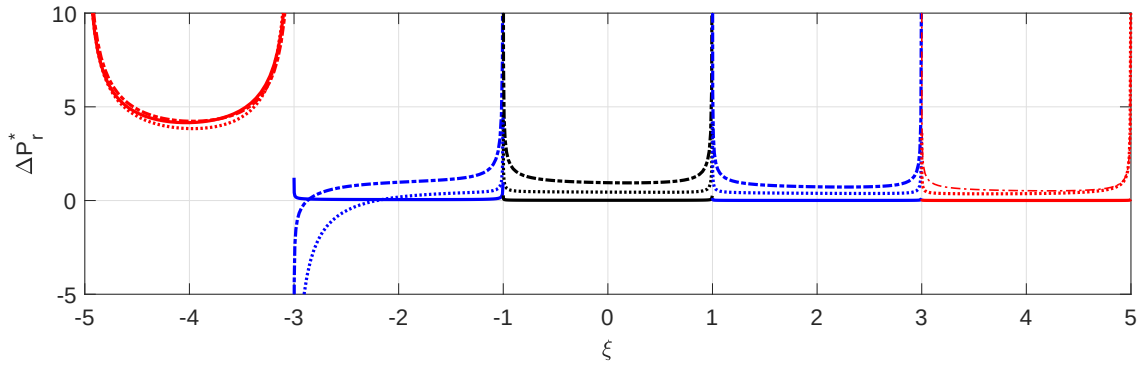

(a)

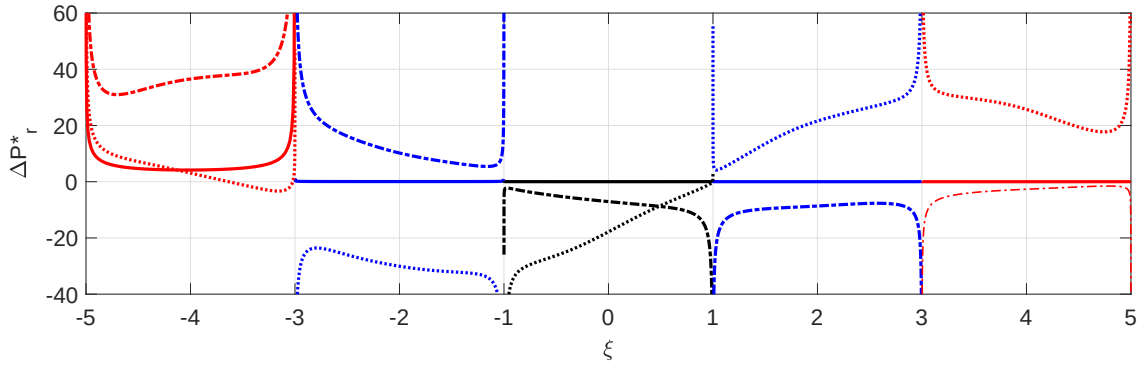

(b)

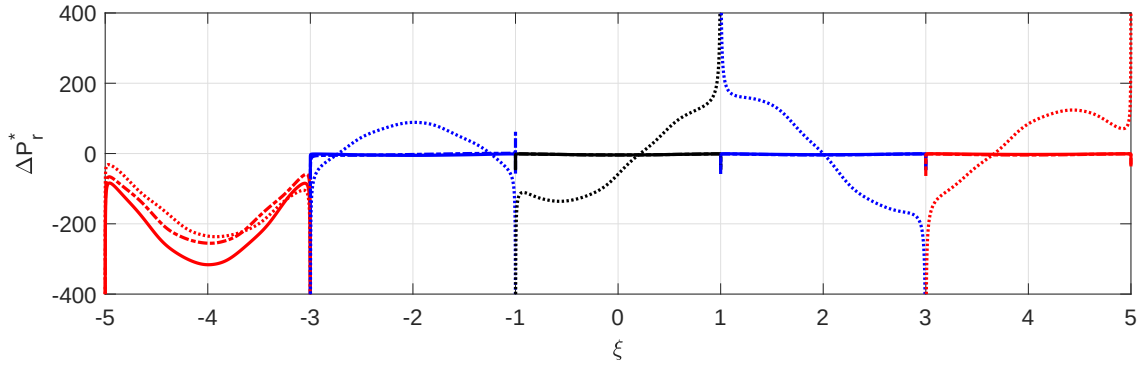

(c)

Figure 3.25: Real part of pressure difference across active (left-most) and passive (rest of them) beams at $Re = 1$ for heights (a) $\bar{h} = 10$, (b) $\bar{h} = 1$ and (c) $\bar{h} = 0.3$ for $\bar{g} = 8$ (solid), $\bar{g} = 0.4$ (dash-dotted) and $\bar{g} = 0.1$ (dotted).

Overall hydrodynamic load A very similar effect is observed as was the case with $Re = 0.1$ but with comparitively reduced overall hydrodynamic load for the corresponding heights and gaps.

Coupling between members The viscous effects continue to have a strong influence with increasing proximity to the surface as was the case with $Re = 0.1$.

Array effects In Figure 3.25 we can observe the array effects vividly with increasing proximity to the surface with it having increased number of nodes with increasing proximity to the surface.

Re = 100

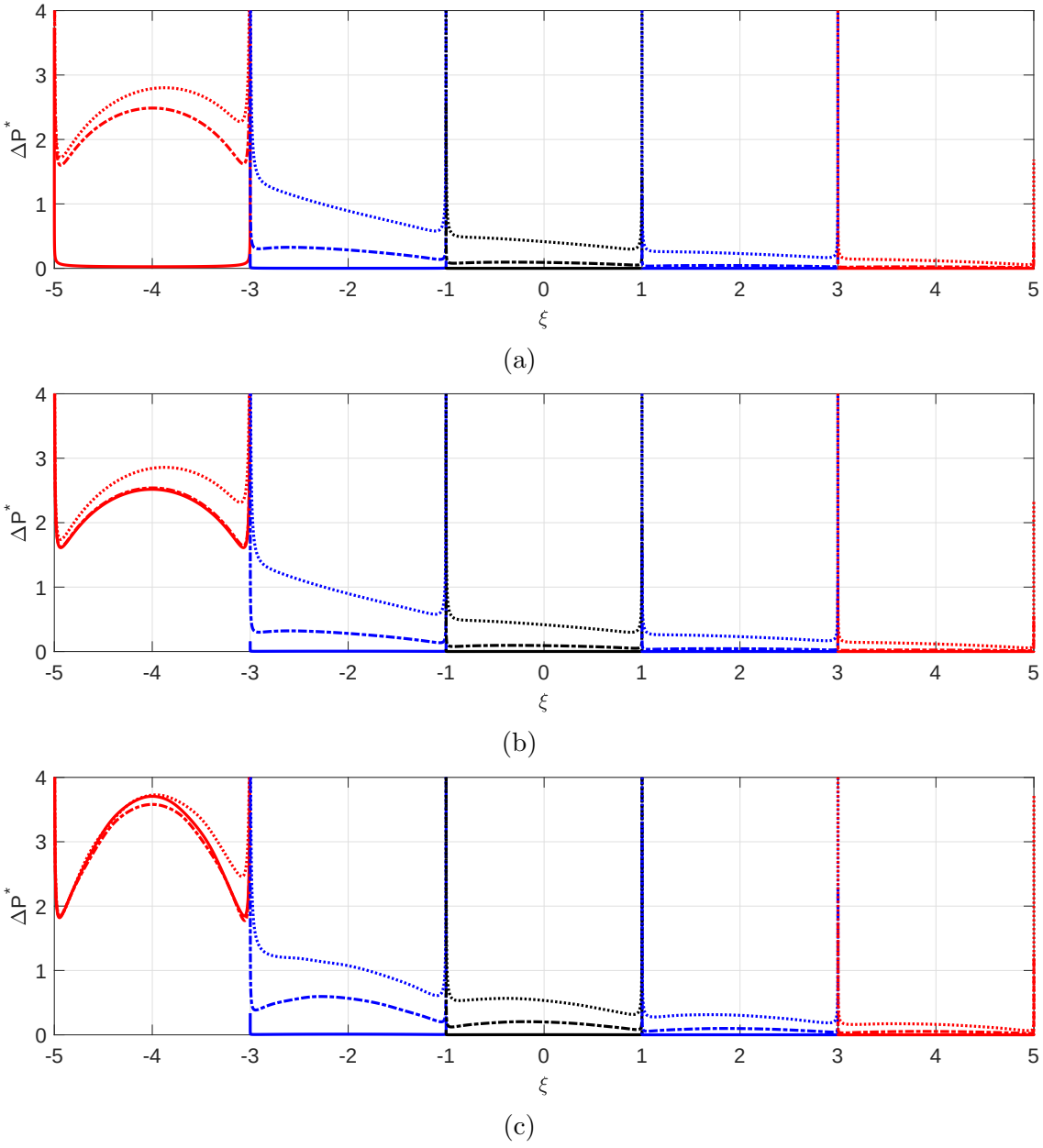

Figure 3.26: Absolute part of pressure difference across active (left-most) and passive (rest of them) beams at $Re = 100$ for heights (a) $\bar{h} = 10$, (b) $\bar{h} = 1$ and (c) $\bar{h} = 0.3$ for $\bar{g} = 8$ (solid), $\bar{g} = 0.4$ (dash-dotted) and $\bar{g} = 0.1$ (dotted).

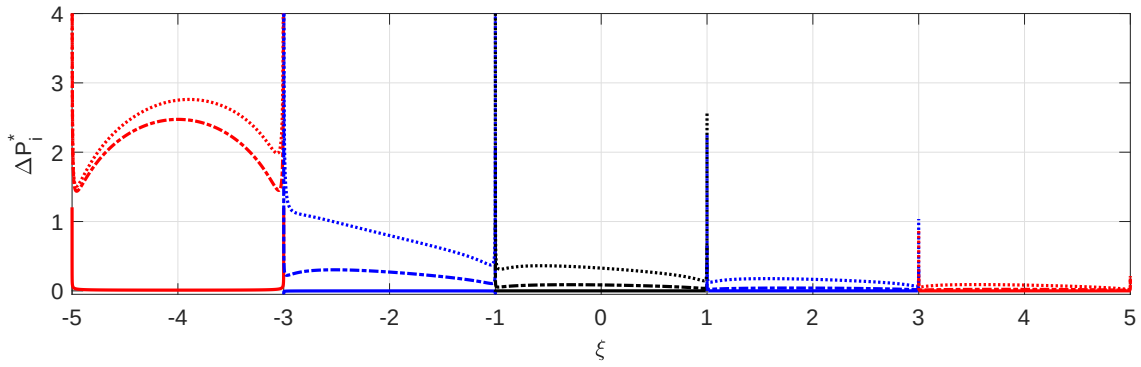

(a)

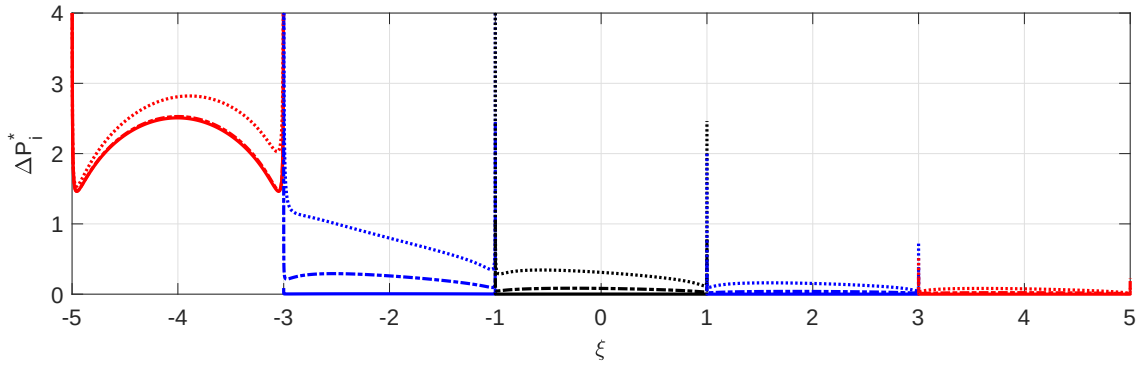

(b)

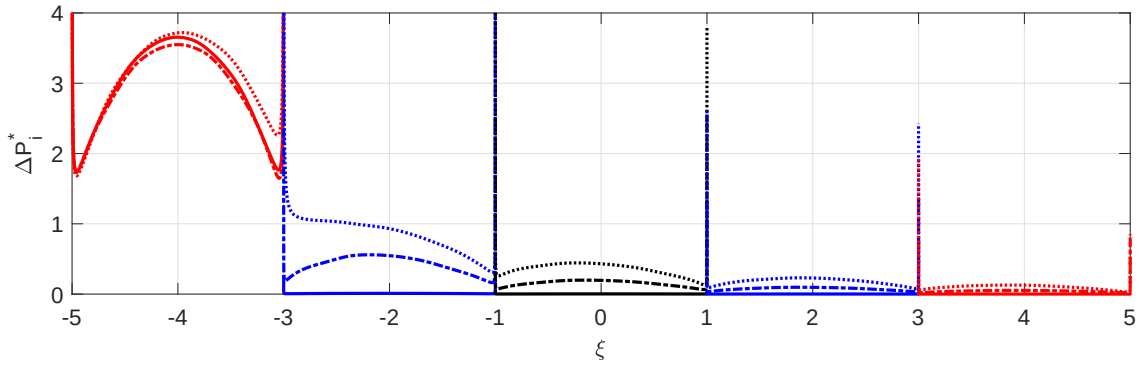

(c)

Figure 3.27: Imaginary part of pressure difference across active (left-most) and passive (rest of them) beams at $Re = 100$ for heights (a) $\bar{h} = 10$, (b) $\bar{h} = 1$ and (c) $\bar{h} = 0.3$ for $\bar{g} = 8$ (solid), $\bar{g} = 0.4$ (dash-dotted) and $\bar{g} = 0.1$ (dotted).

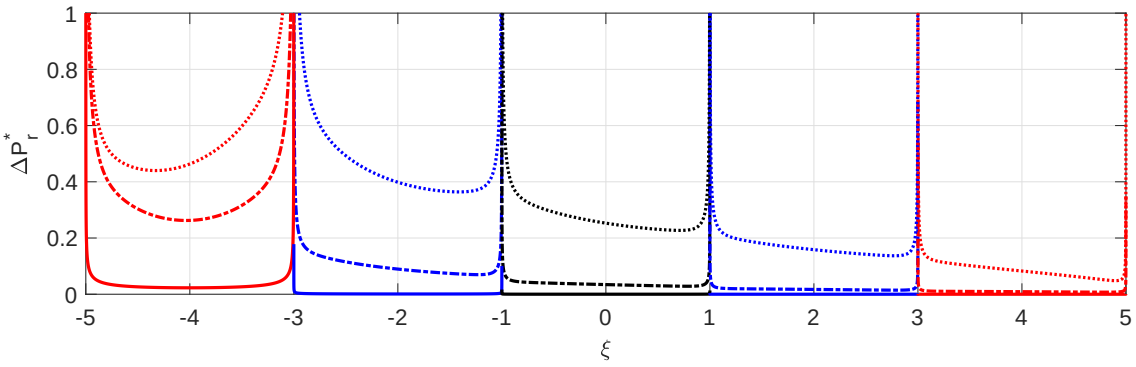

(a)

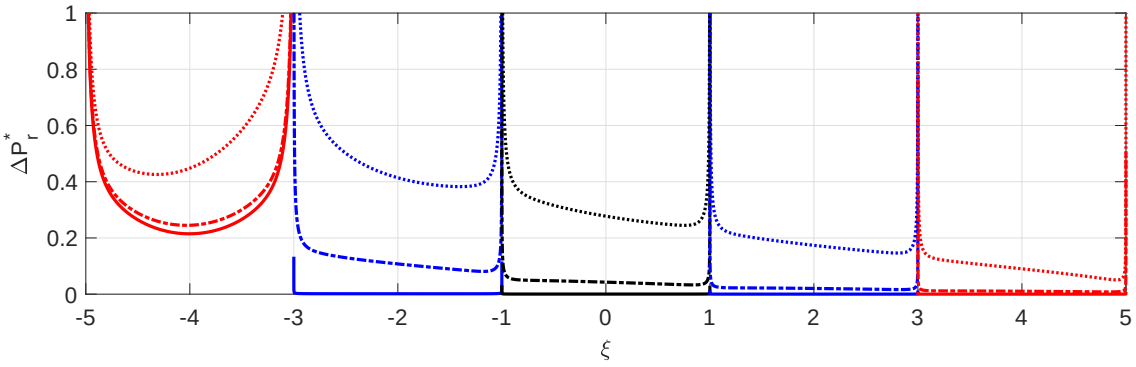

(b)

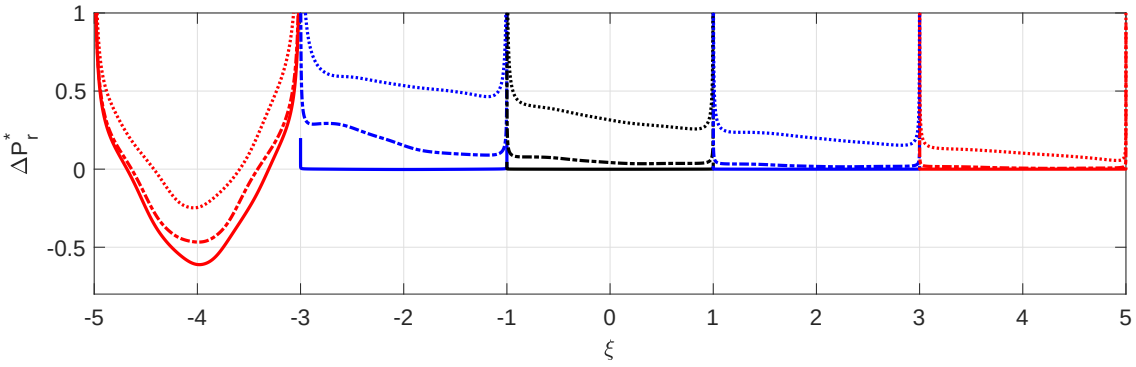

(c)

Figure 3.28: Real part of pressure difference across active (left-most) and passive (rest of them) beams at $Re = 100$ for heights (a) $\bar{h} = 10$, (b) $\bar{h} = 1$ and (c) $\bar{h} = 0.3$ for $\bar{g} = 8$ (solid), $\bar{g} = 0.4$ (dash-dotted) and $\bar{g} = 0.1$ (dotted).

Overall hydrodynamic load The overall hydrodynamic load is significantly less and displays a non-montonic behaviour with decreasing heights.

Coupling between members The added mass dominates the overall dynamics when in close proximity to the surface.

Array effects We note that increasing the number of members in the array does not necessarily result in increased nodes or mode shapes confirming our hypothesis that at high Re, the overall dynamics are localized and is independent of the size of the array.

3.3 Discussion and Conclusions

In this chapter, we studied the fluid coupling phenomena of different sized arrays oscillating in close proximity to a rigid surface subject to steady-state small amplitude vibrations in different configurations, namely, 1-0, 1-0-0 and 1-0-0-0-0. We have derived the governing equations resulting in a hydrodynamic coupling matrix with non-neighbouring member effects incorporated since it was found in Chapter 2 that non-neighbouring members cannot be ignored, see Section 2.7. Raman has observed a non-monotonic behaviour of added mass and viscous damping (coupling effects) in an unbounded fluid medium for varying gaps $\bar{g}$ between the beams. Sader observed an increase in hydrodynamic loading with the viscous dissipation effects dominating the inertial effects when a single beam is brought in close proximity to a surface [21]. We observe that the overall hydrodynamic loading and the coupling effects are mutually dependent on both gaps $\bar{g}$ and heights $\bar{h}$. At low Reynolds numbers i.e. $Re = \{0.1, 1\}$, an increase in overall hydrodynamic load was observed and the viscous effects dominated the overall dynamics with increasing proximity to the surface. At high Reynolds numbers i.e. $Re = 100$, the magnitude of the overall hydrodynamic load is significantly lower in comparison to the low Re cases and displayed a non-monotonic behaviour with increasing proximity to the surface. Also, because of the rather thin boundary layers at high Re, added mass effects dominate the overall dynamics unlike low Re cases in which the viscous effects took precedence.

Also, with increasing array size we note an increase in the overall hydrodynamic load when compared to the corresponding cases of arrays with less members for the respective Reynolds numbers, gaps and heights. The overall trend of hydrodynamic load with increasing length of the array is very similar to that seen in a two-beam array but with an additional effect stemming due to the influence of non-neighbouring members that can be attributed to the array effects and in particular, is enhanced when the beams are close to each other. i.e. $\bar{g} < 0.4$.

Chapter 4

Experimental Design of a test-rig and Comparison of Results

In this chapter we present the design of a test-rig developed to perform experiments to understand the array dynamics of multiple beams in an edge-to-edge array configuration vibrating in a fluid environment. We compare the fluid-coupling effects of our theoretically obtained results with experiments [60]. In our study we emphasize on the coupling ratios of passive beams with respect to the active beam and make comparisons against the numerical simulations in Chapter 2 (infinite fluid domain) and Chapter 3 (in a bounded fluid domain) for different gaps $\bar{g}$ and heights $\bar{h}$ for $Re = \mathcal{O}(100)$ in a pair of beams and a three-beam array. Also, only equal gaps between beams are considered in both experiments and simulations.

4.1 State of the Art

There are a number of experimental test-rigs available in literature that study the dynamics of a single cantilever vibrating in different media [39, 52]. However, there is no equivalent, neither a macro nor a micro-scale test-rig to explore the dynamics of an array of cantilevers vibrating in a fluid environment. There is a greater level of difficulty involved for performing experiments at micro-scale and complexity in measuring data. Therefore existing experimental work which has revealed meaningful insights for the micro-scale dynamics relies on performing experiments at macro-scale [10]. To the author's knowledge there are no micro-scale test rigs as such developed or operated. Likewise, with scaled Re, our work compares to experimental results provided at macro-scale [60]. At the macro-scale gravity plays a significant role whereas at the micro-scale gravitational effects can be neglected. Therefore, cantilevers are hung down vertically in the macro test-rig in order to avoid gravitational effects.

Existing test-rigs not only vary in the number of cantilevers and the medium cantilevers are vibrating in, but also in their arrangement, excitation, imitation of micro-effects and motion measurement [4, 31, 35]. The medium is either air or a viscous fluid such as water, glycerol or silicone oil. External shakers, piezo actuators and an electromagnet combined with a permanent magnet have been used for exciting structures. The motion measurements of the cantilever deflections are done either with a laser-based system, a high speed camera or by strain gauges which are

located near the fixed end of the cantilevers [4, 25, 26].

Existing work on array fabrication at micro-scale, like PRONANO and MILLIPEDE show that it is possible to build and successfully operate arrays up to 4096 cantilevers [54]. However, when it comes to analysis and state of the art or available literature, existing knowledge is only focused on small-size arrays of 2×1, 4×4 or 5×5 in air [34]. Studies that investigate the dynamics in a liquid environment are mainly performed with a single cantilever and existing knowledge from experimental investigations include that the cantilever's frequency response shows a flatter, broader curve (low quality factor) in liquid compared to when vibrating in air [21]. The reduction of frequency is determined by viscous dissipation effects when the cantilever is in close proximity to a surface [21].

4.2 Design of Cantilever

A fluid test-rig is designed to hold a small-size array of cantilevers (up to five) and the design of the test-rig is guided by the cantilever design. The cantilevers in the array need to meet the following criteria: 1) individual actuation, 2) easily changeable gaps between the cantilevers, 3) consistent clamping mechanisms enabling repeatability of experiments and 4) variable length of the cantilever immersed in the fluid.

AFM cantilevers are typically $90 - 460$ μm in length, $25 - 60$ μm in width and $0.7 - 7.5$ μm thick and scaling it by a factor of 1000 results in length of the cantilever between $90-460$ mm which is appropriate for visualization at the macro scale. Hence, the cantilever dimensions were chosen such that it is 150 mm long, 40 mm wide and 1.5 mm thick and made of aluminum. It is actuated by a piezo-actuator pad glued on one side of the structure (see Figure 4.1) and its width b follows the width of the piezoactuator i.e. $b = 40$ mm. Other dimensions are scaled based on factors like size of the array, Reynolds number, dimensions of the test-rig and available actuation and sensing equipment. Four strain gauges, mounted in a full Wheatstone bridge configuration per cantilever is used to measure the cantilever's deflection. The strain gauges are located at the base of each cantilever with two on either sides of it. A small hole at the clamp end of the cantilever allows for easy routing of wires of strain gauge and piezo-actuator.

From a range of fluids which fulfill the requirements of being non-conductive, viscous, devoid of hazard and any unpleasant odour and transparent at all times so the user is able to observe the motion of fluid around the cantilevers using a high-speed camera, our choice of fluid is glycerol. It is also important that the chosen fluid did not cause any corrosive damage to metallic parts and glycerol served this purpose. The fluid properties of glycerol at room temperature are: density $\rho = 1260$ kg/m^3 and absolute dynamic viscosity $\mu = 0.950$ Pa.s. Also, given that high-voltage piezo actuators are glued to the face of the cantilever, it is important to choose a non-conductive fluid. The resonance frequency f_{res} varies depending on the immersion levels of the cantilever in glycerol and also geometry or clamping but is found to be between $30 - 35$ Hz [60]. Using the definition for Reynolds number below:

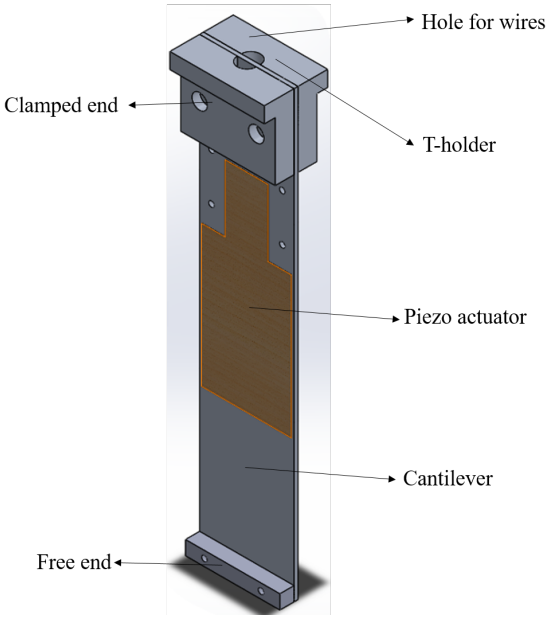

Figure 4.1: Cantilever assembly design

$$Re = \frac{\rho \omega b^2}{\mu} \tag{4.1}$$

where ρ is the density of the fluid, ω is the driving frequency and μ is the dynamic viscosity, we calculate the corresponding Reynolds number in our case to be of order $\mathcal{O}(100)$ and more precisely, Re is found to be between $400 - 443.34$. The width of the beam is an appropriate choice for Reynolds number considered here since it is the dominant length scale causing the transverse oscillations of the cantilever immeresed in fluid. Experiments for other Reynolds numbers could be performed by using fluids of varying viscosities.

The input amplitude of the piezo-actuators and the gap between the cantilevers are varied. The values considered for the input amplitude are $AC_n = \{5, 10, 15\}$ V in air while higher amplitudes $AC_n = \{40, 60, 80\}$ V are chosen in glycerol to observe any significant motion of the cantilevers in the fluid [60], where the subscript $n = 1, 2, 3$ denotes the number of beams in the experiment. Also, a range of gaps $\bar{g} = \{0.025, ..., 0.3\}$ are considered. The immersion depths of the cantilever are nondimensionalised with respect to the length of the beam i.e. $\bar{d} = d/l$.

4.3 Design of Test-rig and Purpose

The main structure of the fluid test-rig followed an initial design by Jackson et al. who designed a smaller test-rig for an array of cantilevers vibrating in air [26]. A CAD view of the designed and built fluid test-rig is shown in Figure 4.2 and a photograph of the fully assembled test-rig is depicted in Figure 4.3. While in this section we focus on key design specifications that directly relate to desired performance of the experiment, details of manufacturing, fabrication, assembling the test-rig, power and electronics have been documented by Jackson [26], Wagner [60] and Raedar [47]

as pointed out earlier.

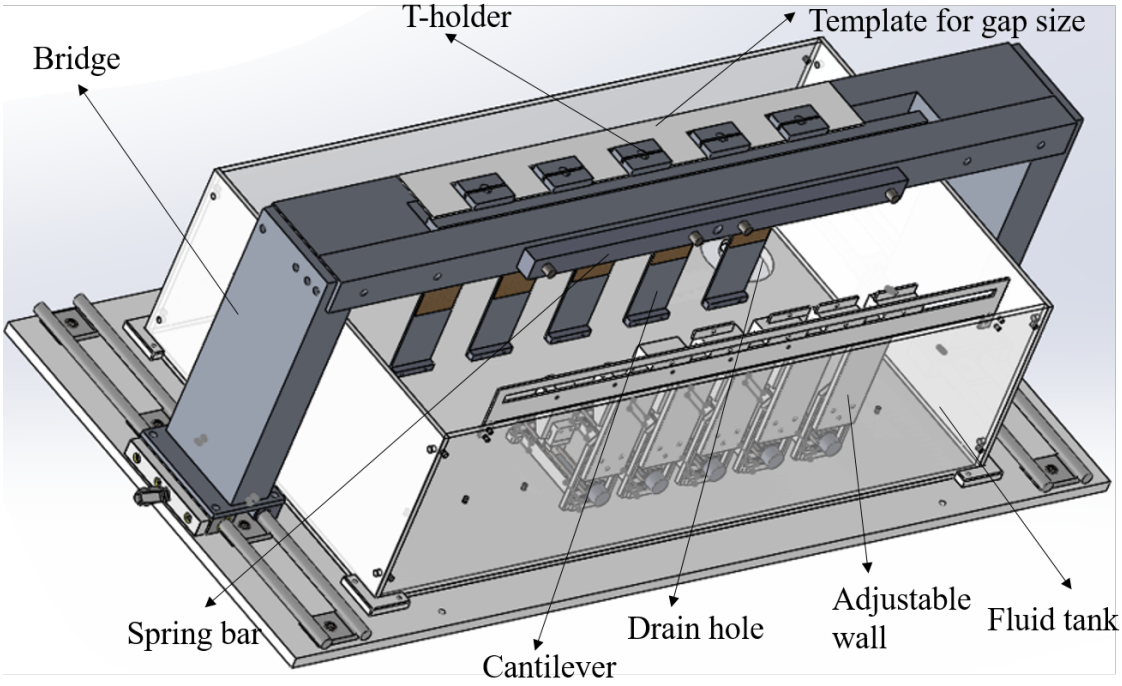

Figure 4.2: CAD model of the fluid test-rig.

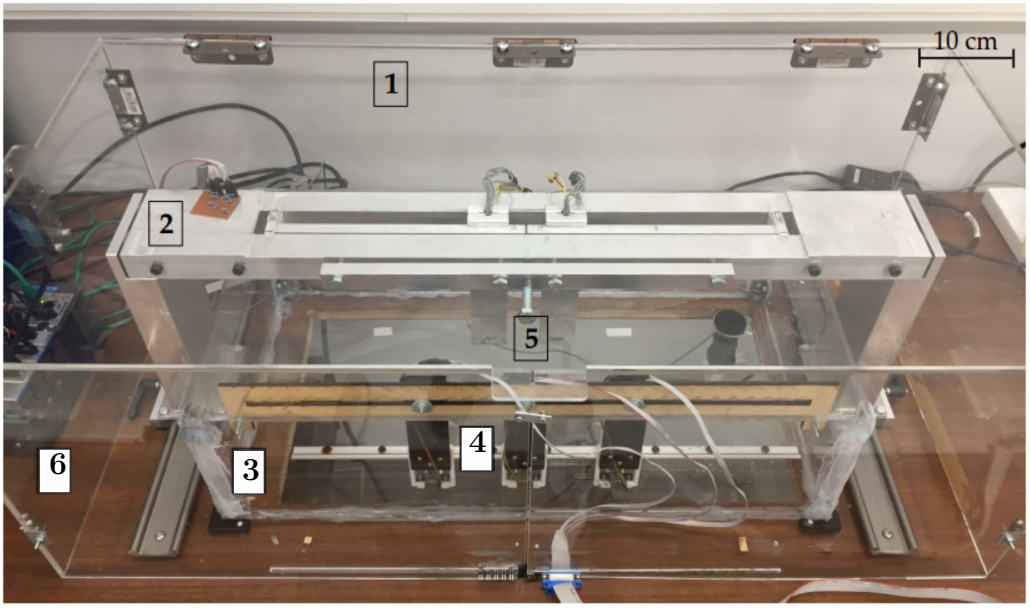

Figure 4.3: Test-rig set up: Two cantilevers clamped at bridge 1) safety box, 2) bridge with separate clamping mechanism, 3) fluid container, 4) wall (individually adjustable), 5) cantilevers and 6) actuation hardware [60, p.26].

4.3.1 Test-rig requirements and design specifications

A series of design requirements are identified to enable comparing results with numerical results in Chapters 2 and 3.

Fluid tank- The test-rig is designed for investigating up to five cantilevers such that it is simple to vary the gaps $\bar{g}$ between them as well as immersion heights of cantilevers.

Based on the scaling study performed for $Re = \mathcal{O}(100)$, the size of the fluid tank is chosen to be $6200 \times 3200 \times 1700$ mm^3. The tank is designed such that it is capable of holding up to five cantilevers with a maximum gap of twice the beam's width (2×40 mm) between them since it is found from our numerical simulations (see Section 2.5, Figure 2.13) that interesting phenomena (e.g. coupling effects) occur for $\bar{g} < 2$. Other factors that contributed to its design are the maximum immersion of the cantilevers. The depth of the cantilever immersed could be varied by having more or less fluid in the tank. Also, due to one of our primary motivators of research being applications of an array of AFM cantilevers in close proximity to a surface, attention was given to change the distance of array and individual beams to compare the wall effects in the case of an array from or to a rigid wall. Unlike in Chapter 3 where we bring the beams in close proximity to the surface, the experimental setup is designed such that the distances $\bar{h}$ between the beams and the wall is adjusted by moving the bridge. A rectangular cutout in the table was made (covered with Perspex) on which the fluid tank was placed allowing transparent viewing of the cantilever motion and fluid flow surrounding it through a high-speed camera from below. A hole is placed in one of the corners in the tank to drain the fluid and to allow for exchangeability of fluid environments.

Clamping mechanism- The design of the clamping mechanism fulfills two main criteria: 1) to minimize mechanical coupling between members and 2) to allow for equal clamping properties (force, location, angle etc.) allowing repeatability of experiments; for manufacturing and installation details the reader is referred to [47].

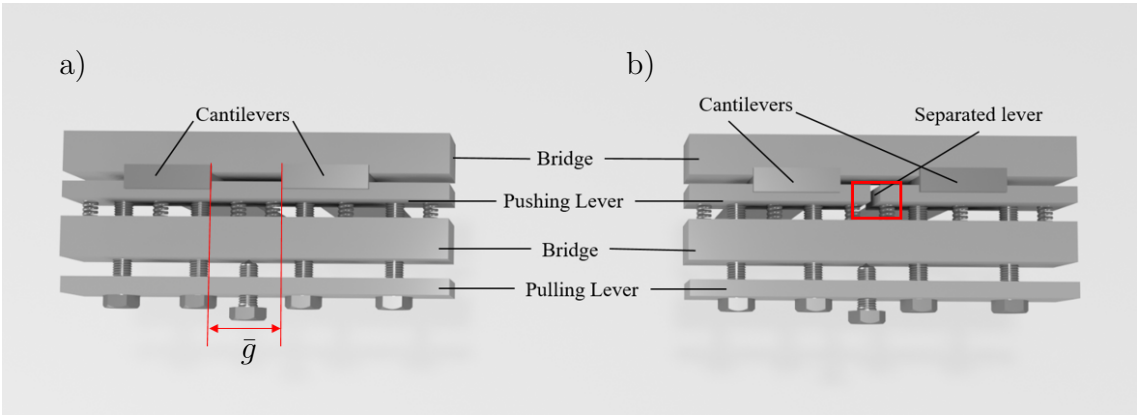

Figure 4.4: Sketch of the clamping mechanism in the test-rig with the two beams clamped on a) a common lever (left) and b) a separate lever (right), top view

As a result the current design of the bridge comprises of a separate base for each cantilever such that they can be sandwiched between any two T-shaped aluminum

blocks, see Figs. 4.1 and 4.4. Usage of compression springs and T-holders to clamp the cantilevers ensured that the clamping mechanism is consistent (Figure 4.4) and realization of variability of gaps between cantilevers with ease was ensured using templates of gapholders made of Perspex.

We are primarily interested in comparing our simulated results emphasizing on the fluid-coupling effects in an array of beams vibrating in an infinite fluid domain and in close proximity to a surface. For that, two set-ups are examined in air: a) cantilevers clamped on a common lever, b) cantilevers clamped on separate levers as shown in Fig. 4.4 in order to determine the mechanical coupling. We have reproduced the experimental results of common and separate levers, which are presented in Fig. 4.5 [60].

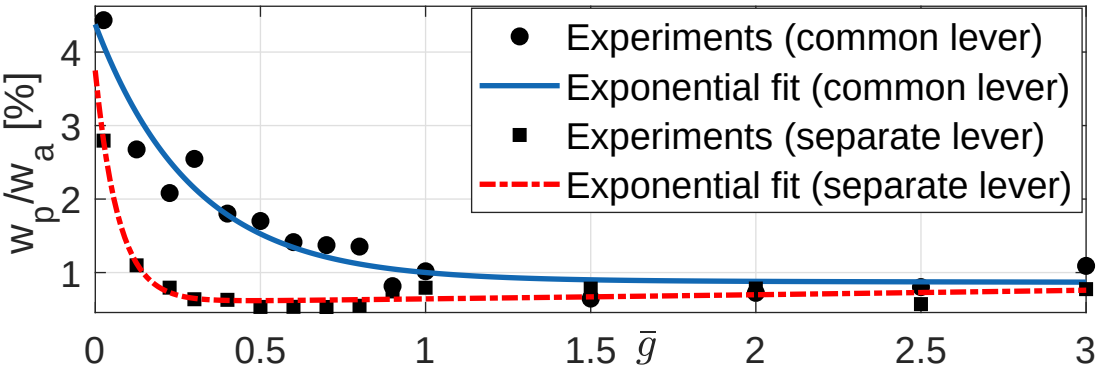

Figure 4.5: Coupling ratio (in percentage) between two beams as a displacement amplitude of passive beam w_p with respect to active beam w_a; input amplitude $\hat{AC}_n = 15$ V; common lever (circular markers) and separate lever (square markers); actual data indicated by markers and also plotted is an exponential fit of the data.

Also, only the first beam is excited while the remaining beams are passive. Hence, the absolute coupling impact of the first beam onto the second beam and so on can be directly measured by evaluating ratios of passive to active members.

It is clearly observable for gaps $\bar{g} < 1$, the influence of coupling is significantly different when clamped on a separate lever to it being clamped on a common lever and for the smallest gap the difference is about $2 - 3\%$. Also, the coupling decays quickly when the beams are clamped on a separate lever as the gap increases whereas for the common lever the decay rate is slower. This confirms that also mechanical coupling plays an increasing role with decreasing gap size and needs to be considered or avoided to minimize mechanical coupling effects. This can be achieved by having the cantilevers clamped on separate levers allowing us to investigate the fluid-coupling effects in detail but not for gaps $\bar{g} < 0.8$ since the coupling ratio is greater than 1%.

4.4 Summary of the experimental setup

The experimental setup comprises of a function generator, a power amplifier, software and a PC. The cantilevers are submerged in a fluid tank of 40 litre capacity.

Wagner [60] performed experiments for a range of gaps $\bar{g}$ and distances $\bar{h}$ in a two- and a three-beam array. Two different immersion levels $\bar{d} = \{0.07, 0.1\}$ are considered. Note that the immersion levels are scaled with respeect to the length of the cantilever.

Three white markers as shown in Figure 4.6 are placed at the edges and the midpoint of each cantilever's cross-section which enabled to accurately set distances $\bar{h}$ between the tip and wall resulting in accurate wall distances for the experiments and is measured with high-speed camera.

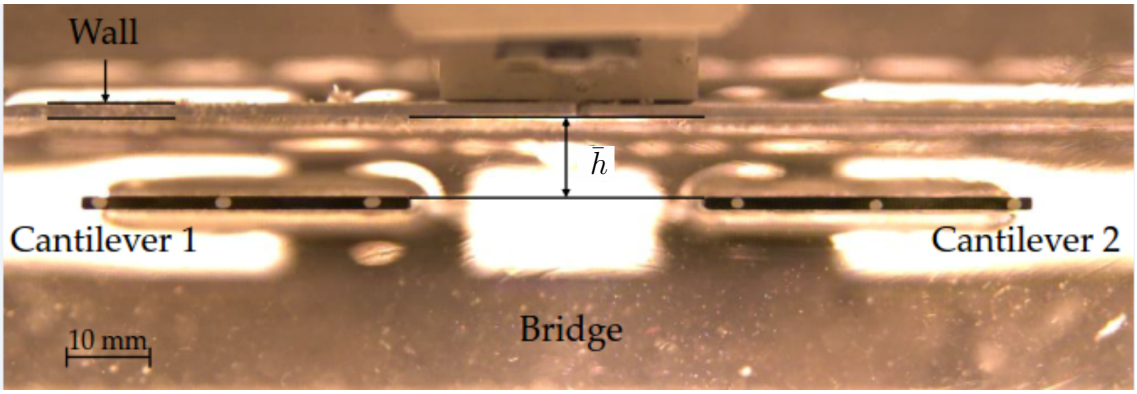

Figure 4.6: A photographic view of the test-rig from below in which two beams are immersed in glycerol and are at a distance $\bar{h}$ from the wall.

The high-speed camera is able to deliver a maximum nondimensional deflection resolution of up to 5×10^{-7} (dimensional value of 20 μm) and maintains a ratio of 1024×1024 pixels for a frame rate of up to 7000 frames per second. In real time, the high-speed camera is connected to the computer via an ethernet cable allowing direct observation of the fluid and the cantilever tip's motion. Photron FASTCAM Viewer software is used to measure and adjust the distance between the sample wall and the cantilever tips. Further, a high performance LED light is used to achieve a consistent and sufficient exposure. While the static distances are set with the camera, the motion is tracked using strain gauges (NI modules).

The test-rig is operated by NI modules and controlled by an embedded FPGA controller with LabVIEW. For detailed information on the implementation of each module and the code used in LabVIEW software the reader is referred to [26].

4.5 Comparison to numerical simulations

In this section, we compare the numerical simulations performed at $Re = 100$ against experimental results ($Re = \mathcal{O}(100)$) to investigate the effect of gaps between beams, effects of non-neighbouring members and the surface effects when the beams are in close proximity to the surface. As a result of small amplitude vibration assumption, hydrodynamic loading on the cantilever becomes a linear function of its displacement. The pressure drops are directly related for constant hydrodynamic coupling

matrix and a particular Reynolds number. Hence, we compare the ratios of pressures in numerical simulations to ratios of displacements in experiments since for constant Reynolds number the pressure is directly proportional to the velocity and thus also the displacement.

4.5.1 Effect of the gap

In Figure 4.7, we compare the influence of gaps with two beams immersed in glycerol at a depth $\bar{d} = 0.1$ (10 % of its length) in an infinite fluid domain. A small depth of immersion is desirable so as to replicate our numerical simulations which considered a two-dimensional model. Figure 4.7 shows a qualitative comparison between experiments and simulations of coupling ratios for two beams immersed in glycerol with varying gaps between them in a 1-0 configuration. The coupling ratio from the experiments is plotted as a ratio of the amplitudes of the passive cantilever with respect to the active cantilever actuated at $\hat{AC} = 80$ V when the beams are clamped on separate levers. Also, plotted from numerical simulations in Chapter 2 is the coupling ratio as a ratio of the normalized hydrodynamic force of the passive beam with respect to the active beam.

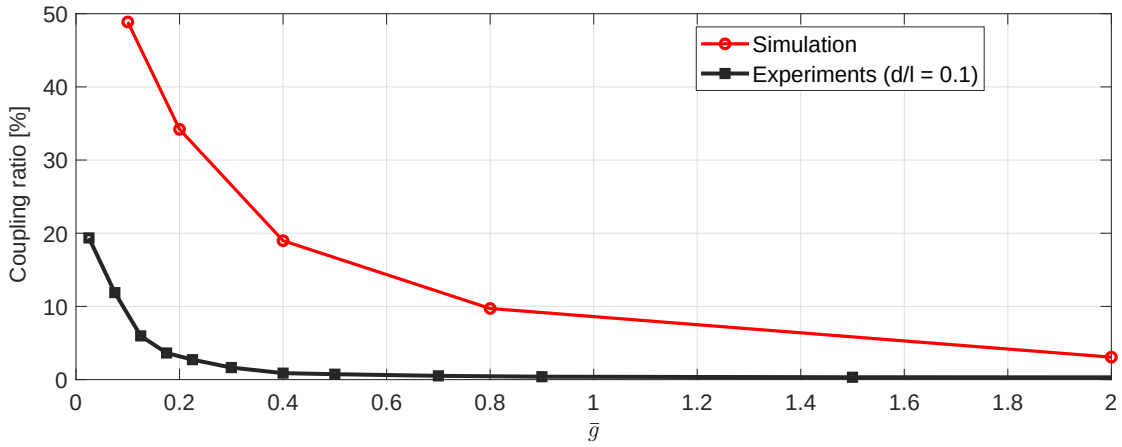

Figure 4.7: Coupling ratio as a precentage of passive beam with respect to active beam; comparison between experimental results (w_p/w_a) for $Re = \mathcal{O}(100)$ and numerical simulations ($\bar{F}_p/\bar{F}_a$) for $Re = 100$.

We note that the influence of coupling drops significantly with increasing gaps between the beams. The quantitative discrepancies between experiments and simulations can be attributed to a number of factors: 1) in our simulations we have assumed a two-dimensional thin ribbon oscillating whereas in our experiments the beam is a three-dimensional object immersed 15 mm (10 % of its length) into the fluid; 2) experimental investigations involve fluid-structure interactions whereas simulations consider only fluid related influences; 3) since the focus of this work is a qualitative understanding no exact parameter match was undertaken, e.g. Reynolds number of experiment is $Re \approx 400$ while the simulations are carried out for $Re = 100$. From the investigation we undertake, it can be seen that a qualitative match is sufficient to understand the underlying physics. Also, matching exact parameters would im-

ply operating the beams in a highly viscous fluid. This would require a re-design of the cantilever as the width of the piezo-actuator would have to be increased in order to move the highly viscous fluid. Note, that with increasing Re the influence of coupling decreases, see Figure 4.7.

4.5.2 Effect of the non-neighbouring members

According to results of Section 2.5.1, a three-beam array is compared with three different actuation scenarios: a) left-most beam active (1-0-0), b) middle beam active (0-1-0) and c) right-most beam active (0-0-1) to compare our findings on the significance of non-neighbouring members, coupling effects and overall loading. We present coupling in percentage as a ratio of passive beam's amplitude w_p to that of the active beam w_a below when the beams are far away from the wall immersed in glycerol at a depth of $\bar{d} = 0.1$ experimentally and compare it against numerical calculations performed for the 1-0-0 and 0-1-0 configurations (see Section 2.5.1, Figures 2.13 d and 2.14 d).

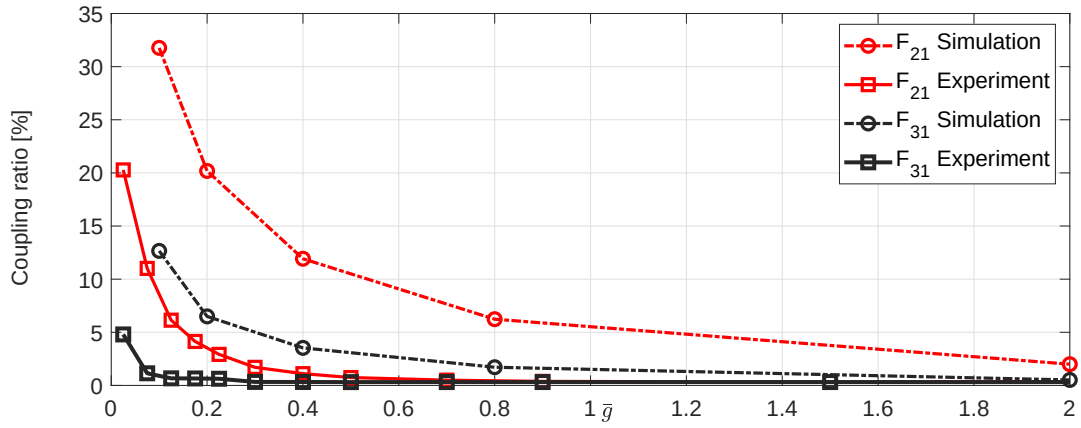

Figure 4.8: Coupling ratio of passive beams 2 and 3 with respect to active beam 1 in a 1-0-0 configuration; comparison between experimental results for $Re = \mathcal{O}(100)$ and numerical calculations for $Re = 100$.

We observe from Figure 4.8 that as the gaps between the beams decrease the coupling ratio of the nearest neighbour (black) increases significantly i.e. for $\bar{g} < 0.8$. We also observe that the non-neighbouring member effects (red) start to increasingly become significant for smaller gaps i.e. $\bar{g} < 0.4$ and imply that for such gaps, non-neighbouring members cannot be neglected and array effects dominate the overall dynamic behaviour. This can equally be observed in both simulations and experiments. Also, quantitative discrepancies observed between experiments and simulations are again associated to factors discussed in the previous Section 4.5.1.

The 0-1-0 configuration, where the outer beams are passive and the middle beam is actuated is comparable to 1-0 configuration for two beams, see Figure 4.9. As previously observed the coupling ratio increases significantly for $\bar{g} < 0.8$. Small discrepancies in coupling ratio observed in the experiments among the two outer beams with respect to the active beam is likely due to manufacturing deficiencies

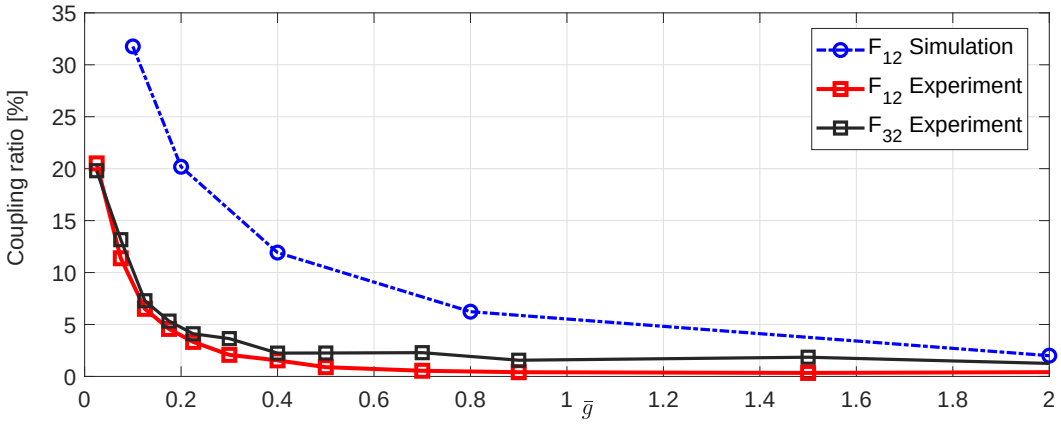

Figure 4.9: Coupling ratio of passive beams 1 and 3 with respect to active beam 2 in a 0-1-0 configuration; comparison between experimental results for $Re = \mathcal{O}(100)$and numerical calculations for $Re = 100$.

of the two cantilevers resulting in different properties and therefore, resonant frequencies. Also, comparing Figures 4.8, 4.9 and 4.10 we observe that critical gaps do not seem to shift much with changing the position of the active beam in the array, however, there is a slight change in the coupling ratio due to the active beam in 0-1-0 configuration being subjected to hydrodynamic influences from members on either side whereas in the 1-0-0 case, it is subjected to influence from only one member. In Figure 4.10, we compare the coupling ratios of passive beams with respect to active beam for different configurations in a two- and a three-beam array in which one beam is active while the rest is/are passive. We are interested in the 1-0 coupling effects in **1-0**, **1-0**-0 and 0-**1-0** configurations. Experimental results (square markers) do not suggest any distinguishable features between different array sizes and position of the active beam in the array. However, we observe a distinct trend in case of a two-beam array in comparison to a three-beam array numerically (circular markers). The result implies a reduction in overall hydrodynamic load or coupling influence with increasing array size in which beams are closely spaced i.e. for $\bar{g} < 2$, see Section 3.3. However, experimental results don't seem to show this. One possible explanation could be that the presence of mechanical coupling is dominating the behaviour and therefore any fluid effects associated to the size of the array is negligible for this range of parameters. The fluid-coupling effects needs to be further investigated especially for large-sized arrays experimentally. The presence of mechanical coupling is further strengthened for a three-beam array since two beams are mounted on separate levers while parts of the middle beam (beam 2) rests on both levers. The quantitative discrepancies observed between experiments and numerical simulations could be attributed to reasons discussed in Section 4.5.1.

4.5.3 Wall effects

In this section we compare our results for two beam hydrodynamics in close proximity to a wall immersed in glycerol. The distance $\bar{h}$ between the wall and the beams is varied to understand the effects of varying distances on the overall dynamics alongside other factors previously explored such as gaps between the beams etc.

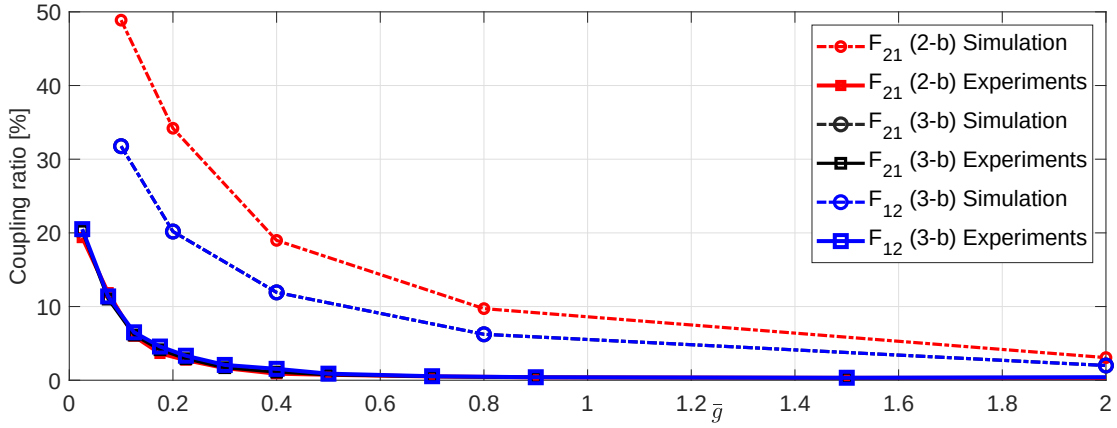

Figure 4.10: Coupling ratio of passive beams with respect to active beam 2 in a 1-0, 1-0-0 and 0-1-0 configurations; comparison between experimental results for $Re = \mathcal{O}(100)$ and numerical calculations for $Re = 100$.

A photograph taken by a camera of two beams immersed in glycerol and vibrating in close proximity to a wall is shown in Figure 4.6. We consider only the case in which the beams are clamped on a separate lever in order to eliminate mechanical coupling effects. Also, we compare the hydrodynamics for gaps between the beams $\bar{g} < 1$ since the analysis of the previous section suggested that coupling effects are especially shown in this regime.

In Figure 4.7 a comparison of coupling ratio with varying gaps $\bar{g}$ is made between experimental observations and numerical results when the beams are in an infinite fluid domain. Note that we use results obtained for $\bar{h} = 10$ numerically (see Figure 4.7) to compare it against $\bar{h} \to \infty$ in experiments. We observe that the coupling ratio increases noticeably for $\bar{g} < 0.4$ when the beams are far from the wall.

Wagner [60] experimentally investigated the coupling ratios for two beams immersed in glycerol for varying gaps $\bar{g}$ and varying heights $\bar{h}$ and the results are reproduced in Figure 4.11.

The trend for red lines indicate two distinct trends when the beams are far away and in close proximity to the wall with the coupling significantly increasing when far away i.e. for $\bar{g} < 0.4$. However, when in close proximity to the wall i.e. $\bar{h} < 0.3$, we notice the red line to be convex for close gaps and plateauing with increasing gaps.

The trend for small $\bar{g}$ is shown by green line signifying that there is a critical gap, here at $\bar{g} = 0.025$ and height $\bar{h} = 0.1$, at which the coupling effects are minimal, implying the coupling is not monotonically increasing with $\bar{g}$ and $\bar{h}$. More details can be found in Chapter 5, p. 98.

A more direct, qualitative comparison of close to the wall numerical results at $\bar{h} = 0.3$ is made against the experimental trend (for $\bar{h} = 0.05$) in Figure 4.12. We observe that the experimental results make a qualitatively good match and we ob-

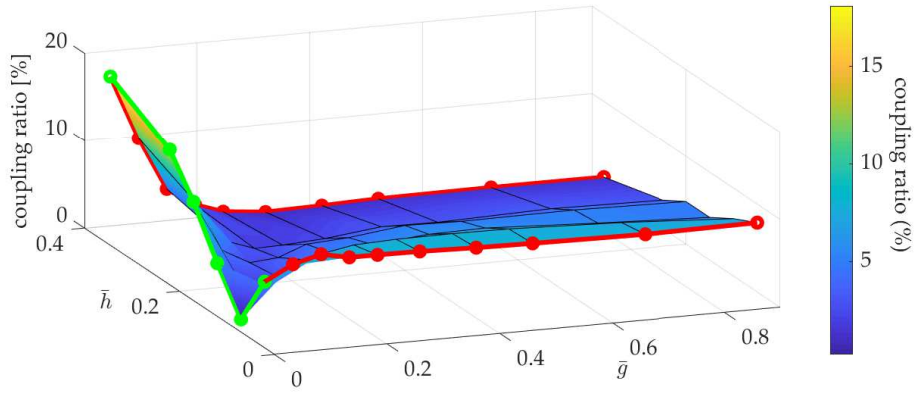

Figure 4.11: Coupling ratio of passive to active beam (as a percentage) for two beams immersed in glycerol in close proximity to a surface for varying gaps $\bar{g}$ and varying heights $\bar{h}$; red lines indicate comparable trends for $\bar{h} \to \infty$ and $\bar{h}$ for close proximity to the wall, compare with Figure 4.7 for $\bar{h} \to \infty$ and Figure 4.12 for $\bar{h}$ when close to the wall.

serve the plateau effect which is distinctively different from the trend seen in the far away case, compare Figure 4.7. This implies that the coupling does not explicitly depend on the gaps and heights but rather mutually on both gaps and heights.

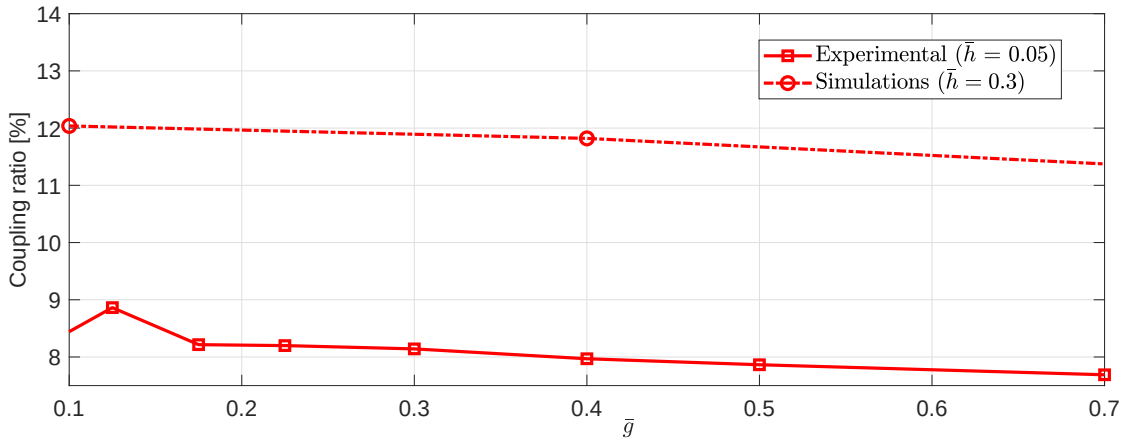

Figure 4.12: Coupling ratio close to the wall of passive to active beam (as a percentage) for varying gaps $\bar{g}$ and heights $\bar{h}$ in case of two beams immersed in glycerol; experimental results (solid line, square markers) for $Re = \mathcal{O}(100)$ and numerical results (dash-dotted line, circular markers) for $Re = 100$ [60, p. 79].

However, a detailed and accurate numerical analysis for more gaps and heights is necessary in order to quantitatively compare the results against experiments.

4.6 Discussion and Conclusions

In this chapter a design of the fluid test-rig is presented to operate a maximum of up to five cantilevers in a fluid environment for varying gaps $\bar{g}$ between the beams and

varying heights $\bar{h}$ or distances from the wall. A qualitative comparison of results is made against numerical results for $Re = \mathcal{O}(100)$ for a two- and a three-beam array and different configurations, namely, 1-0, 1-0-0 and 0-1-0 in which 1 represents the active beam and 0 represents the passive beam. Experimental investigations were performed by Wagner [60] and provided only meaningful results for two and three beams, which we use to compare selected cases from our simulations of Chapters 2 and 3.

A strong coupling is noticed in a two-beam active-passive configuration for decreasing gaps between the beams experimentally for $\bar{g} < 1$. It provides a qualitatively similar trend to that observed from numerical simulations for $Re = \mathcal{O}(100)$.

A comparison is made on the significance of non-neighbouring members in a three-beam array in which the coupling ratio of the nearest neighbour was significant for $\bar{g} < 0.8$, while the coupling strength of non-neighbouring member increased for gaps $\bar{g} < 0.4$. A good qualitative agreement was observed between experiments and simulations implying that non-neighbouring members become significant with increasing array size and their significance is enhanced when the beams are closely spaced i.e. for $\bar{g} < 0.4$.

We also compared the coupling ratios in different sized-arrays (1-0, 1-0-0 and 0-1-0) and found that the coupling ratios did not change significantly in experiments. This implies that location of active beam in the array did not alter the array dynamics for $Re = \mathcal{O}(100)$ due to the localized boundary layers. It is also observed both, experimentally and numerically, that the coupling effects depend not exclusively on gaps $\bar{g}$ or heights $\bar{h}$ but mutually on both gaps $\bar{g}$ and $\bar{h}$, as well as the size of the array.

While our numerical simulations consider fluid coupling only, mechanical coupling effects could not be ignored altogether in the experimental setup resulting in observed quantitative discrepancies. Amongst others, three-dimensional effects and fluid-structure interactions arising from the beams experimentally could have contributed to the observed discrepancies. Though the flow parameters in experiments and simulations are of the same order of magnitude, they are not exact resulting in differences in coupling ratios predicted numerically and experimentally.

Chapter 5

Conclusions and Future outlook

5.1 Conclusions

In this thesis we have developed analytical models and designed experimental tools to analyze the coupled hydrodynamics of small-sized arrays in fluids for a range of applications.

In Chapter 2 additional coupling contributions due to non-neighbouring members were incorporated in order to investigate their effects on the hydrodynamic loading manifested as added mass and damping in a three- and a five-beam array with the first beam activated while the rest remained passive. It was found that both added mass and damping effects were significantly impacted determining the dynamics of array and cannot be neglected for arrays having more than three members. In particular, the effect was enhanced for gaps $\bar{g} < 0.4$.

Building upon the boundary integral formulation used in Chapter 2, we formulated a mathematical model for M beams vibrating in close proximity to a rigid surface in Chapter 3. Our formulation in close proximity to a surface combines an array of beams vibrating in an unbounded fluid media (Raman's model) and a single beam vibrating in close proximity to a surface (Sader's model) and hence, can be applied to study both far- and near-field cases. The focus of our analysis was on overall hydrodynamic load and the coupling strength. Coupling strength depends on the gap between the beams and the height from the surface. A key conclusion from findings in Chapter 3 is that the hydrodynamic coupling need not necessarily be the largest for the smallest gap and height but rather it occurs at a critical gap and height and follows a non-monotonic trend with decreasing gaps and heights. This is also seperately determined by mass or damping effects which in turn plays a dominating role for different parameters.

Lastly, in Chapter 4 we have discussed a design of a macro-scale experimental test-rig to observe hydrodynamic coupling in an array of beams oscillating in fluidic media for two cases: 1) far from the surface and 2) in close proximity to the surface. The results suggest a clear coupling of the parameters gap $\bar{g}$ and distance $\bar{h}$ implying that they cannot and should not be investigated separately.

5.1.1 Technological implications

New insights and knowledge of hydrodynamic load and coupling effects gained for different gaps and heights will help future AFM array design avoiding or exploiting coupling influences. In Figure 5.1, we present two different views of the coupling ratio (in percentage) for two beams immersed in glycerol.

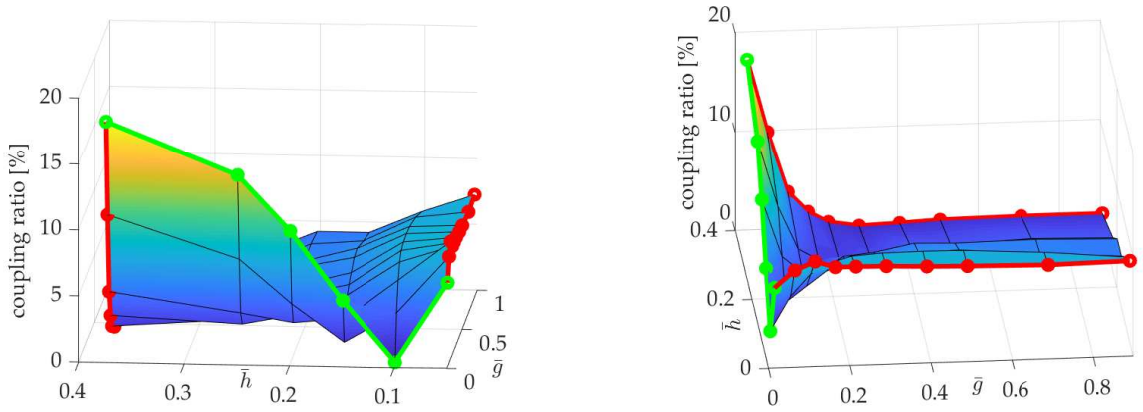

(a) (b)

Figure 5.1: Coupling ratio of passive to active beam (as a percentage) for two beams immersed in glycerol in close proximity to a surface for (a) varying gaps $\bar{g}$ [left panel] and with varying heights $\bar{h}$ [right panel].

In the left panel we note that the red curve shows a distinct trend when far away from the surface (concave) and when in close proximity to the surface (convex). This implies that there is a transitional regime between the two curves and a set of critical parameters at which this switch occurs. From the right panel we note this switch to occur at a critical height (i.e. $\bar{h} = 0.1$) for which the coupling influence is minimum as shown by the green curve. Hence, if a designer intends to miminimze fluid-coupling effects it is recommended to operate the array at this critical height from the sample surface. However, this critical height can shift depending on other factors such as number of members in the array, choice of fluid etc. and needs to be estimated accordingly.

Also, spacing between members in the array will dictate whether non-neighbouring members influence the overall array dynamics suggesting the designer that there will be no additional coupling effects from non-neighbouring members for $\bar{g} > 0.4$. Any shift in natural frequency of the array may incorrectly be attributed to the topographical changes of the sample (interaction forces felt at the cantilever tip) whereas the shift may be due to the fluid-coupling effects as described in Section 1.3. This will in turn allow us to determine accurately if the artifact present is original or arises as a result of fluid-coupling. Also, given the increasing demand for improving the scan speeds without compromising on the image quality, the spacing between members of the array and their respective heights to the corresponding sample under investigation becomes critical allowing the designer to decide on the minimum and maximum gaps at which the members of the array can be spaced and also the heights

at which they can operate to produce high throughput. For instance, Rangelow et al. [1] used a 4-cantilever array with $\bar{g} \sim 0.1$ as shown in Figure 5.2. But, AFM arrays can be purposefully designed such that e.g. the array is operated in the "dip" region (green curve) as seen in Figure 5.1 to minimize fluid-coupling effects.

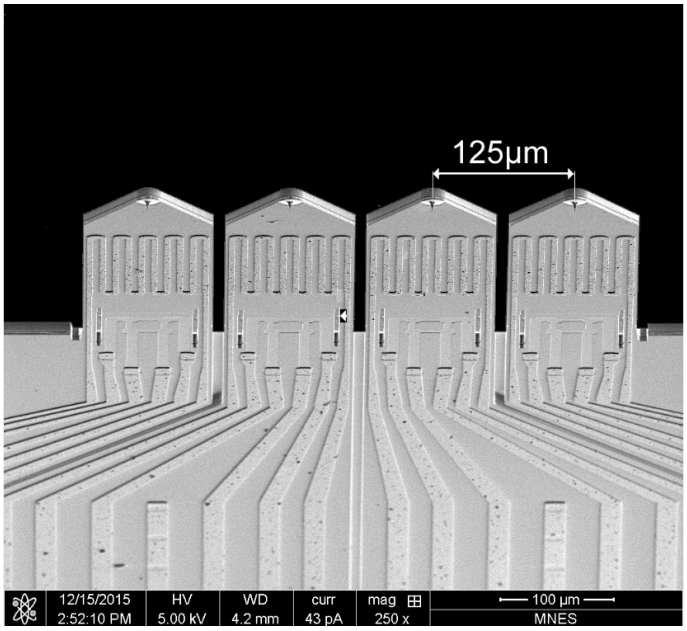

Figure 5.2: SEM image of a 4-cantilever array. Courtesy of Rangelow group [1].

5.2 Future outlook

The hydrodynamic coupling analysis described in Chapter 2 incorporating the contribution of non-neighbouring members can be extended to larger arrays comprising more than five members to study their impact on the overall array dynamics enhancing AFM array technology.

The mathematical model and analysis developed in Chapter 3 can be extended to large-sized arrays (100-1000 members) in close proximity to a surface. Also, a higher resolution analysis (more data points) should be performed and additional parameter studies for different amplitude ratios r and phases θ to understand their effects on coupling and overall hydrodynamic loading profiles impacting the array dynamics. A quantitative study for a particular application should be performed to compare results to analytical models.

From Figure 5.3 we have fitted a curve through the calculated numerical (circular markers) and experimental (square markers) data points when the beams are in close proximity to the surface (for a similar $\bar{h}$). We observe that the fluid-coupling effects cannot be ignored for small $\bar{g}$ and small $\bar{h}$. The experimental test-rig is designed based on gap dependent coupling when far from the surface. However, we note that the coupling does have a significant influence with large $\bar{g}$ and small $\bar{h}$. Hence, future test-rigs should account for large variation of $\bar{g}$ in order to study the

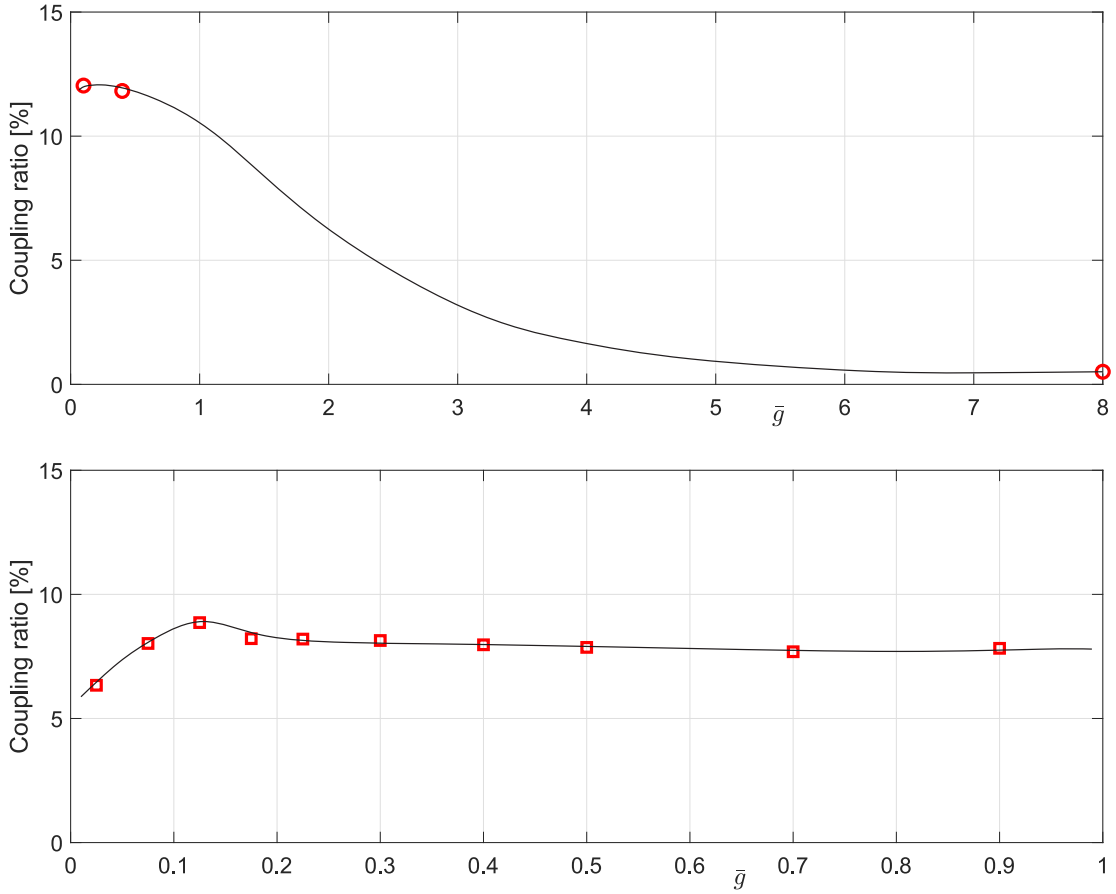

Figure 5.3: Coupling ratio of passive to active beam (as a percentage) for varying gaps $\bar{g}$ and heights $\bar{h}$ in case of two beams immersed in glycerol for $Re = \mathcal{O}(100)$; numerical results (top panel, circular markers) and experimental results (bottom panel, square markers).

fluid-coupling effects broadly especially when in close proximity to the surface.

We have restricted our attention purely to hydrodynamic coupling influences and have ignored fluid-structural coupling effects. Hence, a combined fluid-structure interaction model for an array of cantilevers should be modeled to understand the additional coupling effects arising from the structure on the overall dynamics of the array. Such detailed analyses could pave the way for future designs of AFM array technology in fluidic environments.

5.3 Novel contributions

The novel contributions of this thesis are:

1. extension of the model including non-neighbouring members for M beams in an infinite fluid domain (Chapter 2).

2. analyzing the overall hydrodynamic load and coupling effects of non-neighbouring members in a three- and a five-beam array vibrating in an infinite fluid domain (Chapter 2).

Findings suggested that the model of only nearest neighbours is sufficient for high Re at large gaps whereas one cannot neglect the model incorporating non-neighbouring members for low Re since the critical gaps at which the beams couple is large. A more detailed quantitative study is necessary to accurately predict the critical gaps.

3. mathematical modelling for two beams vibrating in close proximity to a surface in a fluid environment which is also extended to three- and a five-beam array. (Chapter 3).

4. new findings of hydrodynamic coupling being mutually dependent on both gaps and heights (Chapter 3).

5. A design of a macro-scale experimental test-rig is discussed and numerical results are compared against experimental findings (Chapter 4).

   The findings provided good qualitative agreement with experiments showing distinct trends observed for "far from the wall" case and "close to the wall" case. Also, the coupling ratio is position independent of the active beam since the beams are operated for $Re = \mathcal{O}(100)$ while the influence of non-neighbouring members becomes significant with increasing size of the array and decreasing gaps between beams.

Therefore, the objectives of this work have been satisfactorily met.

Bibliography

[1] A. Ahmad, N. Nikolov, T. Angelov, T. Ivonov, A. Reum, I. Atanasov, E. Guliyev, V. Ishchuk, M. Kaestner, Y. Krivoshapkina, S. Lenk, C. Lenk, I. W. Rangelow, and M. Holz. Large area fast-AFM scanning with active "Quattro" cantilever arrays. *Journal of Vacuum Science and Technology B*, 34(6):06KM03, 2016.

[2] T. Ando. High-speed atomic force microscopy coming of age. *Nanotechnology*, 23(6):062001, 2012.

[3] T. Ando, T. Uchihashi, and N. Kodera. High-speed AFM and applications to biomolecular systems. *Annual review of biophysics*, 42:393–414, 2013.

[4] M. Aureli and M. Porfiri. Low frequency and large amplitude oscillations of cantilevers in viscous fluids. *Applied Physics Letters*, 96(16):15–18, 2010.

[5] S. Basak and A. Raman. Hydrodynamic coupling between micromechanical beams oscillating in viscous fluids. *Physics of Fluids*, 19(1):017105, 2007.

[6] S. Basak, A. Raman, and S. V. Garimella. Hydrodynamic loading of microcantilevers vibrating in viscous fluids. *Journal of Applied Physics*, 99(11):114906, 2006.

[7] G. Binnig, C. F. Quate, and C. Gerber. Atomic Force Microscope. *Physical Review Letters*, 56(9):930–933, 1986.

[8] F. Cellini, C. Intartaglia, L. Soria, and M. Porfiri. Effect of hydrodynamic interaction on energy harvesting in arrays of ionic polymer metal composites vibrating in a viscous fluid. *Smart Materials and Structures*, 23(4), 2014.

[9] J. V. Chacko, F. C. Zanacchi, and A. Diaspro. Probing cytoskeletal structures by coupling optical superresolution and AFM techniques for a correlative approach. *Cytoskeleton*, 70(11):729–740, 2013.

[10] I. Chakraborty and B. Balachandran. Noise influenced elastic cantilever dynamics with nonlinear tip interaction forces. *Nonlinear Dynamics*, 66(3):427–439, 2011.

[11] M. Choi, C. Cierpka, and Y.-H. Kim. Effects of the distance between a vibrating cantilever pair. *European Journal of Mechanics - B/Fluids*, 43:154–165, 2014.

[12] J. W. M. Chon, P. Mulvaney, and J. E. Sader. Experimental validation of theoretical models for the frequency response of atomic force microscope cantilever beams immersed in fluids. *Journal of Applied Physics*, 87(8):3978, 2000.

[13] M. Clark and M. Paul. The stochastic dynamics of an array of atomic force microscopes in a viscous fluid. *International Journal of Non-Linear Mechanics*, 42(4):690–696, 2006.

[14] R. J. Clarke, V. Bachtiar, T. C. Lee, J. E. Cater, and J. Minton. Response of a fluid-immersed microcantilever close to a deformable body. *Journal of Applied Physics*, 117(9), 2015.

[15] R. J. Clarke, S. M. Cox, P. M. Williams, and O. E. Jensen. The drag on a microcantilever oscillating near a wall. *Journal of Fluid Mechanics*, 545:397–426, 2005.

[16] R. J. Clarke, S. M. Cox, P. M. Williams, and O. E. Jensen. The drag on a microcantilever oscillating near a wall. *Journal of Fluid Mechanics*, 545(May):397–426, 2005.

[17] R. J. Clarke, O. E. Jensen, and J. Billingham. Three-dimensional elastohydrodynamics of a thin plate oscillating above a wall. *Physical Review E - Statistical, Nonlinear, and Soft Matter Physics*, 78(5):1–17, 2008.

[18] L. W. Francis, P. D. Lewis, C. J. Wright, and R. S. Conlan. Atomic force microscopy comes of age. *Biology of the cell*, 102(2):133–143, 2010.

[19] N. A. Geisse. AFM and combined optical techniques. *Materials Today*, 12(7-8):40–45, 2009.

[20] M. K. Ghatkesar, T. Braun, V. Barwich, J.-P. Ramseyer, C. Gerber, M. Hegner, and H. P. Lang. Resonating modes of vibrating microcantilevers in liquid. *Applied Physics Letters*, 92(4):10–13, 2008.

[21] C. P. Green and J. E. Sader. Small amplitude oscillations of a thin beam immersed in a viscous fluid near a solid surface. *Physics of Fluids*, 17(7):073102, 2005.

[22] A. K. Gupta, P. R. Nair, D. Akin, M. R. Ladisch, S. Broyles, M. A. Alam, and R. Bashir. Anomalous resonance in a nanomechanical biosensor. *Proceedings of the National Academy of Sciences of the United States of America*, 103(36):13362–13367, 2006.

[23] H. Hosaka and K. Itao. Coupled Vibration of Microcantilever Array Induced by Airflow Force. *Journal of Vibration and Acoustics*, 124(1):26, 2002.

[24] C. Huygens. *Philosophical Transactions of the Royal Society of London*, 4:937–953, 1669.

[25] C. Intartaglia, L. Soria, and M. Porfiri. Hydrodynamic coupling of two sharp-edged beams vibrating in a viscous fluid. *Proceedings of the Royal Society*, 470(2162), 2013.

[26] S. Jackson. *Modelling and control of coupled AFM arrays for parallel imaging verified through a macro scale experiment*. PhD thesis, University of Canterbury, 2017.

[27] K.-H. Jeong, G.-H. Yoo, and S.-C. Lee. Hydroelastic vibration of two identical rectangular plates. *Journal of Sound and Vibration*, 272(3-5):539–555, May 2004.

[28] B. Y. John and B. Buck. Synchronous rhythmic flashing of fireflies. *The Quarterly Review of Biology*, 13(3):301–314, 2003.

[29] A. J. Katan and C. Dekker. High-speed AFM reveals the dynamics of single biomolecules at the nanometer scale. *Cell*, 147(5):979–982, 2011.

[30] M. Kimber, S. V. Garimella, and A. Raman. Local Heat Transfer Coefficients Induced by Piezoelectrically Actuated Vibrating Cantilevers. *Journal of Heat Transfer*, 129(9):1168–1176, 2007.

[31] M. Kimber, R. Lonergan, and S. Garimella. Experimental study of aerodynamic damping in arrays of vibrating cantilevers. *Journal of Fluids and Structures*, 25(8):1334–1347, 2009.

[32] D. Kiracofe and A. Raman. Nonlinear dynamics of the atomic force microscope at the liquid-solid interface. *Physical Review B*, 86(20):205405, 2012.

[33] T. A. Klar, S. Jakobs, M. Dyba, A. Egner, and S. W. Hell. Fluorescence microscopy with diffraction resolution barrier broken by stimulated emission. *Proceedings of the National Academy of Sciences of the United States of America*, 97(15):8206–8210, 2000.

[34] H. P. Lang, M. Hegner, and C. Gerber. Cantilever array sensors. *Materials Today*, 8(4):30–36, 2005.

[35] J.-H. Lee, Y.-D. Lau, C.-M. Yao, and W. Fang. Experimental study of the effect of hydrodynamic coupling of micro-cantilever array on the dynamic response of micro-cantilever. *Sensors and Actuators A: Physical*, 165(1):79–85, 2011.

[36] C. Liu. Parallel scanning probe arrays: their applications. *Materials Today*, 11(SUPPL.):22–29, 2008.

[37] G. Lukinavičius, L. Reymond, E. D'Este, A. Masharina, F. Göttfert, H. Ta, A. Güther, M. Fournier, S. Rizzo, H. Waldmann, C. Blaukopf, C. Sommer, D. W. Gerlich, H.-D. Arndt, S. W. Hell, and K. Johnsson. Fluorogenic probes for live-cell imaging of the cytoskeleton. *Nature methods*, 11(7):731–733, July 2014.

[38] Y. L. Lyubchenko, L. S. Shlyakhtenko, and T. Ando. Imaging of nucleic acids with atomic force microscopy. *Methods*, 54(2):274–283, 2011.

[39] C. Metzger, J. Rodriguez, and F. Zypman. Vibration of a Cantilever Beam in Ambient Fluid. 2016.

[40] L. I. Mi, L. I. U. Lianqing, X. I. Ning, W. Yuechao, D. Zaili, X. Xiubin, and Z. Weijing. Progress of AFM single-cell and single-molecule morphology imaging. *Progress Cell Biology*, 58(26):3177–3182, 2013.

[41] T. Michels and I. W. Rangelow. Review of scanning probe micromachining and its applications within nanoscience. *Microelectronic Engineering*, 126:191–203, 2014.

[42] K. C. Morton and L. A. Baker. Atomic force microscopy-based bioanalysis for the study of disease. *Analytical Methods*, 6(14):4932, 2014.

[43] T. Naik, E. K. Longmire, and S. C. Mantell. Dynamic response of a cantilever in liquid near a solid wall. *Sensors and Actuators A:Physical*, 102:240–254, 2002.

[44] S. Nazari, A. Heydari, and J. Khaligh. Modified Modeling of the Heart by Applying Nonlinear Oscillators and Designing Proper Control Signal. *Applied Mathematics*, 04(07):972–978, 2013.

[45] O. D. Payton, L. Picco, and T. B. Scott. High-speed atomic force microscopy for materials science. *International Materials Reviews*, 61(8):473–494, 2016.

[46] C. Pozrikidis. *Boundary Integral and Singularity Methods for Linearized Viscous Flow*. Cambridge University Press, 1992.

[47] M. Raeder. Design, analysis and fabrication of a test-rig to investigate dynamics of an array in fluidic media, 2016.

[48] I. W. Rangelow, T. Ivanov, A. Ahmad, M. Kaestner, C. Lenk, I. S. Bozchalooi, F. Xia, K. Youcef-Toumi, M. Holz, and A. Reum. Review Article: Active scanning probes: A versatile toolkit for fast imaging and emerging nanofabrication. *Journal of Vacuum Science & Technology B, Nanotechnology and Microelectronics: Materials, Processing, Measurement, and Phenomena*, 35(6):06G101, 2017.

[49] I. W. Rangelow, T. Ivanov, K. Ivanova, B. E. Volland, P. Grabiec, Y. Sarov, A. Persaud, T. Gotszalk, P. Zawierucha, M. Zielony, D. Dontzov, B. Schmidt, M. Zier, N. Nikolov, I. Kostic, W. Engl, T. Sulzbach, J. Mielczarski, S. Kolb, D. P. Latimier, R. Pedreau, V. Djakov, S. E. Huq, K. Edinger, O. Fortagne, A. Almansa, and H. O. Blom. Piezoresistive and self-actuated 128-cantilever arrays for nanotechnology applications. *Microelectronic Engineering*, 84(5-8):1260–1264, 2007.

[50] D. J. Rapport, H. A. Regier, and T. C. Hutchinson. Ecosystem Behavior Under Stress. *The American Naturalist*, 125(5):617–640, 1985.

[51] W. M. Roberts and M. A. Rutherford. Linear and nonlinear processing in hair cells. *Journal of Experimental Biology*, 211(11):1775–1780, 2008.

[52] C. G. Rodriguez, F. G. Pierart, L. R. Contzen, and E. Egusquiza. Experimental Modal Analysis in Submerged Cantilever Plate with Nearby Rigid Wall. *Proceedings of ISMA 2010*, pages 2591–2596, 2010.

[53] J. E. Sader. Frequency response of cantilever beams immersed in viscous fluids with applications to the atomic force microscope. *Journal of Applied Physics*, 84(1):64, 1998.

[54] Y. Sarov, T. Ivanov, A. Frank, and I. W. Rangelow. Thermally driven multilayer actuator for 2D cantilever arrays. *Applied Physics A*, 102(1):61–68, 2010.

[55] W. Shyy, M. Berg, and D. Ljungqvist. Flapping and flexible wings for biological and micro air vehicles. *Progress in Aerospace Sciences*, 35:455–505, 1999.

[56] G. G. Stokes. *On the Effect of the Internal Friction of Fluids on the Motion of Pendulums*, volume 3 of *Cambridge Library Collection - Mathematics*, page 1–10. Cambridge University Press, 2009.

[57] E. O. Tuck. Calculation of Unsteady Flows Due to Small Motions of Cylinders in Viscous Fluid. *Journal of Engineering Mathematics*, 3(1):29–44, 1969.

[58] R. C. Tung, A. Jana, and A. Raman. Hydrodynamic loading of microcantilevers oscillating near rigid walls. *Journal of Applied Physics*, 104(11), 2008.

[59] C. A. Van Eysden and J. E. Sader. Small amplitude oscillations of a flexible thin blade in a viscous fluid: Exact analytical solution. *Physics of Fluids*, 18(12):1–11, 2006.

[60] N. Wagner. Array Dynamics Submerged in Fluids: Experimental Investigations of a Two-Beam Array in Air and Glycerol. Master's thesis, Technical University Ilmenau, 2018.

[61] R. Yang, N. Xi, C. Kar Man Fung, K. Seiffert-Sinha, K. Wai Chiu Lai, and A. A. Sinha. The emergence of afm applications to cell biology: How new technologies are facilitating investigation of human cells in health and disease at the nanoscale. *Journal of Nanoscience Letters*, 1(2):87–101, 2011.

Appendices

Appendix A

Coupling matrix for two beams vibrating in close proximity to a surface

$$\hat{\boldsymbol{G}}_{\boldsymbol{II}} = \begin{bmatrix} A_1 & 0 & A_{2_{11}} & A_{2_{22}} & -A_{3_{11}} & -A_{3_{22}} \\ 0 & B_1 & -A_{3_{11}} & -A_{3_{22}} & B_{3_{11}} & B_{3_{22}} \\ C_1 & -C_2 & C_{3_{11}} & C_{3_{12}} & 0 & 0 \\ C_1 & -C_2 & C_{3_{21}} & C_{3_{22}} & 0 & 0 \\ -C_2 & D_2 & 0 & 0 & D_{3_{11}} & D_{3_{12}} \\ -C_2 & D_2 & 0 & 0 & D_{3_{21}} & D_{3_{22}} \end{bmatrix},$$

The above matrix can be partitioned into nine 2x2 blocks

$$\mathbf{G}_{11} = \begin{bmatrix} A_1 & 0 \\ 0 & B_1 \end{bmatrix}$$

$$\mathbf{G}_{12} = \begin{bmatrix} A_{2_{11}} & A_{2_{22}} \\ -A_{3_{11}} & -A_{3_{22}} \end{bmatrix}$$

$$\mathbf{G}_{13} = \begin{bmatrix} -A_{3_{11}} & -A_{3_{22}} \\ B_{3_{11}} & B_{3_{22}} \end{bmatrix}$$

$$\mathbf{G}_{21} = \begin{bmatrix} C_1 & -C_2 \\ C_1 & -C_2 \end{bmatrix}$$

$$\mathbf{G}_{22} = \begin{bmatrix} C_{3_{11}} & C_{3_{12}} \\ C_{3_{21}} & C_{3_{22}} \end{bmatrix}$$

$$\mathbf{G}_{23} = \begin{bmatrix} 0 & 0 \\ 0 & 0 \end{bmatrix}$$

$$\mathbf{G}_{31} = \begin{bmatrix} -C_2 & D_2 \\ -C_2 & D_2 \end{bmatrix}$$

$$\mathbf{G}_{32} = \begin{bmatrix} 0 & 0 \\ 0 & 0 \end{bmatrix}$$

$$\mathbf{G}_{33} = \begin{bmatrix} D_{3_{11}} & D_{3_{12}} \\ D_{3_{21}} & D_{3_{22}} \end{bmatrix}$$

Appendix B

Matrix elements

$$A_1 = \int_{L^w\xi'_j}^{L^w\xi'_{j+1}} \psi_{z'z}(\xi_k, 0|\xi'_j, 0)d\xi',$$

$$A_2 = \int_{\xi'_j}^{\xi'_{j+1}} \psi_{z'z}(\xi_k, 0|\xi'_j, \bar{h})d\xi',$$

$$A_3 = \int_{\xi'_j}^{\xi'_{j+1}} \psi_{\xi'z}(\xi_k, 0|\xi'_j, \bar{h})d\xi',$$

$$B_1 = \int_{L^w\xi'_j}^{L^w\xi'_{j+1}} \psi_{\xi'\xi}(\xi_k, 0|\xi'_j, 0)d\xi',$$

$$B_3 = \int_{\xi'_j}^{\xi'_{j+1}} \psi_{\xi'\xi}(\xi_k, 0|\xi'_j, \bar{h})d\xi',$$

$$C_1 = \int_{L^w\xi'_j}^{L^w\xi'_{j+1}} \psi_{z'z}(\xi_k, \bar{h}|\xi'_j, 0)d\xi',$$

$$C_2 = \int_{L^w\xi'_j}^{L^w\xi'_{j+1}} \psi_{\xi'z}(\xi_k, \bar{h}|\xi'_j, 0)d\xi',$$

$$C_3 = \int_{\xi'_j}^{\xi'_{j+1}} \psi_{z'z}(\xi_k, \bar{h}|\xi'_j, \bar{h})d\xi',$$

$$D_2 = \int_{L^w\xi'_j}^{L^w\xi'_{j+1}} \psi_{\xi'\xi}(\xi_k, \bar{h}|\xi'_j, 0)d\xi',$$

$$D_3 = \int_{\xi'_j}^{\xi'_{j+1}} \psi_{\xi'\xi}(\xi_k, \bar{h}|\xi'_j, \bar{h})d\xi'.$$

For instance, to compute $D_{3_{21}}$ which implies influence of segments of beam 1 on beam 2, the integral

$$D_3 = \int_{\xi'_j}^{\xi'_{j+1}} \psi_{\xi'\xi}(\xi_k, \bar{h}|\xi'_j, \bar{h}) d\xi'$$

becomes

$$D_{3_{21}} = \int_{\xi'_{j2}}^{\xi'_{j2+1}} \psi_{\xi'_2\xi_1}(\xi_{k1}, \bar{h}|\xi'_{j2}, \bar{h}) d\xi'_2$$

A similar approach can be used to obtain other elements.

Appendix C

Convergence study

A systematic and extensive convergence study was performed in order to obtain sufficient accuracy for the number of wall and beam elements N, the wall length L_w, and the order n of the Gauss-Legendre quadrature used for computing the entries of the submatrices.

For a single beam in an infinite fluid domain, a value of $N = 49$ and $n = 4$ was found to be adequate at $Re = 1$. Next, an additional beam was included and we reached the conclusion that N was independent of number of members in the array. One could interpret this as a case when both beams are brought close to each other to close the gaps, the beam would act like a single beam with twice its initial width in which case N shouldn't change.

A single beam in close proximity to a surface was then considered. The number of discretization elements N was systematically increased for $n = 4$ and $L_w = 10$ for a single beam vibrating in close proximity to a surface. It was found that a low n was sufficient as increasing numbers to $n = 10$ caused numerical instability. Also, increasing L_w beyond 15 for a single beam resulted in accuracy of obtained results being within 1%.

In Figures C.1 and C.2, we plot the fitted curves between number of elements N required for corresponding heights in which we are within 2% of the true value of the imaginary and real parts for $Re \leq 1$.

A similar procedure was repeated at $Re = 100$ but the curve plotted is based on an error within 20% for the real part (assuming that the true value occurs at $N = 1500$) at $\bar{h} = 0.3$ and hence, the results are interpreted keeping this in mind that a much better accuracy is required when the beam is in close proximity to the surface and in particular, the real part.

This curve is not influenced by n and the convergence solely depended on N which increased with increasing proximity to the surface. Also, a compromise between accuracy of results and computational cost was sought and hence, the N values were chosen correspondingly for the respective heights for a qualitative study.

We plot the errors in absolute, imaginary and real parts of pressure at $Re = 100$

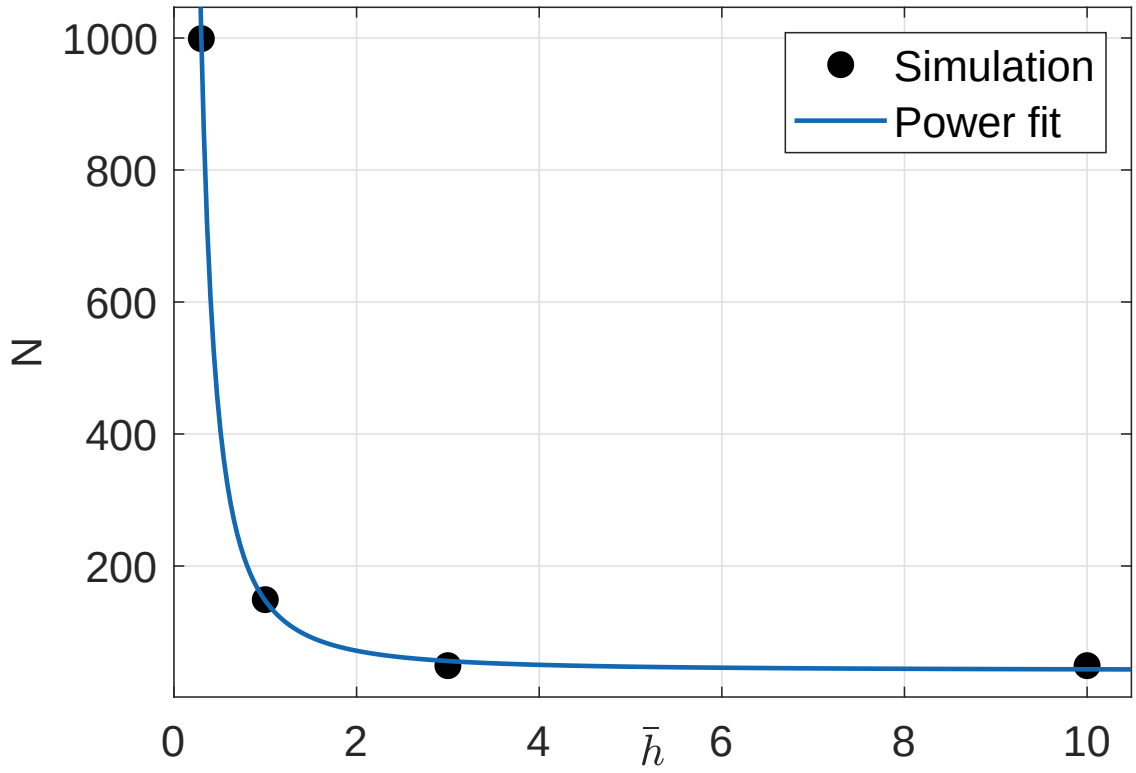

Figure C.1: 1% convergence curve for N versus $\bar{h}$.

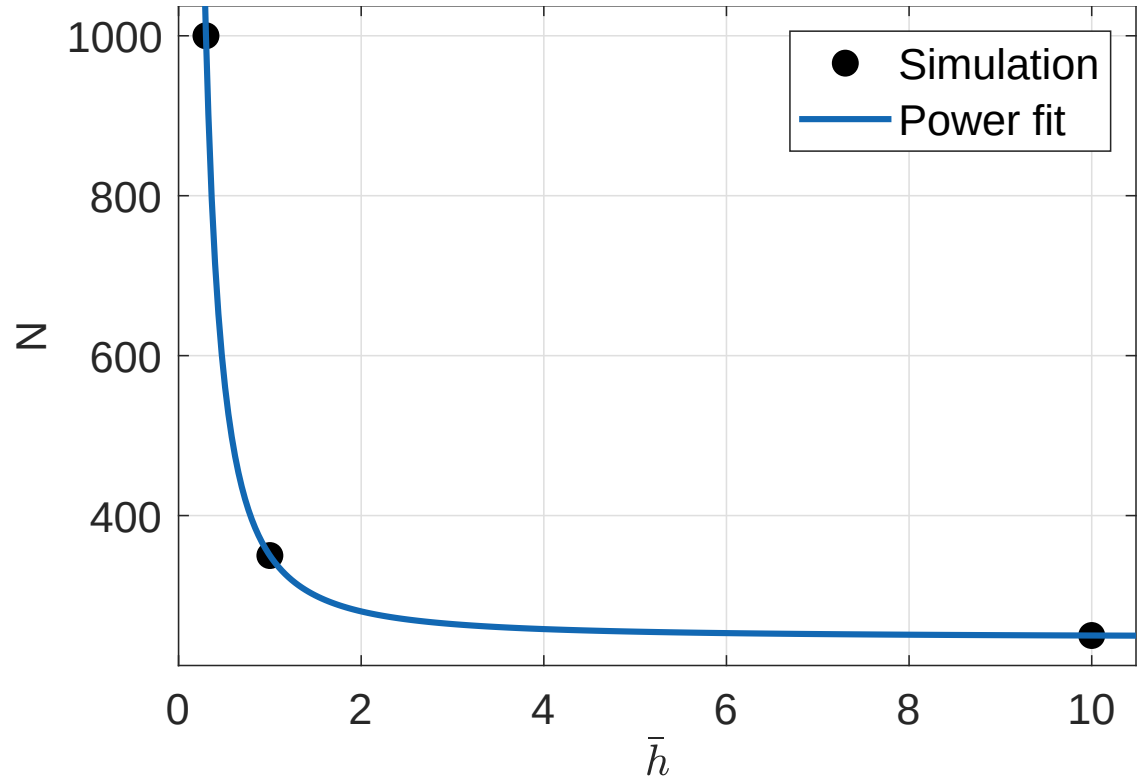

Figure C.2: Plot of N versus $\bar{h}$ at $Re = 100$.

for different N's at $n = 4$ and $L_w = 10$ for the smallest height under consideration i.e $\bar{h} = 0.3$ in Figure C.3.

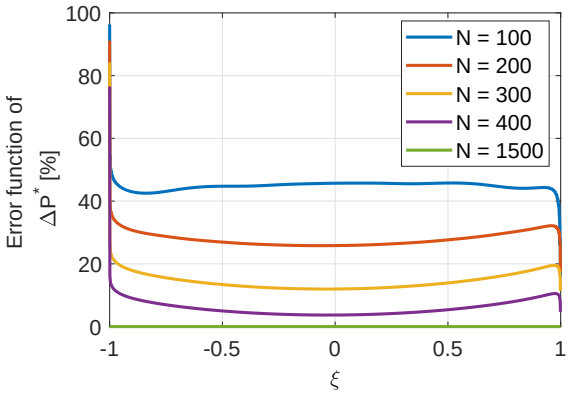

(a)

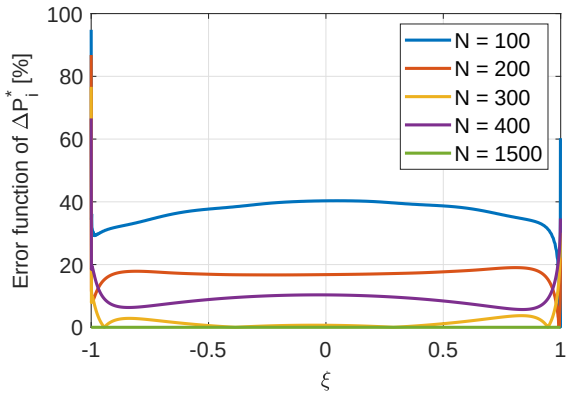

(b)

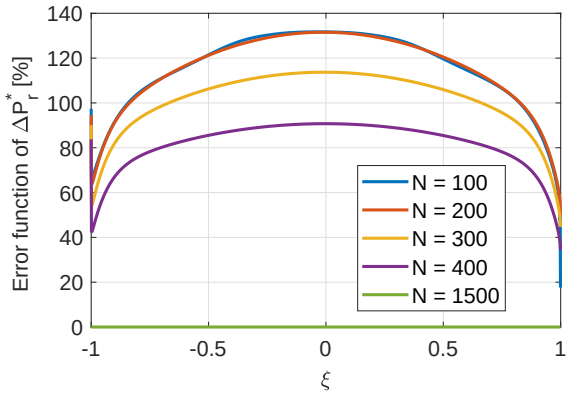

(c)

Figure C.3: Error functions of (a) absolute, (b) imaginary and (c) real parts of pressure corresponding to varying N for a single beam oscillating in close proximity to a surface ($\bar{h} = 0.3$), $Re = 100$.

We observe that the errors at $N = 400$ is within 20% over most part of the beam width (excluding the edges) which is not the case with the real part. Hence, further simulations were run between $N = 400$ and $N = 1500$ to determine the N to be used so as to reduce the percentage error of the real part while also keeping in mind to preserve the qualitative nature of the pressure profile across the beam width and the time required to run the simulation.

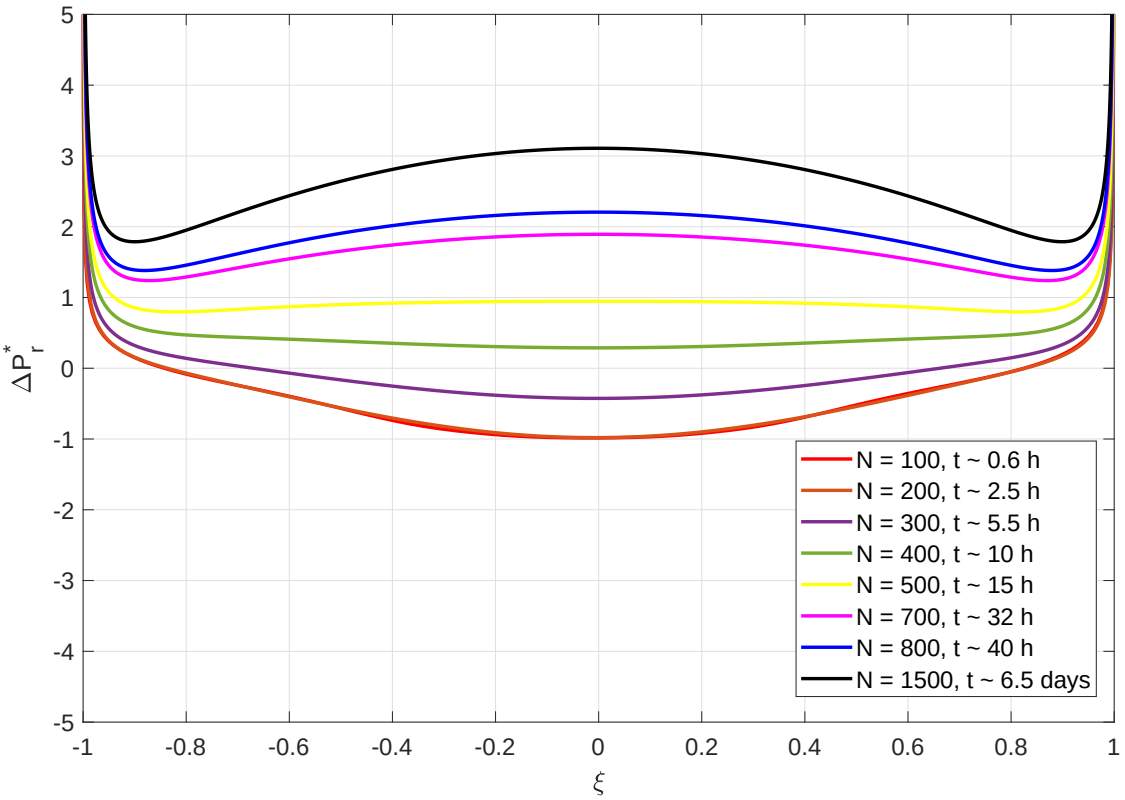

Figure C.4: Real parts of pressure computed for various N's across the width of the beam when in close proximity to the surface i.e. $\bar{h} = 0.3$.

In Figure C.4, we plot the profiles of real parts of pressure for different values of N and found that $N = 700$ satisfies our purposes of a qualitative understanding of the physics, with the respective time taken to run simulations for each N provided in the legend.

We found that N is independent of the number of beams in the array and the gaps between the beams but solely depended on the proximity to the surface. Also, $Re = 100$ resulted in slower convergence requiring more segments N across the width of the beam. Hence, N calculated for $Re = 100$ should be more than sufficient for performing calculations at a low Re, however, to cut down on computational time, convergence analysis was also performed for $Re = 1$ and the corresponding N values were used for $Re = \{0.1, 1\}$.

Based on these findings we chose $N = 50$ for $\bar{h} = 10$, $N = 150$ for $\bar{h} = 1$ and $N = 1000$ for $\bar{h} = 0.3$ at $Re = \{0.1, 1\}$ for a two-beam array with $N = 700$ chosen for $\bar{h} = 0.3$ at $Re = 100$. For a three-beam array $N = \{50, 150, 700\}$ were chosen for $\bar{h} = \{10, 1, 0.3\}$ at $Re = \{0.1, 1\}$. But at $Re = 100$, $N = \{250, 350, 700\}$ at $\bar{h} = \{10, 1, 0.3\}$ were correspondingly chosen. For a five-beam array similar N values were chosen as that of a three-beam array for $\bar{h} = \{10, 1\}$ for the respective Reynolds numbers but due to the number of calculations enormously increasing (a two-beam array at $Re = 0.1$ when far away from the wall takes about 20 minutes to run while a five-beam array in close proximity to a surface at $Re = 100$ takes about 5.25 days) with more beams in the array and a need to compromise on the

computational time, a value of $N = 500$ was chosen at $\bar{h} = 0.3$ for all Reynolds numbers under consideration.